January 2016

CONTINUUM DISLOCATION DYNAMICS MODELING OF THE DEFORMATION OF FCC SINGLE CRYSTALS

Shengxu Xia
Purdue University

Graduate School Form
30 Updated 12/26/2015

PURDUE UNIVERSITY
GRADUATE SCHOOL
Thesis/Dissertation Acceptance

This is to certify that the thesis/dissertation prepared

By Shengxu Xia

Entitled

CONTINUUM DISLOCATION DYNAMICS MODELING OF THE DEFORMATION OF FCC SINGLE CRYSTALS

For the degree of Doctor of Philosophy

Is approved by the final examining committee:

Rodney W. Trice
Co-chair

Alejandro Strachan

Anter El-Azab
Co-chair

Jr. David Johnson

Marisol Koslowski

To the best of my knowledge and as understood by the student in the Thesis/Dissertation Agreement, Publication Delay, and Certification Disclaimer (Graduate School Form 32), this thesis/dissertation adheres to the provisions of Purdue University's "Policy of Integrity in Research" and the use of copyright material.

Approved by Major Professor(s): Anter El-Azab

Approved by: David F. Bahr 7/21/2016

Head of the Departmental Graduate Program Date

CONTINUUM DISLOCATION DYNAMICS MODELING OF THE DEFORMATION OF FCC SINGLE CRYSTALS

A Dissertation

Submitted to the Faculty

of

Purdue University

by

Shengxu Xia

In Partial Fulfillment of the

Requirements for the Degree

of

Doctor of Philosophy

August 2016

Purdue University

West Lafayette, Indiana

ACKNOWLEDGEMENTS

It has been a great honour to spend my doctoral degree years at Purdue University where I have been immersed in a highly intellectual atmosphere. The completion of my dissertation has been a long journey and I could not succeed without the invaluable assistance of many individuals to whom I wish to express my deepest appreciation.

First of all, I would like to dedicate a special thank you to my advisor, Professor Anter El-Azab, who has been offering tremendous support over the past years. It is his encouragement, enthusiasm, persistence, knowledge, and spirit that made this dissertation possible. His personality and character will always be an example to look up to for the rest of my life.

I am also grateful to the committee members of my study plan, Professors Rodney Trice, David Johnson, Alejandro Strachan, and Marisol Koslowski. The kindness and guidance from them has benefited a great deal. Their expertise in various domains related to my work was so important for my research. I would also like to express my appreciation to Professor Eric Kvam who offers great assistance in my preliminary exam.

My appreciation is extended to all the professors who taught me with a great passion. The knowledge and techniques learned here shaped my learning experience. I would like to thank Professor Robert Spitzer for the opportunity of working with him as a teaching assistant.

Connections in the research communities have also been critical for me. I wish to express my sincere appreciation to those who made suggestions regarding my research, including, but not limited to, Professor Thomas Hochrainer, Dr. Ben Larson, Dr. Ladislas Kubin, Dr. Stefan Sandfeld, Professor Wolfgang Pantleon, and Dr. James Belak. I also wish to thank Professor Grethe Winther for collaborating with me and my advisor in one of the joint papers.

Special thanks are due to all my fellow group members and friends, Dr. Jie Deng, Dr. Srujan Rokkam, Professor Santosh Dubey, Dr. Karim Ahmed, Professor Mamdouh Mohamed, and Dr. Ahmed Hamed, for the joyful interaction and assistance through my doctoral research journey.

Last but not least, I would like to express my gratitude to my wife for her support and understanding during my studies, both at Purdue and Florida State University. I owe also a lot to my parents who supported throughout my education.

TABLE OF CONTENTS

Page

Page

LIST OF TABLES

LIST OF FIGURES

Figure Page

Figure Page

Figure Page

Figure Page

Figure Page

Figure Page

Figure Page

ABSTRACT

Shengxu, Xia. Ph.D., Purdue University, August 2016. Continuum Dislocation Dynamics Modelling of the Deformation of Single Crystals. Major Professor: Anter El-Azab.

A continuum dislocation dynamics model was developed for simulation of the deformation of Face Centred Cubic (FCC) single crystals. In this model, dislocations are described by a set of vector fields, one per slip system, whose evolution is governed by curl-type kinetic equations describing the transport of dislocation lines. These kinetic equations are closed by specifying the velocity field in terms of a mobility law in which the driving force is obtained by solving the Cauchy's equilibrium equation for stress. The coupled kinetic equations and crystal mechanics equations are numerically solved in a staggered fashion using a custom finite element approach featuring the use of Galerkin and Least Squares finite element methods for the mechanics and dislocation kinetics parts, respectively, on a mesh generated on an FCC superlattice. The spatial resolution of the mesh was determined based on the annihilation distance between opposite dislocations. Cross slip rates from discrete dislocation simulation have been incorporated into the continuum model by time coarse graining involving time series analysis. The overall model provides a full solution of the crystal deformation problem, including the space and time evolution of the dislocation density and all internal elastic and plastic fields. Under periodic boundary conditions, the model has been applied to predict the stress-strain behaviour of FCC crystal as well as the dislocation patterns for both monotonic and

cyclic loading conditions. For monotonic loading, the cell structure is predicted and the wavelength is detected and shown to satisfy the empirical similitude law. The dislocation patterns are found to depend on the loading mode, monotonic versus cyclic, as well as the crystal orientation. For cyclic loading, the famous vein structure was also predicted by the model and the composition of dislocation veins are analysed. All results are compared with experiments and other discrete dislocation dynamics simulations, yielding a good agreement. An important finding of this investigation is that cross slip was found to be critical in triggering cell structure formation under monotonic loading and that the average cell size evolution was found to strongly depend on the cross slip rate.

CHAPTER 1. INTRODUCTION

Plastic deformation of crystals is fundamental to strength of metals as it is related to the ductility, hardening failure of this class of materials. Plasticity of metals is carried by dislocations, which were originally proposed to interpret the difference between the theoretical and actual shear strengths of crystals. In the experiments that were done during 1920s, single crystals yield at much lower stress level than theoretically predicted and develop slip bands [1–5]. Based on these observations, Taylor [6], Polanyi [7] and Orowan [8–10] proposed almost at the same time the concept of dislocations—a linear defect which glides under the influence of shear stress causing deformation of crystals. The movement of these defects results in irreversible crystallographic and shape change of the crystal, inducing so-called plasticity. The resistance of metal to plastic deformation derives its origin from the impediment of dislocation motion due to precipitates [11], solute atoms [12,13], and mutual interactions among the dislocations themselves [14].

Figure 1.1 plots the lattice structure for (a) an edge dislocation and (b) a section of dislocation curve which has edge and screw properties at two ends. A pure edge dislocation can be regarded as a result of the presence of an extra half plane of atoms in an otherwise perfect crystal. The position of the edge dislocation, in the case of figure 1.1(a), is located at the bottom of the extra half plane, with its line direction along the lower edge of the plane of atoms. Such an extra plane introduces distortion and stress in

the crystal. A pure screw dislocation can be constructed by slicing and shearing half of the crystal, as plotted in figure 1.1(b) at point A. Between a pure screw dislocation and a pure edge dislocation (point A and point B, respectively), the dislocation line has a mixed character. A dislocation line, from another angle of point, can be viewed as the boundary between slipped and un-slipped area. Thus, a dislocation line must either form a loop or ends on the boundary of a crystal [15] but without being broken within the crystal.

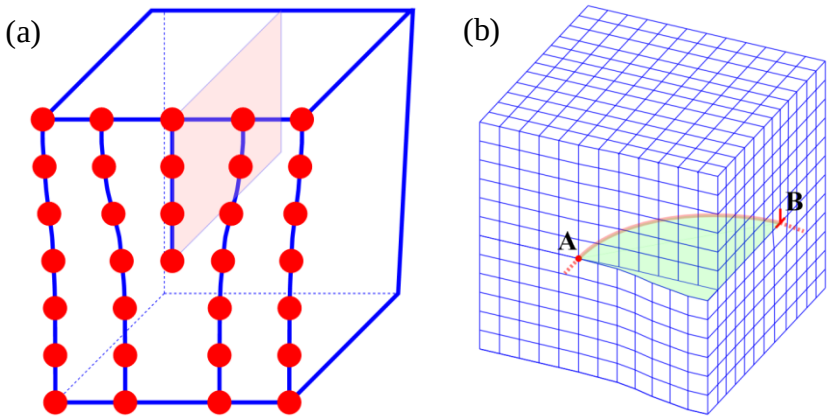

Figure 1.1. An illustration of (a) an edge dislocation line and (b) a curved dislocation line.

The Burgers vector [16] is defined to represent the direction and the magnitude of lattice distortion associated with a dislocation. A perfect Burgers vector always corresponds in direction to a close-packed row of atoms and in magnitude to the distance between two neighbouring atoms in that row [15]. A dislocation line possessing a perfect Burgers vector is called a perfect dislocation which may decompose, depending on crystallography [17], into partial dislocations, each of which is associated with a partial Burgers vector. The slip plane is the plane on which dislocations glide and the slip

direction is in the direction of a perfect Burgers vector. From a crystallographic perspective, a slip plane is preferably a plane on which atoms are most closely packed and a slip direction is also close packed direction in the slip plane. A combination of slip plane and slip direction constitutes a slip system. A Face Centred Crystal (FCC) has twelve {111}<110> type slip systems [18]. The plastic deformation takes place as a result of motion of dislocations on their slip planes. Unlike elastic deformation which occurs as a result of distortion of crystal lattice, the plastic slip essentially changes the way in which atoms are connected and is thus irreversible. Dislocations can leave traces when they pass in crystals and such traces are observed as slip bands in experiments [19–22].

The motion of dislocations is governed by the local stress field in accordance with the Peach-Koehler force [23] on dislocation lines. The latter depends on the stress field and Burgers vector and line direction of the dislocation. It is important to note that dislocations produce internal stress field around themselves. Such a stress field, according to the calculations by Volterra's singular model [24] and Peierls-Nabarro's non-singular model [25,26], has a long range character, i.e., the magnitude of stress decays with the distance to the order of one. The long range effect of internal stress implies that the behaviour of a dislocation segment is not only affected by dislocations close to it but also those dislocations which are far from it, but which are large in number. When dislocations are close enough to each other, they might interact by short range reactions which lead to jogs, kinks, annihilations [27]. Dislocations with new Burgers vector may also come into existence if this is energetically preferred [28], forming sessile locks [29–31] and glissile junctions [32]. All these junctions and interactions contribute to the impediment of dislocation motion to various degrees [33–37], resulting in the

phenomenon of strain hardening. One can imagine this by comparing the journey of a moving dislocation to the scenario in which a horizontal long rod is passing through a forest made of other dislocations [38]. Forest hardening derives from this conception [38–40].

The concept of dislocations only existed in theory until the first report of them in experiments enabled by Transmission Electron Microscopy (TEM) technology in 1950s [41]. Since then, experimentalists have been conducting extensive works on observing the landscape of dislocations in various materials under various conditions. It is commonly found that dislocations organize into patterns which are characterized by inhomogeneous distribution of dislocation dense and poor areas in space: the ladder and vein structures come into existence in single slip fatigue tests [42,43]; labyrinth structures are seen in multi-slip fatigued experiments [44]; cell structure reveals itself in multi-slip monotonic loading conditions [45,46]. Figure 1.2 plots typical patterns observed under fatigue and monotonic loadings.

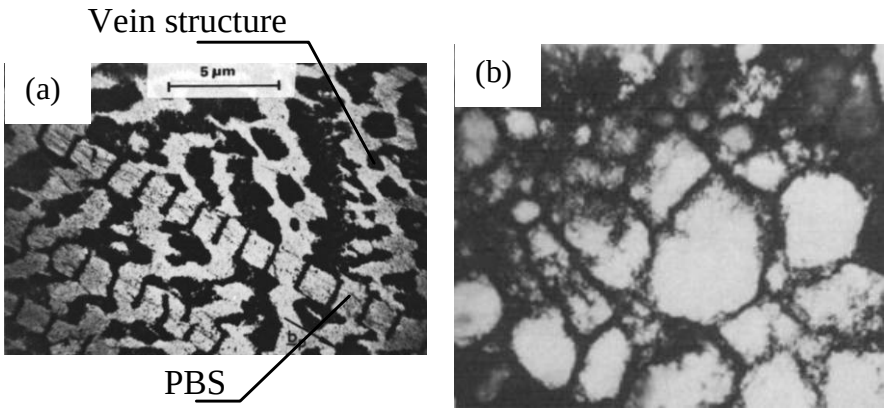

Figure 1.2. Dislocation structure in copper single crystal: (a) Persistent Slip Bands (PSB) ladder structure and vein structure on {121}-type slice in a crystal oriented for single slip, adopted from [47]. (b) Dislocation cell structure on (001) slice in a [001] crystal under monotonic loading at 19% strain, adopted from [45]

It is clear that the external loading does not smear dislocations through the space, but rather favours their clustering into rich and poor areas because such an organized pattern is energetically preferred to a homogeneous distribution [47–49]. The ladder structure shown in figure 1.2 contributes to the formation of persistent slip bands [50] which eventually lead to the fatigue crack initiation [51,52] by causing extrusions and intrusions that give rise to the strong localization of strain and stress [53]. The cell structure in figure 1.2(b) is thought to be related to recrystallization process [54,55] in which subgrains gradually establish themselves within a single crystal [56–59]. The patterning of dislocations is thus significant both from a theoretical standpoint and metal processing and metal performance.

The conventional plasticity [60] and crystal plasticity [61–63] theories, however, make no allowance for the consideration of these linear defects and thus prove to be unable to predict the heterogeneous distribution of dislocations and strain. In addition, the need to reveal the underlying mechanisms for hardening and patterning also requests the modelling of dislocation system from first principles. Furthermore, the results from modelling might drive new discoveries in experiments just as the proposal of dislocations precedes the spot of them in laboratories.

Thus, stimulated by experimental findings and motivated by the challenges, scientists start to develop models for dislocation evolution, which is referred to as dislocation dynamics and to which this dissertation is dedicated. The models of dislocation dynamics can be generally divided into two groups: the discrete dislocation dynamics [35,64–67] and continuum dislocation dynamics [68–73]. The discrete dislocation dynamics discretizes dislocation lines into sequences of segments connected by nodes. The entire simulation of dislocation motion is realized by managing the configuration of the collection of segments and nodes. The continuum dislocation dynamics does not treat the system at detailed level but rather replaces the dislocation lines with the description of mathematical fields which are governed by kinetic equations. The advantage of the continuum dislocation dynamics exists in the fact that the dislocation multiplication does not add any difficulty to the computational burden as in the discrete dislocation dynamics and thus larger strain level is prospective. Nevertheless, a comprehensive 3D continuum dislocation dynamics model illustrated with extensive examples is still far from completion.

Motivated by the need to predict the dislocation patterns, the present work is dedicated to the development of continuum dislocation dynamics for FCC single crystals under different mechanical loadings. A continuum model is first constructed, in which the dislocations are characterized by vector fields governed by curl-type kinetic equations. Such vector fields represent oriented dislocation densities on various slip systems. The evolution of dislocations and mechanical stress field are coupled by Orowan's law and mobility law. The implementation of the model delivers results that are in agreement with experiments in many respects. The model couples the dislocation kinetic (transport) equations with crystal mechanics. This coupling is two-way. The dislocation density field is evolved as a result of motion induced by the Peach and Koehler force resulting from the local stress field in the crystal. This evolution leads to accumulation of plastic strain, which is treated as an eigenstrain in the equations of crystal mechanics. The solution of the mechanics part thus depends on the evolution of the dislocations by incorporating the time dependent or evolving eigenstrain. The loop is closed by using the resulting local stress to compute the local Peach and Koehler force that drives the dislocation field evolution further.

This dissertation is arranged as what follows. Chapter 2 presents a review on relevant works including experiments, discrete dislocation dynamics models, and continuum dislocation models. The previous results regarding dislocation patterning are also included. Starting from chapter 3, we introduce the continuum model along with its numerical solution strategy and illustrate elementary solutions. As the solution requires cross slip rates as input, a methodology of deriving such rates from discrete dislocation dynamics is presented in Chapter 4. As shown, this calibration process leads to

significant improvement of the model predictions of the stress-train behaviour and patterns. In chapter 5, the model results for monotonic loading are presented including dislocation patterning, the influence of cross-slip, and the effect of crystal orientation. Chapter 6 extends the application of the continuum model to the simulation of dislocation patterns and hysteresis under cyclic loading. A summary of the current research, its significance and a future outlook are finally presented in Chapter 7.

CHAPTER 2. RESEARCH BACKGROUND

This chapter presents a concise review of experimental results and models related to the current work. The dislocation patterns obtained from experiments are reviewed first, followed by discrete and continuum dislocation dynamics models along with some results that illustrate the importance of the modelling approach used in this dissertation.

2.1 Dislocation Patterns in Experiments

Dislocation patterning has been widely reported in the experimental literature. The concentration of dislocations into dense and poor areas is mainly because such a patterning is energetically appealing to dislocations than a homogeneous distribution. There are also kinetic and kinematic factors influencing this patterning or self-organization of dislocations. In the case of monotonic loading, the patterns of dislocations show dependence on the orientation of the crystal [74–76]. In general, dislocation walls are inclined to be parallel with the crystallographic planes which have relatively higher Schmid factor than the other planes [75], which is more pronounced in the single-slip cases. In the case of multislip situation, where several crystallographic systems may have about the same in Schmid factor, dislocations tend to form cells whose walls that may (in the cases of [110] and [111] type loading) or may not (in the case of [001] type loading)

parallel to any of crystallographic planes. In references [74,75] , dislocation patterns are grouped into three types shown in figure 2.1.

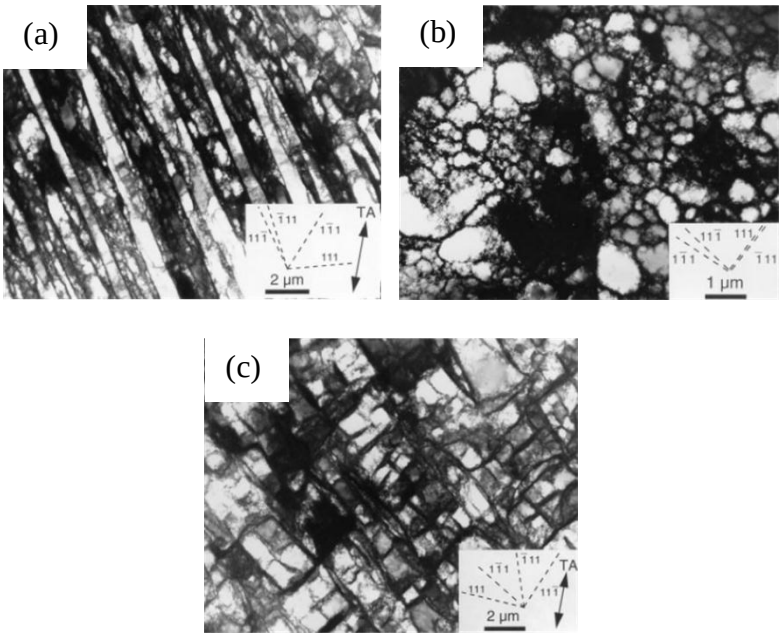

Figure 2.1. Orientation dependence of dislocation patterns, adopted from [75]: (a) Type 1 structure appears in the loading direction which favours the activation of single slip system, (b) Type 2 cell structure appears in crystals oriented around [001] direction, and (c) Type 3 cell structure appears in crystals near [111] direction.

Type 1 structure (plotted in figure 2.1(a)) is often observed in single slip crystals in which dislocation walls are evidently parallel to the traces of slip planes on the selected sections. Type 2 structure is an isotropic cell structure which is found in [001] crystals (shown in figure 2.1(b)). Type 3 structure is also cell structure, but in which the walls show the inclination of being parallel with traces of slip planes (see figure 2.1(c)).

A considerable amount of works has been done to analyse the property of these patterns. The cell structure of dislocation-dense walls is analysed geometrically to yield the fractal dimension of the pattern and its relationship with strain-hardening process [77,78]. A positive power law relationship has been established between fractal dimension and flow stress for different orientations of copper single crystals [78]. The size of dislocation-depleted area (interior cell size), on the other hand, defines the wavelength of dislocation structure [79,80]. Experiments [81–85] have revealed the relationship between wavelength and the hardening stress, yielding the famous similitude law [48,86,87].

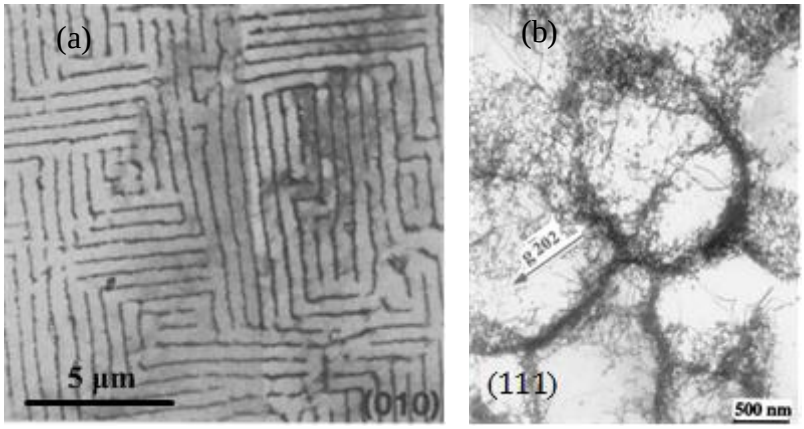

Figure 2.2. Dislocation structure in fatigued copper single crystals oriented for multislip: (a) labyrinth structure in [001] crystals, adopted from [44], and (b) cell structure in $[\bar{1}12]$ crystals, adopted from [88].

The dislocation patterns for a cyclically deformed crystal vary to quite an extent with a number of factors including the orientation of crystal [88,89], the amplitude of plastic deformation [89–91], and the temperature [92]. The pattern composed of vein-

channel and ladders, as shown in figure 1.2(a), is typically observed in the grains oriented for single slip [93]. The multislip cyclic loading around [001] facilitates the formation of well-saturated labyrinth structure consisted of dislocation walls perpendicular and parallel to the loading direction [94]. A compilation and analysis of orientation dependence of dislocation patterns is made in [95]. The amplitude of plastic strain has its consequence on the final saturation stress [96] and also the type of dislocation patterns [90]. Figure 2.2 shows labyrinth structure and cell structure in fatigued single crystals oriented for multislip.

2.2 Dislocation Dynamics Simulations

Discrete dislocation dynamics models were first proposed in 1980s. They aim to simulate the evolution of discretized dislocation lines embedded in the elastic medium [97]. A few models were developed, which differ in such factors as the dimension, the methods of discretization of dislocation lines, the treatments of boundary conditions and the implementation of short range reactions. 2D dislocation models were developed first. These models treat infinitely long, straight and parallel dislocation lines or either pure screws or pure edges character [98]. Multiple gliding planes can be taken into account [99] and many features that originate from 3D configuration can be borrowed from the analysis of curved dislocation lines in 3D space [100]. Despite its oversimplification, 2D models are still within the options of dislocation models and applied to monotonic loading [66], fatigue [101] and crack simulations [102]. While these models served as a starting point, they are still in use. However, they will not be discussed further in order to concentrate on 3D models, which are more relevant to the current work.

2.2.1 The ‘microMegas’ Model

In 1990s, Kubin *et al.* proposed a model [103] which leads to the later development of the ‘microMegas’ code [104]. The model is characterized by lattice based discretization of dislocations in which the dislocation segments may take on a finite number of directions [64,105]. As such, the gliding directions, which are normal to the segments, are also confined to a certain number of directions on slip planes. In this manner, a continuous dislocation line can be approximated by a succession of straight segments comprised only of screws and edges, which is schematically plotted in figure 2.3(a) for a loop. A refinement has been made on the discretization of segments from four directions (edges and screws in both directions) to eight directions with the addition of mixed type segments, which is plotted in figure 2.3(b). Further refinement of more prescribed directions is possible but the overall enhancement saturates fast [104].

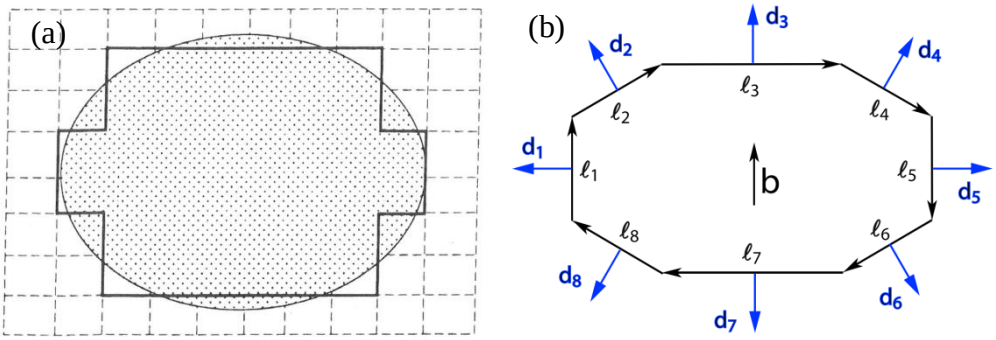

Figure 2.3. Discretization of a dislocation loop in the microMegas model in (a) a pure edge and screw scheme, adopted from [106] and (b) a refined eight directions model, adopted from [104].

The force applied to a dislocation segment includes a number of components [106]. The external force depends on the loading and the properties of segments, Burgers vector and line direction. Internal force exists because of the long-range feature of the mutual interaction between dislocations. It is summed over the contributions from all dislocations except the neighbouring ones [106]. Line tension, caused by the neighbouring segments, is a virtual force reflecting the tendency of dislocation lines to decrease their curvature [104]. Image forces are also applied, which depend on the type of the boundary condition.

The relationship between the force and the velocity is specified by a number of rules [104]. Short range reactions are explicitly modelled for annihilation and dipole formation. In the model implemented in microMegas, the new formed segment of junction is regarded as nothing but the intersecting part of its parent segments. The work of controlling junction formation is left for the stress field to determine whether to zip or unzip the two parent segments. All junctions are treated as sessile and glissile junctions are not considered [104]. The performance of microMegas model shows great agreement with experiments and it has been used in many types of simulations [107–111].

2.2.2 The ‘ParaDis’ Model

In 1990, Hirth *et al.* [112,113] proposed a 3D dislocation dynamics model which at a later point motivated the development of the ParaDis code [114]. In the latter, the discretised segments of dislocations can be oriented in arbitrary directions in 3D, as shown in figure 2.4(a). The network is updated by changing the positions of the nodes as

well as by adding or subtracting the nodes if necessary [115]. In this method, the movement of segments is not confined to any prescribed directions as is in microMegas.

The Peach-Koehler force is evaluated for each segment within the network by summing the contributions of Peach-Koehler force from all the other segments:

$$F_{iseg} = \sum_{jseg=1,\, j\neq iseg}^{N_{\text{seg}}} F_{jseg}^{PK} + F_{\text{app}}^{PK}, \tag{2.1}$$

where F_{iseg} is the total force on segment $iseg$, F_{jseg}^{PK} the Peach-Koehler force contributed by segment $jseg$, N_{seg} total number of segments, F_{app}^{PK} the Peach-Koehler force caused by the applied stress field.

Then the segment forces are distributed to the nodes based on a linear interpolation, as shown in figure 2.4(b). The scenario now can be described as a collection of nodes $\{\mathbf{r}_i, i = 1, 2, ..., N_{\text{node}}\}$ associated with a collection of nodal forces $\{\mathbf{F}_i, i = 1, 2, ..., N_{\text{node}}\}$. The motion of the one point on a segment is locally described by [115]:

$$\mathbf{f}^{\text{drag}}(\mathbf{x}) = -\mathbf{B}(\boldsymbol{\xi}(\mathbf{x}))\mathbf{v}(\mathbf{x}), \tag{2.2}$$

where $\mathbf{f}^{\text{drag}}$ is the dragging force at point $\mathbf{x}$, $\mathbf{v}(\mathbf{x})$ the velocity, $\mathbf{B}(\boldsymbol{\xi}(\mathbf{x}))$ the tangent dependent drag coefficient matrix which contains gliding, cross-slip, climbing information in it, $\boldsymbol{\xi}(\mathbf{x})$ the tangent at point $\mathbf{x}$. Once the virtual work principle is applied to the configuration of the network [116], the relationship between nodal velocities and nodal forces are obtained as follows [115]:

$$\sum_j \mathbf{B}_{ij}\mathbf{v}_j = \mathbf{F}_i \,, \tag{2.3}$$

where i and j are nodal indexes, $\mathbf{v}_j$ the nodal velocity, $\mathbf{B}$ is global stiffness matrix which should not be confused with $\mathbf{B}(\boldsymbol{\xi}(\mathbf{x}))$ in equation (2.2). Equation (2.3) is a set of linear equations which are solved at each time step to determine the nodal velocities.

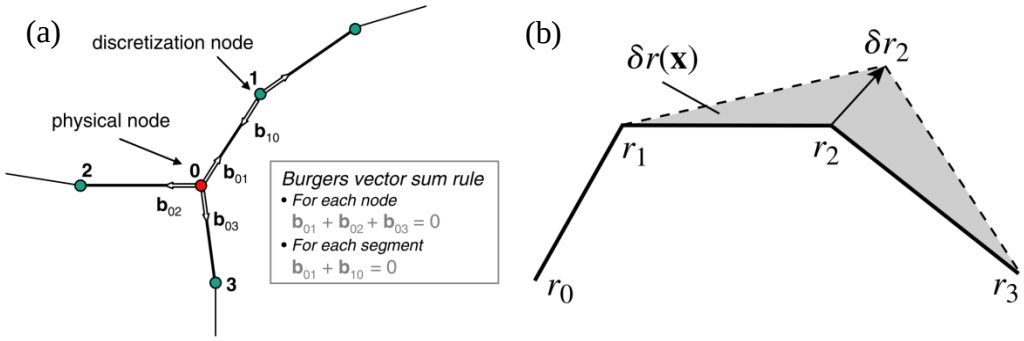

Figure 2.4. A schematic of the discretization method of dislocation lines in ParaDis model (a) and the calculation of forces for each node (b). The dislocation network consists of arbitrarily oriented segments which are connected by nodes at the end of each segment. Burgers vector is conserved through the network. The forces are associated with nodes in the way that the nodal force is computed as a weighted average of two neighbouring segment forces. (a) is adopted from [114] and (b) is adopted from [115].

The topological information of the network is kept and modified through the simulation. New nodes are added to a segment if its length surpasses a prescribed upper limit and old nodes are deleted if the segment is too short. The short range reactions are implemented when the distance between dislocation segments is below a prescribed limitation, only above which the elastic field holds. A new segment is produced by the

two reacted segments in the way that the Burgers vector of the new one is the sum of its ‘parents’. Both sessile and glissile junctions are represented by monitoring the Burgers vector of the newly generated segments. Some applications of the ParaDis model can be found in [117–119].

2.2.3 Parametric Discrete Dislocation Dynamics Models

It is a common feature in microMegas model and in ParaDis models that the curved dislocation lines are discretized into straight lines. Such is not the case in some other models. Ghoniem proposed a model in which the discretized segments are curved cubic hermit splines [120], see figure 2.5. The tangent on each segment are differing from point to point and are dependent on the parameter w, ranging from 0 to 1, see figure 2.5(b). One of the main features of the model is its efficiency in calculating the elastic stress field of complex shape ensembles of dislocations by using a fast numerical quadrature sum [120]. Generalized coordinates are used for obtaining the motion of the curved segments by applying a variational principle. One of the merits of this model is that it reduces the computational burden by allowing more freedom of a segment in both length and shape.

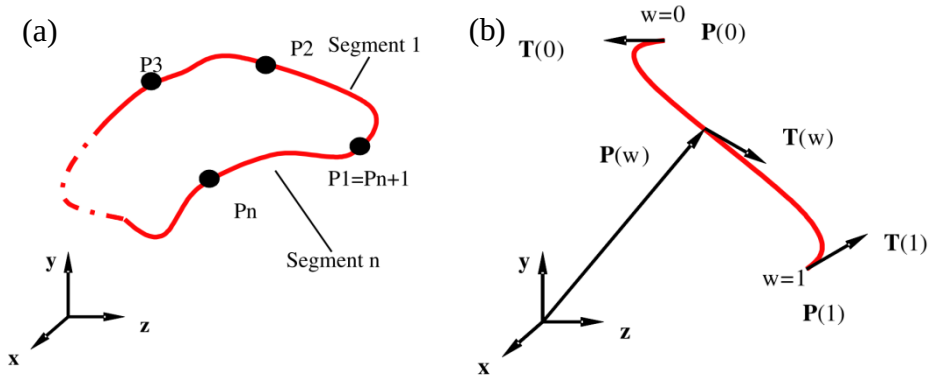

Figure 2.5. Parametric model of discrete dislocation dynamics: (a) ensemble of segments, and (b) a single curved dislocation segment. Adopted from [121].

2.2.4 Comments on Discrete Dislocation Models

Discrete dislocation dynamics (DDD) has achieved a considerable amount of results that explain experimental results to various degrees. The method is originally proposed two decades ago by Amodeo and Ghoniem [97] and Canova and Kubin [122]. The DDD model is widely used for different types of loading conditions for different types of crystals [118,123–127]. The simulations of fatigue and crack propagation are also realized by the discrete models [102,128–130]. Not only are the simulated results agree with experiments but also the simulations reveal the mechanisms underlying the observable phenomena [33,131,132].

Despite the great achievements accomplished by discrete dislocation dynamics, the intrinsic dependence on the tracking of dislocation lines makes the method expensive in computation, which deteriorates its performance when the dislocation density increases with strain [113,133] in a linear or even super-linear manner. An alternative option is

continuum dislocation dynamics, in which dislocations are represented by density fields that evolve in space and time. The following section reviews the progress in developing continuum dislocation dynamics models.

2.3 Continuum Dislocation Dynamics Models

The thought of considering dislocations as continuously distributed can be dated back to Nye [134] who first proposed the dislocation density tensor and related it with the lattice curvature. Kröner [135] continued to clarify the presence of dislocation density tensor as a result of incompatible plastic distortion within the crystal. Kondo [136] and Bilby [137] constructed the differential geometry theory for single dislocation lines. Although were not successful in predicting plasticity, these early works paved the road toward the modern continuum dislocation dynamics formulations discussed below.

2.3.1 Acharya's PMFDM Model

Based on the idea of curl relationship between dislocation density and plastic distortion tensors, Acharya and coworkers [69,138,139] proposed field dislocation mechanics (FDM) in which equations governing the evolution of the dislocation field (represented by a tensor) and the crystal mechanics take on the form:

$$\begin{aligned}
&\nabla \times \boldsymbol{\chi} = \boldsymbol{\alpha} \\
&\nabla \cdot \boldsymbol{\chi} = 0 \\
&\nabla \cdot (\nabla \dot{\mathbf{z}}) = \nabla \cdot (\boldsymbol{\alpha} \times \mathbf{v}) \\
&\nabla \cdot \left[C : \left(\nabla (\mathbf{u} - \mathbf{z}) + \boldsymbol{\chi} \right) \right] = 0 \\
&\dot{\boldsymbol{\alpha}} = -\nabla \times (\boldsymbol{\alpha} \times \mathbf{v}) + \mathbf{s}
\end{aligned} \quad . \tag{2.4}$$

where $\boldsymbol{\alpha}$ is dislocation density tensor, $\boldsymbol{\chi}$ the incompatible part of the elastic distortion tensor, $\mathbf{v}$ the dislocation velocity vector, $\mathbf{u}$ the total displacement, $\mathbf{z}$ the perturbed displacement due to the incompatible part of elastic distortion, $\mathbf{s}$ the nucleation rate tensor of dislocations. The first equation in (2.4) is derived by Kröner for the definition of dislocation density tensor [140]; the second equation imposes a divergence free constraint on $\boldsymbol{\chi}$; the third equation is Orowan's law written in a tensor format continuous fields; the fourth equation is the equilibrium equation for stress field; the last equation is the kinetic equation for $\boldsymbol{\alpha}$.

Apparently, physical fields listed in (2.4) are coupled in the way that the second-order tensor $\boldsymbol{\alpha}$ acts as a central role. Equation (2.4) is not closed due to the unspecified parameters $\mathbf{v}$ and $\mathbf{s}$. In the implementation, the theory is closed with constitutive designation of the velocity field $\mathbf{v}$ and the nucleation term $\mathbf{s}$ by borrowing relationships from crystal plasticity [63]. Such a constitutive specification renders the model phenomenological [141]. Acharya's model demonstrates the applicability of the curl type kinetic equations on the mesoscale level. The model delivers good results in agreement with experiments for a 3D cube where a single slip system is activated [138].

2.3.2 Sethna's Model

In the same line but without any phenomenological prescription, Limkumnerd and Sethna [70,142] developed a mesoscale theory where the evolution equation for dislocation density tensor is given by the flux term of Burgers vector [143]:

$$\frac{\partial}{\partial t}\rho_{ik} = -\varepsilon_{ijq}\partial_j J_{qk}, \tag{2.5}$$

where ρ_{ik} is the second order density tensor, amounting to $\boldsymbol{\alpha}$ in equation (2.4) in Acharya's model; J_{qk} is flux tensor which in a sense amounts to $\boldsymbol{\alpha}\times\mathbf{v}$ in the last one of equations (2.4). The flux is related to the plastic distortion β_{ij}^{P} tensor in the following way [143]:

$$\frac{\partial \beta_{ij}^{\mathrm{P}}}{\partial t} = J_{ij}, \tag{2.6}$$

where β_{ij}^{P} amounts to $\boldsymbol{\chi}$ in Acharya's model. The plastic distortion tensor β_{ij}^{P} is solved by variational principle which is expressed mathematically [143]:

$$\frac{\partial}{\partial t}\beta_{ij}^{\mathrm{P}} = -\Gamma\frac{\delta F}{\delta \beta_{ij}^{\mathrm{P}}}, \tag{2.7}$$

where F is a functional of β_{ij}^{P} representing the free energy (elastic energy) induced by stress field, Γ the material dependent constant. β_{ij}^{P} is eventually dependent on stress tensor which can be related to dislocation density tensor but in Fourier space [70]:

$$\tilde{\sigma}_{\alpha\beta}(\mathbf{k}) = K_{\alpha\beta\mu\upsilon}(\mathbf{k})\tilde{\rho}_{\mu\upsilon}(\mathbf{k}), \tag{2.8}$$

where $K_{\alpha\beta\mu\upsilon}$ is a function of position $\mathbf{k}$ in Fourier space. The stress field in equation (2.8) is both expressed and solved in Fourier space during the simulation. It can be seen that to some degree that Sethna's model shares some features with Acharya's model in terms of

the curl relationship between plastic distortion and dislocation density tensor, but they differ in the constitutive closure [143]. The model is applied to simulate the relaxation of an initially plastically distorted cube, where fractal features were found to form.

2.3.3 Diffusion-reaction Type Model

In analogy to the chemical process, The model proposed by Walgraef and Aifantis [68,144,145] describes dislocation system in diffusion-reaction type equation which reads [68]:

$$\partial_t \rho + \nabla \cdot \mathbf{J} = R(\rho), \tag{2.9}$$

where ρ is the scalar field of dislocation density, $\mathbf{J}$ the flux term denoting diffusion of dislocations, $R(\rho)$ the production or annihilation term which denotes reactions. The total density ρ is divided into immobile and mobile components which are governed by their respective equations expressed in the form [145]:

$$\begin{aligned} \partial_t \rho_I + \nabla \cdot \mathbf{J}_I &= R_I(\rho_I, \rho_M) \\ \partial_t \rho_M + \nabla \cdot \mathbf{J}_M &= R_M(\rho_I, \rho_M) \end{aligned}, \tag{2.10}$$

where ρ_I and ρ_M , $\mathbf{J}_I$ and $\mathbf{J}_M$, R_I and R_M are immobile and mobile dislocation densities, flux terms, reaction terms respectively. When specifying the flux term $\mathbf{J}_I$, which describes the motion of dislocations, the model appeals to crystal plasticity expression for velocity, which is written in power law relationship [145]:

$$V = V((\tau_0 / \tau)^m), \tag{2.11}$$

where V represents velocity which turns out to be dependent on the ratio between critical shear stress τ_0 and resolved shear stress τ.

The diffusion-reaction type model has been successful in predicting the patterns in cyclic loading as persistent slip bands [146] and labyrinth [147] structures seen in experiments.

2.3.4 Statistical Models

In the late 90s, Groma and Zaiser [148–150] applied statistical mechanics to analyse the system of straight parallel edge dislocations, ending up with the kinetic equation of advection-reaction type. The governing equations of dislocation density scalar in their model can be written in the following form [149]:

$$\begin{aligned} &\frac{\partial}{\partial t}\rho(\mathbf{r}) + \nabla_{\mathbf{r}}(B\mathbf{b}\tau(\mathbf{r})k(\mathbf{r})) = f(\rho,\tau,...) \\ &\frac{\partial}{\partial t}k(\mathbf{r}) + \nabla_{\mathbf{r}}(B\mathbf{b}\tau(\mathbf{r})\rho(\mathbf{r})) = 0 \end{aligned}, \tag{2.12}$$

where $\nabla_{\mathbf{r}}$ denotes the spatial gradient, B the dislocation mobility [148], $\mathbf{b}$ Burgers vector, $f(\rho,\tau,...)$ source term. ρ and k correspond to total and geometrically necessary dislocation densities respectively [151] and they are expressed as:

$$\begin{aligned} \rho &= \rho_+ + \rho_- \\ k &= \rho_+ - \rho_- \end{aligned}, \tag{2.13}$$

where ρ_+ and ρ_- are densities of dislocation with positive and negative Burgers vectors respectively. The second terms on the left hand side of equation (2.12) is first-order

spatial derivative of density which reflects advection, in contrast to diffusion-reaction model in which the second order differentiation is applied to density quantity.

The numerical implementation of Groma's model delivers results in good comparison with discrete dislocation models [152] and predicts a certain dislocation patterns [149]. However, the availability of the kinetic equation was limited to 2D case until El-Azab [72,117] formulated a general 3D statistical modelling. El-Azab pointed out that the dislocations on given slip system can be described by a scalar field in multi-dimensional phase space, which can be described by a kinetic equation of the form [72]:

$$\left(\frac{\partial}{\partial t}+\mathbf{v}\cdot\nabla_{\mathbf{x}}+\dot{\mathbf{v}}\cdot\nabla_{v}\right)\phi(\mathbf{x},\mathbf{v},\theta,t)=S(\mathbf{x},\mathbf{v},\theta,t), \tag{2.14}$$

where ϕ is the scalar dislocation density at point $(\mathbf{x},\mathbf{v},\theta,t)$ in the phase space which is spanned by the generalized coordinates of position, $\mathbf{x}$, orientation, θ, velocity, $\mathbf{v}$, and time, t. The source term S appears on the right hand side of equation (2.14) to take into account the annihilation, multiplication, short-range reactions, and cross-slip. The operator $\nabla_{\mathbf{x}}$ represents spatial gradient, describing dislocation transport while ∇_{v} represents gradient but in velocity phase space. Taking the zeroth order velocity moment of the last equation leads to kinetic equations describing the density field of dislocations in each slip system [153]. A stochastic procedure [107,154,155] has been applied to data from discrete dislocation dynamics simulation to determine the source terms in the kinetic equations for the density.

2.3.5 Hochrainer's Model

Motivated by El-Azab's approach, Hochrainer [156] and co-workers [156–158] developed the continuum model that favours the representation of dislocations of multi-direction and multi-curvature at one single spatial point. In this approach, Kröner's second order dislocation density tensor is generalized into a tensor field in 4D space in which the real space is supplemented by an angular dimension denoting dislocation orientation. Figure 2.6 plots a 2D loop extended into 3D space, where the vertical axis represents the angular dimension ranging from 0 to 2π [158].

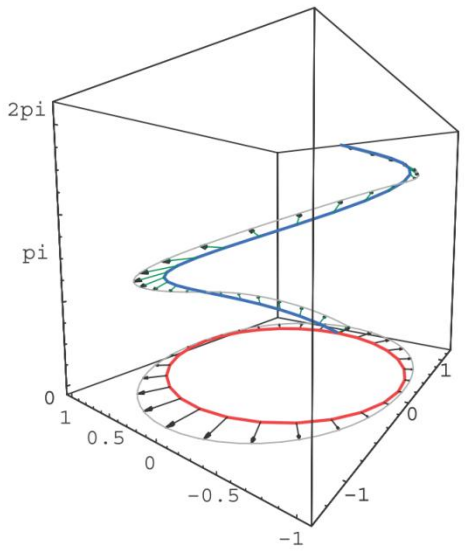

Figure 2.6. A continuous curve (in red) physically located on 2D plane is 'lifted' to 3D configuration space, forming a 'spiral' shape (in blue). The vertical axis is the angular dimension. The arrows on the curves show the generalized velocity field. Adopted from [158].

A generalized second order density tensor $\boldsymbol{\alpha}^{\mathrm{II}}$ is introduced, which plays a central part in the model [157,159]. Its definition is given by [159]:

$$\boldsymbol{\alpha}^{\mathrm{II}} = \rho(\mathbf{p},\varphi)\mathbf{L}(\mathbf{p},\varphi)\otimes\mathbf{b}\,, \tag{2.15}$$

where $\mathbf{p}$ and φ are coordinates in real space and in angular space, respectively; ρ is scalar density and $\mathbf{L}$ is the tangent of dislocation line; $\mathbf{b}$ is Burgers vector. Equation (2.15) is similar in the form to the earlier work by Nye for the definition of second order dislocation density tensor [134]. The evolution equation for the model reads [159]:

$$\begin{aligned} \partial_t \rho &= -\hat{\nabla}\cdot(\rho\mathbf{V}) + qv \\ \partial_t q &= -\hat{\nabla}\cdot(q\mathbf{V}) - \rho\hat{\nabla}_{\mathbf{L}}\hat{\nabla}_{\mathbf{L}} v \end{aligned}, \tag{2.16}$$

where $\mathbf{V}$ and v are generalized and scalar velocity respectively, q the curvature; $\hat{\nabla} = \nabla + \partial_\varphi$ denotes the differential operation in the higher dimension space.

The addition of an orientation dimension makes possible multiple directions of dislocation lines at a single point. In principle, the model is closely related to the statistical model proposed by El-Azab but the dislocations in the later one are described in scalar quantity. It must be noted that the price for the lift in dimension is the computational burden which can however be avoided following the procedure described in [159]. Hochrainer's model was implemented for some simplified cases such as micro-bending [158] and mechanical annealing [159]. 2D patterns were shown to form in a minimal model of continuum dislocation plasticity based on Hochrainer's dislocation density tensor [160] but 3D results are yet to be demonstrated.

2.3.6 The Phase Field Model

Koslowski proposed the phase field model from the angle of the energy of dislocation evolution during elasto-plastic process [161]. The principle of minimization of energy leads to the problem [161]:

$$\inf_{\varsigma \in Y} \inf_{\xi \in X} E[\varsigma \mid \xi], \tag{2.17}$$

where function $\varsigma(\mathbf{x})$ is normalized slip distribution, $\xi(\mathbf{x})$ represents the number of dislocations that have ever passed over point $\mathbf{x}$, X and Y the configuration space of phase fields and slip fields respectively [73]. The functional E in equation (2.17) is the total energy given by:

$$E[\zeta \mid \xi] = \int \frac{\mu b^2}{2d} |\zeta - \xi|^2 \, d^2x + \frac{1}{(2\pi)^2} \int \frac{\mu b^2}{4} K \left|\hat{\xi}\right|^2 d^2k - \int b\mathbf{t} \cdot \mathbf{m} \zeta d^2x, \tag{2.18}$$

where μ is the shear modulus, b the Burgers vector, d the interplanar distance, $\mathbf{t}$ the traction on the slip plane caused by external stress, and $\mathbf{m}$ the normal to the slip plane. $\hat{\zeta}$ denotes the Fourier transformation of ζ. In equation (2.18), the first integration represents the core energy, the second one is the elastic interaction energy, and the last one is the energy of the external system of forces.

The phase field model has demonstrated its ability in predicting dislocation patterns under monotonic and cyclic loading conditions [161] as well as for single and multiple slips [73]. Scaling laws are also revealed from the simulation by this model [162]. Its application even extends to the simulation of non-metallic materials [163].

2.3.7 Comments on Continuum Models

The continuum dislocation dynamics models were proposed earlier than the discrete models and still remain to be an active research area. The common feature shared by all the types of continuum models is the governing equation(s) which describe the evolution of continuous fields which can be scalar(s), vector(s), or tensor(s), in 3D or higher dimension space. Unlike discrete models, the forms governing equation(s) differ a lot among the continuum models mainly because of the differences in representing the dislocation systems.

A great amount of progress has been realized by continuum models. For example, it is well known in experiments that crystalline materials show size effects at small scales [164–168]. This characteristic has been successfully predicted by continuum models [138]. The continuum model also predicts dislocation patterns that are in agreement with experiments in many situations [143,147,160,161,169], which will be presented in the section follows.

2.4 Dislocation Patterns in Simulations

This section is concerned with dislocation patterns obtained from the above mentioned discrete and continuum dislocation dynamics models. It will be seen that the discrete dislocation dynamics models can predict patterns but the continuum models do not yet make prediction of patterns consistent with 3D bulk plasticity.

2.4.1 Dislocation Patterns in Discrete Models

It was noticed earlier that even in some simplified 2D models [170,171] or 2.5D [99], dislocations organize into patterns with a certain measurable wavelength which delivers scaling laws [99]. Figure 2.7 shows a patterned edge dislocation ensemble under cyclic ((a)) and monotonic ((b)) loading conditions. Under cyclic loading circumstance, dislocation walls composed of edge dipoles arrange vertically along *y*-axis; while monotonic loading seems to facilitate the formation of cells whose walls are in parallel with slip systems.

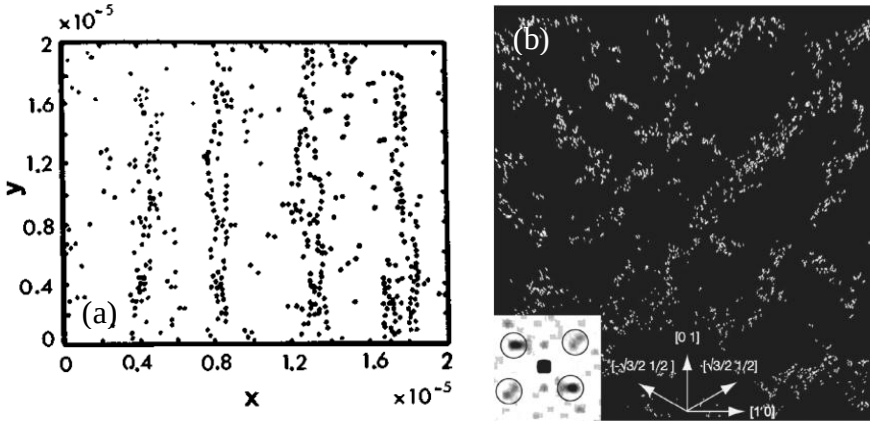

Figure 2.7. Dislocation patterns in (a) 2D and (b) 2.5D simulations: (a) cyclic loading and (b) monotonic loading. The model in (b) includes 2 slip systems. In both images, inhomogeneous and isotropic arrangements of edge dislocations emerge to form into certain patterns composed of dislocation-free and dislocation-dense areas. (a) is adopted from [171] and (b) is adopted from [99].

The implementation of 3D discrete models also predicts dislocation patterns under different loading conditions, as shown in figure 2.8. Dislocations tend to be arranged along some preferred crystallographic directions which could be the traces of slip planes

on the sliced sections. The model leading to the pattern shown in figure 2.8(a) activates only two slip systems and the crystal is subjected to cyclic loading. The model delivering the pattern in figure 2.8 (b) activates multiple slip systems for a monotonically loaded single crystal.

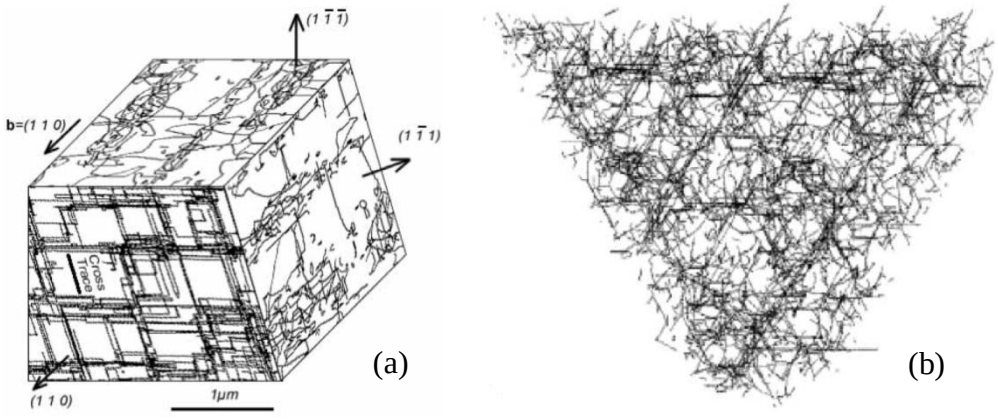

Figure 2.8. Dislocations organize into patterns under (a) cyclic loading and (b) monotonic loading conditions in 3D. (a) is adopted from [128] and (b) is adopted from [172].

2.4.2 Dislocation Patterns in Continuum Models

The diffusion-reaction type model predicts the evolution of dislocations from a random initial state to a labyrinth structure that is observed in fatigue experiments [44,47,90]. A comparison between simulation and TEM images is plotted in figure 2.9. It is to be noted that the diffusion-reaction model predicts dislocation walls oriented along slip planes, while in experiments the walls are along the directions parallel or vertical to [001] loading axis [89], which might be attributed to the lack in the model to include some

reactions. So crystallographically, the model and experiment are not in agreement. Moreover, while the experimental pattern occurs as a result of dislocation self-organization in 3D, the model solves equations in a 2D domain, ignoring all 3D effects. The comparison must thus be considered with some care about the differences.

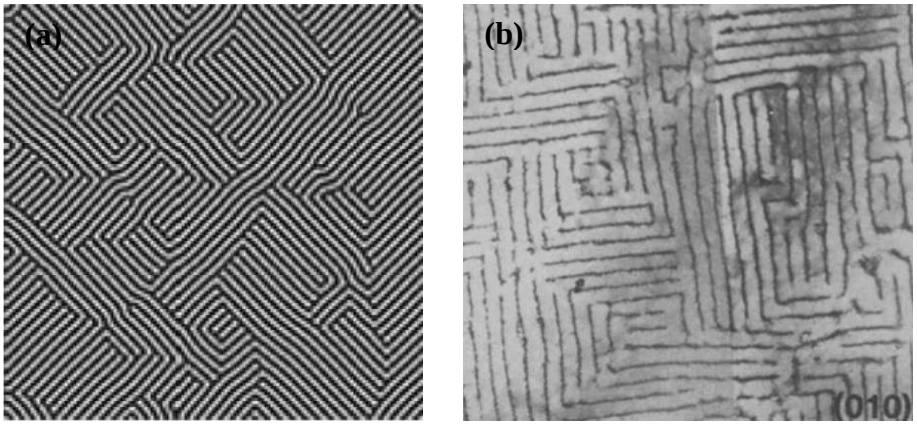

Figure 2.9. Labyrinth structure of dislocations shown from (a) reaction-diffusion model and (b) experiment. The labyrinth structure shows good agreement between TEM images and simulations in shape but not in the orientation. (a) is quoted from [147] and (b) is from [44].

Cell structures are conspicuous in monotonically loaded single crystals especially when multiple slip systems are activated (see figure 2.10(b)). The continuum models also demonstrate their ability in reproducing some patterns. The relaxation process of an initially distorted crystal is simulated by Sethna's model, yielding the fractal structure plotted in figure 2.10.

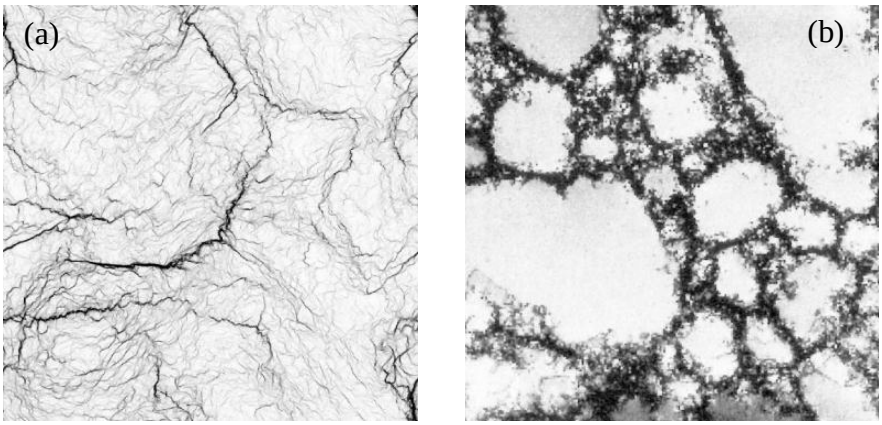

Figure 2.10. Comparison of dislocation distribution between (a) continuum simulation and (b) TEM images. (a) plots GND density from Sethna's model and (b) is obtained from copper single crystal loaded along [001] to the stress of 76.5MPa. Striking resemblance is shown between modelling and experiments. Both are adopted from [143].

Sandfeld [160] observed dislocation patterning by solving Hochrainer's model in 2D where the specimen is subjected to external loading. The difference between figure 2.10 and 2.11 in physics is that the former numerical example does not apply external loading but the later one does. The cells formed under loading conditions [160] have closed walls and resemble those observed in experiments to a more extent than the unloaded case [143]. Relevant fields obtained from Hochrainer's model are shown in figure 2.11. Although a similarity between simulation and experiment is observed when one compares figure 2.11 and figure 2.1(b), this observation is hard to explain as the model simulates a single slip situation, which is known experimentally to not yield cellular struture.

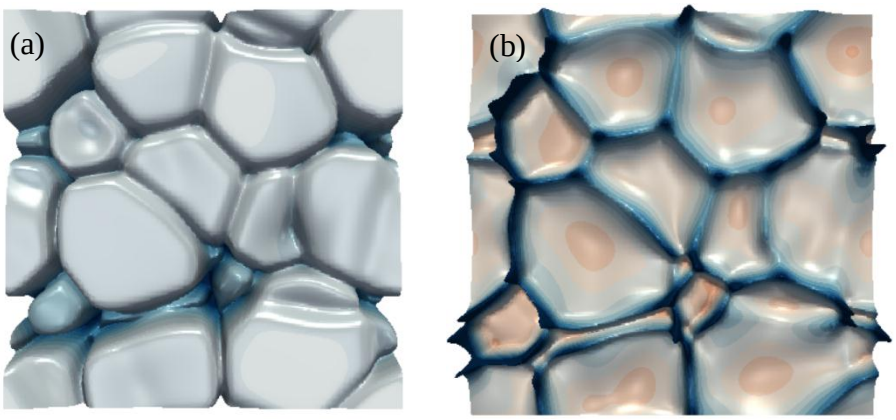

Figure 2.11 Total dislocation density (a) and scaled curvature density (b) in 2D simulations using Hochrainer's model. Adopted from [160].

2.5 Motivation of the Current Research

In general, the discrete dislocation dynamics simulation approach aims to track the evolution of discrete systems of dislocations in space and time. The geometrically increasing burden in computation limits its application to larger domains (>10μm) and to longer simulation time. In order to avoid such computational limitations, some compromise, or simplification, has to be made by either reducing the number of slip systems [128] or reducing the density of dislocation segments [172], or by some other approaches. In attempting to avoid the increasing computational burden, however, discrete dislocation dynamics models may suffer idealizations that lead to discounting important physics.

Continuum modeling, on the other hand, oriented at an ultimate goal of general governing equations for physical fields, is relatively more immune from computational limitations. Yet the continuum modelling still requires significant progress. The PFMDF

model [141], which resorts to empirical rules, should be considered as an important effort in transition from crystal plasticity to dislocation dynamics. The same situation applies to diffusion-reaction model devoid of the advection which is an intrinsic feature of dislocations. Sethna's model [143] takes no phenomenological assumption and represents advection, but the lack of separation of dislocation density between different slip systems limits the capability of the model to capture the slip heterogeneity as well as detailed events of dislocation lines, such as cross-slip and short-range reactions. The models that employ expression in higher dimension space [72,157] raise a potential computational challenge which might become obvious when it comes to 3D simulation.

It is worthwhile to keep in mind that the discrete dislocation dynamics' advantage of accuracy in tracking individual dislocation segments and the merit of continuum model in computational cost (supposedly) can be combined to yield a hybrid model, as is realized by Zbib and co-workers [173–175]. In their model, the dislocation motion simulated at microscopic scale is coupled with the stress solved at macroscopic scale in such a way that the former provides the latter with plastic deformation that serves as eigenstrain [176] in equilibrium equation, presenting a typical example of multiscale modelling for materials. However, as long as the discrete simulation is still implemented and the long-range interaction between dislocation segments is still computed, the concern on the growing computational burden may not be cleared completely.

Motivated by the above-mentioned achievements in dislocation simulation and being aware of insufficiency in current models, a 3D continuum dislocation dynamics model is developed. This model couples the dislocation kinetics with crystal mechanics, stress equilibrium and deformation kinematics. A vector representation of the dislocation

density field is employed to encompass both the density magnitude and line orientation, which leads to kinetic equation of a curl type. The equation is closed by associated elastic boundary value problem where the plastic strain is treated as an eigenstrain field. The rate of cross-slip, which is used as a parameter in the continuum model, is obtained by discrete dislocation simulation, showing the general framework of embedding parameters from statistics of discrete dislocation simulation into the continuum model. The effectiveness of this continuum representation is demonstrated here by simulating the dislocation patterning under monotonic and cyclic loadings, showing that the model captures the main dislocation patterns observed in experiments. The results agree with experimental results and with results of previous simulations.

CHAPTER 3. CONTINUUM DISLOCATION DYNAMICS

In this chapter, the kinetic equations governing dislocation density evolution are developed and their connection with stress boundary value problem is accomplished by invoking the framework of crystal plasticity. The model is developed for small deformation situations. The chapter is arranged as follows: section 3.1 presents a detailed derivation of kinetic equations for dislocations; section 3.2 shows how the dislocation kinetics is closed with plasticity theory without resorting to phenomenological arguments; periodic boundary conditions are implemented in the model, which is presented in section 3.3; section 3.4 is dedicated to the numerical treatment of the equations.

3.1 The Kinetic Equations

Despite the discrete nature of dislocations, it is their large density that makes a continuum representation possible, which is an important postulate of the current work. The proposed model regards dislocations to be continuously distributed in the crystal and considers the linearized kinematics of small deformation. Since a vector representation of the dislocation density will be used, a first goal is to derive the equation of motion of dislocations with that representation in mind. In order to do so, we start with a single slip system and the tensor representation of dislocations at sufficiently small resolution, which will be clarified at a later point. For a reason that will be explained later, we

concentrate on dislocation bundles of the same Burgers vector before generalizing the formalism to arbitrary dislocation system. A bundle of dislocations is defined here as a set of continuously distributed dislocation lines of a given Burgers vector that have only one line direction at every point in space. Such bundles may fully lie on a single slip system or on two collinear slip systems in the case of cross-slip.

With the dislocation bundle picture in mind, the second order dislocation density tensor $\boldsymbol{\alpha}$, following Kröner's development [135], is defined in terms of the plastic distortion tensor $\boldsymbol{\beta}^{\mathrm{p}}$ by:

$$\boldsymbol{\alpha} = -\nabla \times \boldsymbol{\beta}^{\mathrm{p}}. \tag{3.1}$$

The time differentiation of equation (3.1) yields:

$$\dot{\boldsymbol{\alpha}} = -\nabla \times \dot{\boldsymbol{\beta}}^{\mathrm{P}}. \tag{3.2}$$

In the above, the rate of plastic distortion at a point in space can be obtained by Orowan's law, which presents in tensor form as [177]:

$$\dot{\boldsymbol{\beta}}^{\mathrm{p}} = -\mathbf{v} \times \boldsymbol{\alpha}, \tag{3.3}$$

where $\mathbf{v}$ is the dislocation velocity field. The above equation makes it possible to update the plastic distortion $\boldsymbol{\beta}^{\mathrm{p}}$ from the movement of dislocations. Insertion of equation (3.3) into equation (3.2) generates the equation for the time rate of change of the $\boldsymbol{\beta}^{\mathrm{p}}$ tensor through the velocity field $\mathbf{v}$,

$$\dot{\boldsymbol{\alpha}} = \nabla \times (\mathbf{v} \times \boldsymbol{\alpha}). \tag{3.4}$$

Because dislocations are spatial curves with line orientation, a vector field representation of their density field is appropriate, which is denoted by $\boldsymbol{\rho}$. Consider again a dislocation bundle with a unit tangent $\boldsymbol{\xi}$ at an arbitrary point on its slip plane. A scalar density ρ may also be defined such that

$$\boldsymbol{\rho} = \rho\boldsymbol{\xi}. \tag{3.5}$$

The dislocation density tensor $\boldsymbol{\alpha}$ given by equation (3.1) can be interpreted as tensor product of the dislocation density vector $\boldsymbol{\rho}$ and the Burgers vector $\mathbf{b}$ of the dislocation bundles [134],

$$\boldsymbol{\alpha} = \boldsymbol{\rho} \otimes \mathbf{b}. \tag{3.6}$$

The assumption that all dislocation lines in a bundle share a common Burgers vector makes the simplification of equation (3.4) in terms of the vector field $\boldsymbol{\rho}$ possible by exploiting expression (3.6). Substitution of the latter into the former yields

$$\dot{\boldsymbol{\rho}} \otimes \mathbf{b} = \nabla \times (\mathbf{v} \times (\dot{\boldsymbol{\rho}} \otimes \mathbf{b})). \tag{3.7}$$

It is shown below that the Burgers vector $\mathbf{b}$, which is a constant vector, drops from the above equation to yield an evolution law for the vector field itself. In doing so, equation (3.7) is first expressed using the Cartesian index notation,

$$\dot{\rho}_i b_j = e_{ipn} \partial_p (e_{nmk} v_m \rho_k b_j). \tag{3.8}$$

Applying the tensors on both sides of (3.8) to the vector $\mathbf{b}$ gives

$$\dot{\rho}_i b_j b_j = e_{ipn}\partial_p(e_{nmk}v_m\rho_k)b_j b_j \quad \rightarrow \quad \dot{\rho}_i = e_{ipn}\partial_p(e_{nmk}v_m\rho_k)\,. \tag{3.9}$$

Reverting back to the direct notation, equation (3.9) now reads:

$$\dot{\boldsymbol{\rho}} = \nabla\times(\mathbf{v}\times\boldsymbol{\rho})\,. \tag{3.10}$$

Equation (3.10) preserves the form of equation (3.4) and serves as the main kinetic equation that describes the motion of dislocations. The merit of equation (3.10) lies in the fact that it describes the bowing of a dislocation line and hence the line length increases in a natural way, and it can easily incorporate cross-slip and climb by allowing the direction of the velocity vector to change out of a glide plane and onto the cross-slip plane or normal to the slip plane, respectively. The physical process of dislocation annihilation is realized in the equation by the cancelling of $\boldsymbol{\rho}$ field with opposite directions. It is to be noted that equation (3.10) holds only for a dislocation bundle and cannot apply to a situation where multiple dislocation directions exist at a given point in space.

On the other hand, the plastic tensor $\boldsymbol{\beta}^{\mathrm{p}}$ in equation (3.3) can be expressed in the form:

$$\boldsymbol{\beta}^{\mathrm{p}} = \gamma\mathbf{S}\,, \tag{3.11}$$

where γ is the plastic shear strain and $\mathbf{S}$ is Schmidt tensor, $\mathbf{S} = \mathbf{n}\otimes\mathbf{b}/b$, with $\mathbf{n}$ being the unit normal to the slip plane and $\mathbf{b}$ the Burgers vector with magnitude b. The evolution law for the plastic slip is

$$\frac{\dot{\gamma}}{b}\mathbf{n} = -\mathbf{v}\times\boldsymbol{\rho}\,. \tag{3.12}$$

Equation (3.10) and equation (3.12) are used together in the model to evolve dislocation density field and eigen-distortion field simultaneously. The latter quantity is required in the elastic boundary value problem for the stress field.

The underlying idea of equation (3.10) is that the dislocation density vector $\boldsymbol{\rho}$ flows in the direction and at the magnitude of velocity $\mathbf{v}$, which enables the incorporation of cross slip. Assigning the dislocation density $\boldsymbol{\rho}$ to a particular slip system is then necessary. Incorporating cross slip then changes the kinetic equation to the form:

$$\dot{\boldsymbol{\rho}}_l = \nabla\times(\mathbf{v}_l\times\boldsymbol{\rho}_l) - \dot{\boldsymbol{\rho}}^{\mathrm{cs}}_{l\to l_*} + \dot{\boldsymbol{\rho}}^{\mathrm{cs}}_{l_*\to l}\,, \tag{3.13}$$

where $\boldsymbol{\rho}_l$ is dislocation density vector on slip system l, $\mathbf{v}_l$ is the glide velocity of dislocations on that slip system, $\dot{\boldsymbol{\rho}}^{\mathrm{cs}}_{l\to l_*}$ is the cross slip rate leaving from l to l^*, and $\dot{\boldsymbol{\rho}}^{\mathrm{cs}}_{l_*\to l}$ is the cross-slip rate in the opposite direction. The rate of cross-slip in the governing equation (3.13), $\dot{\boldsymbol{\rho}}^{\mathrm{cs}}_{l\to l_*}$ is expressed in the form

$$\dot{\boldsymbol{\rho}}^{\mathrm{cs}}_{l\to l_*} = \dot{p}^{\mathrm{cs}}_l\boldsymbol{\rho}^{\mathrm{cs}}_l = \dot{p}^{\mathrm{cs}}_l\boldsymbol{\rho}_l I(\boldsymbol{\zeta}^{\mathrm{cs}}_l)\,, \tag{3.14}$$

where $\dot{p}^{\mathrm{cs}}_l$ is the probability rate, $I(\boldsymbol{\zeta}^{\mathrm{cs}}_l)$ an indicator for screw dislocation which takes the value of 1 if the dislocation is screw and 0 if otherwise, $\boldsymbol{\zeta}^{\mathrm{cs}}_l$ the tangent of vector $\boldsymbol{\rho}_l$.

3.2 Crystal Plasticity

Up to now, equation (3.13) is open because the velocity fields are not yet determined. In a pure crystal, the velocity depends on the local stress and temperature. Previous models [139,158,178,179] either assume a form of the velocity or use phenomenological assumptions to close the kinetic equation (3.10). Such assumptions are useful but they introduce empirical parameters which requires experimental fitting. In this work, and without loss of generosity, only the glide motion of dislocations is considered for which the velocity magnitude is assumed to be linearly related to the resolved shear stress,

$$v = M\tau, \tag{3.15}$$

with M being a mobility coefficient and τ the resolved shear stress. This form applies to velocities on all slip systems where the resolved shear stress is computed from the following equation:

$$\tau = \boldsymbol{\sigma} : \mathbf{S} = (\boldsymbol{\sigma}\mathbf{n}) \cdot \mathbf{b} / b. \tag{3.16}$$

where $\mathbf{S}$ is the Schmid factor for the slip system characterized by slip plane normal $\mathbf{n}$ and slip direction: $\mathbf{b}/b$.

The stress tensor $\boldsymbol{\sigma}$ appearing in equation (3.16) is often decomposed according to sources into three parts: applied loads, image stress, long-range dislocation stress [174]. Regardless of how stress is handled, the total stress field satisfies the equilibrium equation

$$\nabla \cdot \boldsymbol{\sigma} = 0. \tag{3.17}$$

The stress field is equal to elastic tensor $\mathbf{C}$ times elastic strain, $\boldsymbol{\varepsilon}^{\mathrm{e}}$, via Hooke's law: $\boldsymbol{\sigma} = \mathbf{C} : \boldsymbol{\varepsilon}^{\mathrm{e}} = \mathbf{C} : (\boldsymbol{\varepsilon}^{\mathrm{tot}} - \boldsymbol{\varepsilon}^{\mathrm{p}})$. The elastic strain itself is the difference between the total strain, $\boldsymbol{\varepsilon}^{\mathrm{tot}}$, and the plastic strain, $\boldsymbol{\varepsilon}^{\mathrm{p}}$. Therefore, equation (3.17) can be expressed as

$$\nabla \cdot [\mathbf{C} : (\boldsymbol{\varepsilon}^{\mathrm{tot}} - \boldsymbol{\varepsilon}^{\mathrm{p}})] = 0, \tag{3.18}$$

where $\boldsymbol{\varepsilon}^{\mathrm{p}}$ is regarded as eigenstrain field [176] which is given by the summation of plastic strain of all slip systems,

$$\boldsymbol{\varepsilon}^{\mathrm{p}} = \mathrm{sym}\, \boldsymbol{\beta}^{\mathrm{p}} = \mathrm{sym} \sum_{l=1}^{N_{\mathrm{ss}}} \boldsymbol{\beta}_l^{\mathrm{p}} = \mathrm{sym} \sum_{l=1}^{N_{\mathrm{ss}}} \gamma_l \mathbf{S}_l . \tag{3.19}$$

In equation (3.19), N_{ss} is the number of slip systems and $\boldsymbol{\beta}_l^{\mathrm{p}}$ is the plastic distortion contributed by slip system l to the overall distortion.

3.3 Boundary Conditions

Various boundary conditions are adopted in dislocation dynamics and among them periodic boundary condition is employed here. This is justified by the fact that we will try to simulate the bulk crystal behaviour. Periodicity implies that the dislocations exiting from one side enter into the opposite side. To realize this, two quantities should be equal at the opposite sides: the dislocation density and the velocity. Dislocation density can be directly set to the same on the left and right, top and bottom, rear and front while solving kinetic equations. The periodicity of velocity field requires a periodic stress field within the bulk of the crystal. For this purpose, the total strain in equation (3.18) is decomposed

into the average strain $\bar{\boldsymbol{\varepsilon}}$, which is controlled by strain rate and independent of spatial points, and a perturbation strain $\tilde{\boldsymbol{\varepsilon}}$; that is

$$\boldsymbol{\varepsilon}^{\text{tot}} = \bar{\boldsymbol{\varepsilon}} + \tilde{\boldsymbol{\varepsilon}}. \tag{3.20}$$

Accordingly, the displacement field is also decomposed into two parts: a linear part $\bar{\mathbf{u}}$ whose (symmetric) gradient is $\bar{\boldsymbol{\varepsilon}}$ and a perturbation part $\tilde{\mathbf{u}}$ whose (symmetric) gradient is $\tilde{\boldsymbol{\varepsilon}}$. The former one is calculated in accordance with the imposed strain and represents the displacement due to the external loading mechanism; the latter gives $\tilde{\boldsymbol{\varepsilon}}$ in the form $\tilde{\boldsymbol{\varepsilon}} = \text{sym}(\nabla\tilde{\mathbf{u}})$. Following the above development, equation (3.18) can be rewritten in the following form:

$$\nabla \cdot [\mathbf{C} : (\text{sym}(\nabla\tilde{\mathbf{u}}) + \bar{\boldsymbol{\varepsilon}} - \text{sym}(\boldsymbol{\beta}^{p}))] = 0. \tag{3.21}$$

In the above equation, periodic boundary condition is applied on $\tilde{\mathbf{u}}$. Equation (3.21) is suited for any elastic boundary problem of plastically distorted bulk and the constraint on $\tilde{\mathbf{u}}$ ensures the equivalent stress and, in turn, dislocation velocity on opposite boundaries.

3.4 Numerical Treatments

The overall continuum dislocation dynamics model for mesoscale crystal plasticity consists of two sets of partial differential equations: equation (3.13) which governs dislocation density evolution and equation (3.21) which delivers stress field upon solving for the displacement field, separating the plastic strain and applying Hooke's law. We adopt a staggered numerical scheme for their coupled solution, which favours appropriate numerical treatments towards the equations according to their respective characteristics.

The treatments to equation (3.13) and (3.21) are first presented in this section with illustration of numerical examples. The overall numerical scheme is given in section 3.4.3 and the detailed discretization of space and time is presented in section 3.4.4.

3.4.1 Galerkin Finite Element Method for the Equilibrium Equation

The equilibrium equation (3.21) is rather conventional and can be solved using a standard Galerkin finite element method; see [176] and [180] , for example, for details of the implementation. During the simulation process, the stiffness matrix of the discretized system remains unchanged and only the load vector varies as the eigenstrain $\boldsymbol{\varepsilon}^{p}$ (representing the plastic distortion) changes as dislocations evolve. Therefore, only one LU decomposition step of the stiffness matrix is needed and reused at all steps throughout the simulation. Equation (3.12) represents the evolution of plastic slip and the two-step Adams-Bashforth method [181] is used in each time step to perform the update, which owns second-order accuracy.

Two examples are shown here by calculating self-stress field around an edge dislocation and a dislocation loop.

Suppose an edge dislocation is created by cutting half-through a perfect cubic crystal along the plane ABCD denoted in figure 3.1(a). The upper part is then stretched outward in the direction and by the amount of Burgers vector. Finally, the upper and lower parts are recombined along the line *B'C'* as seen in figure 3.1(b). In this way, an edge is formed on the surface of the crystal and an edge dislocation appears inside with the extra half plane below, see figure 3.1(b). Due to the break of the uniqueness of the

displacement field in the presence of dislocation, the original BC line is actually separated into two lines: *B'C'* and *B''C''*.

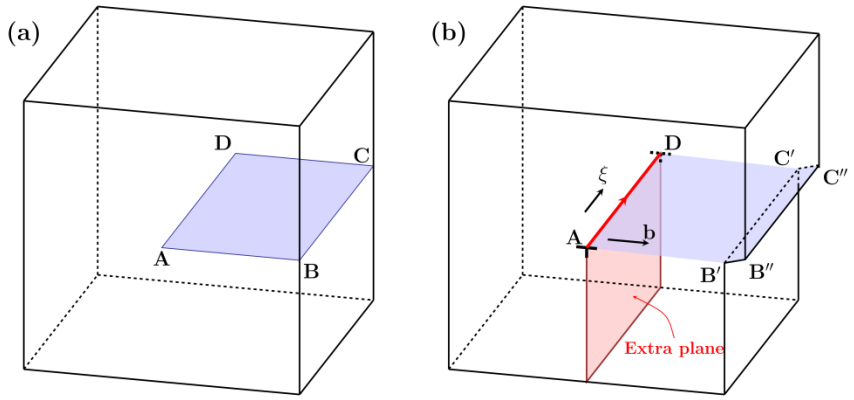

Figure 3.1. A perfect cubic crystal (a) is cut through ABCD to produce an edge dislocation (b) with line sense in the direction of AD.

The continuum method will represent such a case by the introduction of a prescribed plastic distortion field $\boldsymbol{\beta}^{p} = \gamma \vec{\mathbf{n}} \otimes \vec{\mathbf{b}}$ into a lamella around the plane *ABCD*. This simplified case is solved by equation (3.18) with the finite boundary condition that prevents rigid body motion. The numerically calculated stress component σ_{xz} is compared with analytical solution for an edge dislocation in figure 3.2. The linear elastic solutions of the stress components approaches infinity close to the dislocation core. The numerical solution given by equation (3.18) however has a finite value even at the exact position of dislocation. Apart from this difference, the fields in both cases show the similarity with each other.

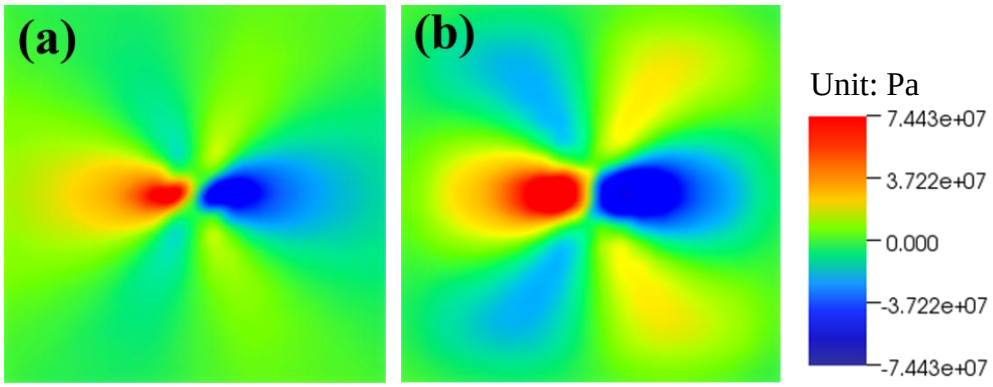

Figure 3.2. Comparison of stress component σ_{xz} around an edge dislocation between analytical solution (a) and numerical solution (b). Slight differences exit away from the core due to image fields present in case (a).

The stress field of a dislocation loop can also be computed by embedding into the cube an eigenstrain field which has the non-trivial value in a disk of a small thickness as shown in figure 3.3. Figure 3.4 shows the iso-surface of stress component σ_{xz} given by continuum solution and numerical solution respectively. The stress field is normalized by dividing by $\mu b / R$, where R is the radius of the dislocation loop. The similarity of the iso-surface between continuum representation and discrete computation illustrates the accuracy of the eigenstrain method in capturing the stress field which plays an essential role in the kinetics of dislocations.

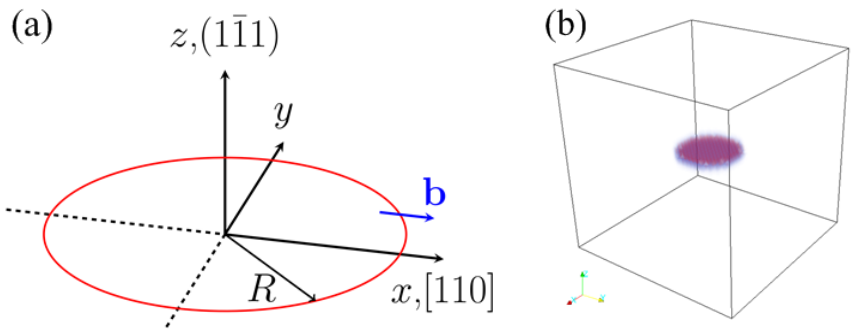

Figure 3.3. Stress field generated from a dislocation loop (a) is computed by embedding an eigenstrain field into the cube in (b). The non-vanishing area of the eigenstrain is of a disk shape that is bounded by the dislocation loop itself.

The success in solving kinetic equations to describe the motion of dislocations where the velocity or the underlying stress field is set as known and in solving the elastic boundary problem for the desired stress field while dislocation configuration is known lays down the foundation for the coupled scheme proposed in the following sections.

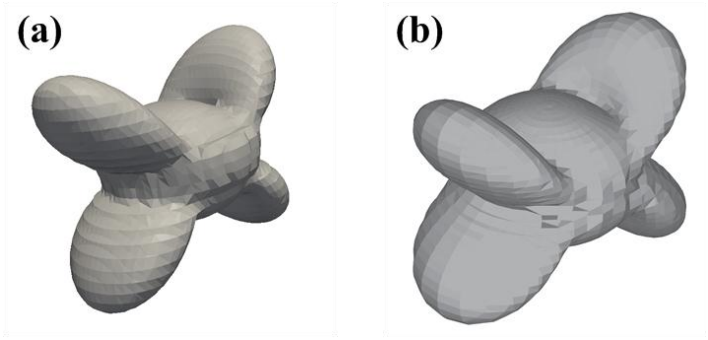

Figure 3.4. Iso-surface ($\sigma_{xz} = 0.08$) of a dislocation loop computed from continuum model by the usage of eigenstrain concept (a) and from discrete dislocation method (b) adopted from [182].

3.4.2 Least-square Finite Element Method for the Curl Equation

Equation (3.13) describes the evolution of dislocation density on a single slip plane. The dislocation lines must stay continuous on a pair of collinear slip systems, which, in FCC crystal, contain of pairs of slip planes, say, l and $l*$, sharing one Burgers vector. Thus the following divergence free condition applies to the dislocation density:

$$\nabla \cdot (\boldsymbol{\rho}_l + \boldsymbol{\rho}_{l*}) = 0. \tag{3.22}$$

The subscript l will be dropped for simplicity when no confusion arises.

To implement cross slip, the density on a given slip system is separated into two parts: $\delta\boldsymbol{\rho}^{\mathrm{cs}}$ corresponding to part that will cross slip and part that will continue to glide on the original plane, $\boldsymbol{\rho}^{\mathrm{g}} = \boldsymbol{\rho} - \delta\boldsymbol{\rho}^{\mathrm{cs}}$. Over a time step δt , the cross slip density is determined by the probability rate $\dot{p}_l^{\mathrm{cs}}$ described in equation (3.14):

$$\delta\boldsymbol{\rho}^{cs} = (\dot{p}_l^{cs}\delta t)\boldsymbol{\rho} = \delta p_l^{cs}\boldsymbol{\rho}, \tag{3.23}$$

Following the numerical scheme adopted in discrete dislocation simulation, cross slip happens only when the following conditions are all satisfied [183]: 1. The resolved shear stress computed from section 3.2 must be in favour of the cross slip; 2. A Monte Carlo method is used to determine whether a cross slip will take place; 3. We make an allowance for $\boldsymbol{\zeta}_l^{cs}$ to align with 15 °to the pure screw direction. A fraction $\delta\boldsymbol{\rho}^{cs}$ given by equation (3.23) cross slips given that all criteria of the process are satisfied. The corresponding velocities are associated with $\delta\boldsymbol{\rho}^{cs}$ and $\boldsymbol{\rho}^{g}$ for updating dislocation densities in the following way:

$$\begin{aligned} \dot{\boldsymbol{\rho}}^{g} &= \nabla\times(\mathbf{v}^{g}\times\boldsymbol{\rho}^{g}) \\ \delta\dot{\boldsymbol{\rho}}^{cs} &= \nabla\times(\mathbf{v}^{cs}\times\delta\boldsymbol{\rho}^{cs}) \end{aligned}, \tag{3.24}$$

where $\mathbf{v}^{g} = v^{g}\boldsymbol{\zeta}^{g}$ and $\mathbf{v}^{cs} = v^{cs}\boldsymbol{\zeta}^{cs}$ with $\boldsymbol{\zeta}^{g}$ and $\boldsymbol{\zeta}^{g}$ being the velocity directions in glide and cross-slip planes respectively.

The separation of the total density into gliding and cross slipping parts is also done in equation (3.12) and it has the final form as

$$\begin{aligned} \dot{\gamma}^{g}\mathbf{n}^{g}/b &= -\mathbf{v}^{g}\times\boldsymbol{\rho}^{g} \\ \dot{\gamma}^{cs}\mathbf{n}^{cs}/b &= -\mathbf{v}^{cs}\times\delta\boldsymbol{\rho}^{cs} \end{aligned}. \tag{3.25}$$

When solving equation (3.24), condition (3.22) is used as constraint on the solution of $\boldsymbol{\rho}$ to ensure continuity at all steps.

The dislocation kinetic equations (3.24) are hyperbolic partial differential equations describing the evolution of the dislocation density field through the transport and bow-out of dislocations. Numerical diffusion and dispersion are two issues associated with the discretization of hyperbolic PDEs. In addition, within a wide array of numerical methods, there exists a trade-off between the numerical oscillation caused by dispersion and the smearing of the peak caused by diffusion [184]. In the scheme adopted here, the dispersion is not a concern because the designation of velocity is controlled by the direction of dislocation density. Keeping this in mind, we choose the first order implicit discretization to handle the time derivatives, which proves to be almost dispersion-free as can be seen later. A least square finite element method (LSFEM) [185], which suits well for the first-order spatial differential operators [186], is then selected to solve the equation after time discretization. The entire scheme is presented as follows.

For convenience, a complete list of equations involved is as follows:

$$\begin{aligned} \dot{\boldsymbol{\rho}}^{\mathrm{g}} &= \nabla \times (\mathbf{v}^{\mathrm{g}} \times \boldsymbol{\rho}^{\mathrm{g}}) \\ \delta\dot{\boldsymbol{\rho}}^{\mathrm{cs}} &= \nabla \times (\mathbf{v}^{\mathrm{cs}} \times \delta\boldsymbol{\rho}^{\mathrm{cs}}), \\ 0 &= \nabla \cdot (\boldsymbol{\rho}^{\mathrm{g}} + \boldsymbol{\rho}^{\mathrm{cs}}) \end{aligned} \tag{3.26}$$

which is then rewritten in a matrix form:

$$A_t[\dot{\rho}] = A_0[\rho] + A_x \frac{\partial}{\partial x}[\rho] + A_y \frac{\partial}{\partial y}[\rho] + A_z \frac{\partial}{\partial z}[\rho]. \tag{3.27}$$

In equation (3.27), the unknown $[\rho]$ consists of both gliding dislocation density and cross slip density such that $[\rho]=[\rho_1^{\mathrm{g}},\rho_2^{\mathrm{g}},\rho_3^{\mathrm{g}},\delta\rho_1^{\mathrm{cs}},\delta\rho_2^{\mathrm{cs}},\delta\rho_3^{\mathrm{cs}}]^T$ and the coefficient matrix: A_t, A_0, A_x A_y and A_z are all of dimension 7×6. They are given by:

$$A_t=\begin{pmatrix} I_{3\times3} & 0 \\ 0 & I_{3\times3} \\ [0]_{1\times3} & [0]_{1\times3} \end{pmatrix}, A_0=\begin{pmatrix} A_0^{\mathrm{g}} & 0 \\ 0 & A_0^{\mathrm{cs}} \\ [0]_{1\times3} & [0]_{1\times3} \end{pmatrix}$$

$$A_x=\begin{pmatrix} A_x^{\mathrm{g}} & 0 \\ 0 & A_x^{\mathrm{cs}} \\ [1,0,0] & [1,0,0] \end{pmatrix}, A_y=\begin{pmatrix} A_y^{\mathrm{g}} & 0 \\ 0 & A_y^{\mathrm{cs}} \\ [0,1,0] & [0,1,0] \end{pmatrix}, A_z=\begin{pmatrix} A_z^{\mathrm{g}} & 0 \\ 0 & A_z^{\mathrm{cs}} \\ [0,0,1] & [0,0,1] \end{pmatrix},$$

where A_0^{g}, A_x^{g}, A_y^{g} and A_z^{g} are 3×3 matrices,

$$A_0^{\mathrm{g}}=\begin{pmatrix} -\partial_2 v_2^{\mathrm{g}}-\partial_3 v_3^{\mathrm{g}} & \partial_2 v_1^{\mathrm{g}} & \partial_3 v_1^{\mathrm{g}} \\ \partial_1 v_2^{g} & -\partial_1 v_1^{\mathrm{g}}-\partial_3 v_3^{\mathrm{g}} & \partial_3 v_2^{\mathrm{g}} \\ \partial_1 v_3^{g} & \partial_2 v_3^{\mathrm{g}} & -\partial_2 v_2^{\mathrm{g}}-\partial_1 v_1^{\mathrm{g}} \end{pmatrix}$$

$$A_x^{g}=\begin{pmatrix} 0 & 0 & 0 \\ v_2^{\mathrm{g}} & -v_1^{\mathrm{g}} & 0 \\ v_3^{\mathrm{g}} & 0 & -v_1^{\mathrm{g}} \end{pmatrix}, A_y^{g}=\begin{pmatrix} -v_2^{\mathrm{g}} & v_1^{\mathrm{g}} & 0 \\ 0 & 0 & 0 \\ 0 & v_3^{\mathrm{g}} & -v_2^{\mathrm{g}} \end{pmatrix}, A_z^{\mathrm{g}}=\begin{pmatrix} -v_3^{\mathrm{g}} & 0 & v_1^{\mathrm{g}} \\ 0 & -v_3^{\mathrm{g}} & v_2^{\mathrm{g}} \\ 0 & 0 & 0 \end{pmatrix},$$

and the matrices A_0^{cs}, A_x^{cs}, A_y^{cs} and A_z^{cs} have the same expressions with replacing the superscript g with cs. After the temporal discretization by using first-order implicit method, equation (3.27) reads:

$$L^n([\rho]^{n+1})=P^n, \tag{3.28}$$

where the differential operator $L^n([\cdot])$ and P^n depend on the information at time $n\Delta t$ as follows:

$$L^n([\cdot]) = [-A_t + \Delta t A_0 + \Delta t(A_x \frac{\partial}{\partial x} + A_y \frac{\partial}{\partial y} + A_z \frac{\partial}{\partial z})]_{7\times 6}[\cdot]$$
$$P^n = [-A_t]_{7\times 6}[\rho]^n \quad (3.29)$$

LSFEM works by minimizing the least-square residual, R which is expressed as a functional,

$$R = \int_\Omega \left(L^n([\rho]^{n+1}) - P^n \right)^2 d\Omega, \quad (3.30)$$

where Ω is the spatial domain of the problem. The minimization follows from setting the variation of R to be zero, namely

$$\delta R = 2\int_\Omega \left(L^n([\rho]^{n+1}) - P^n \right) L^n([\delta\rho]^{n+1}) d\Omega = 0, \quad (3.31)$$

where $[\delta\rho]$ is variation of $[\rho]$. The above equation leads to the weak form of equation (3.28):

$$\left\langle L^n([\delta\rho]), L^n([\rho]) \right\rangle_\Omega = \left\langle L^n([\delta\rho]), P^n \right\rangle_\Omega, \quad (3.32)$$

with the inner products defined by:

$$\langle f, g \rangle_\Omega = \int_\Omega fg d\Omega. \quad (3.33)$$

It is worth noting that the weak form given by Galerkin FEM for the same problem has the form: $\left\langle [\delta\rho], L^n([\rho]) \right\rangle_\Omega = \left\langle [\delta\rho], P^n \right\rangle_\Omega$, where the differential operator $L^n([\cdot])$ only applies to $[\rho]$, as opposed to the case of least square FEM. The Galerkin FEM suffers

spurious oscillation in the case of first order systems [186] and cannot accommodate the extra divergence free condition directly.

By discritizing $[\rho]$ and $[\delta\rho]$ piecewise in the space, equation (3.32) eventually leads to the desired set of linear algebraic equations:

$$K^n U^{n+1} = R^n, \tag{3.34}$$

in which both stiffness matrix K^n and the load vector R^n are evaluated based on the information at time step n.

Several examples are presented here for illustrating the solution given by above-mentioned Backward-Euler/LSFEM for the curl equations. Starting from a simple example, a dislocation loop is put in a square domain where a velocity field is applied in radial direction such that the loop expands. Figure 3.5 shows the initial condition and the expanded loop, plotted in terms of the magnitude of vector $\boldsymbol{\rho}$, by solving the governing equation (3.10).It is noted here that the value of $\|\boldsymbol{\rho}\|$ itself is not of great importance because the examples of this section serve merely as numerical examination and the parameters used are not physics. As expected, the numerical diffusion is inevitable from first-order backward Euler discretization while the oscillation is very little if at all existent. The employed curl equation furnishes the loop with perfect continuity after expansion.

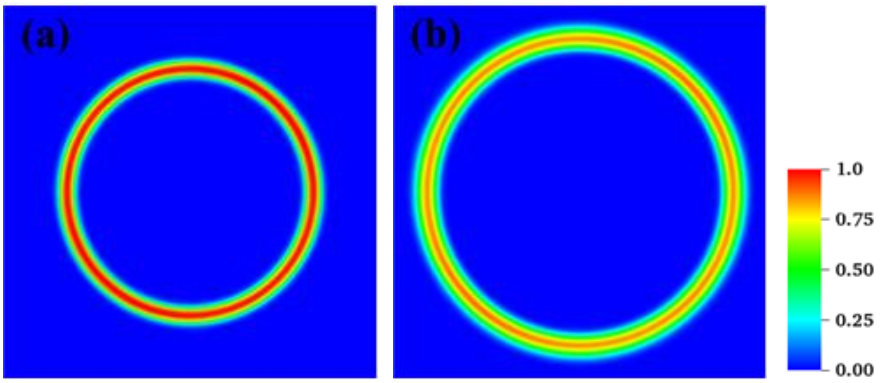

Figure 3.5. Expansion of a dislocation loop: (a) initial and (b) final configurations. The colour scales in both (a) and (b) are the same, implying the occurrence of some numerical diffusion. Nonetheless, there is no numerical oscillation and the continuity of the loop is preserved.

One might expect the change of the shape of the dislocation loop if the velocity field is arranged appropriately. In figure 3.6 the velocity is associated with dislocation density vector in a perpendicular way and its magnitude gradually decreases to zero near the boundary. As a result, the dislocations pile up at the vicinity of the boundary and transforms to square shape. Similar results can be found in reference [187] with the difference that the dislocation is represented by second order tensor rather than vector.

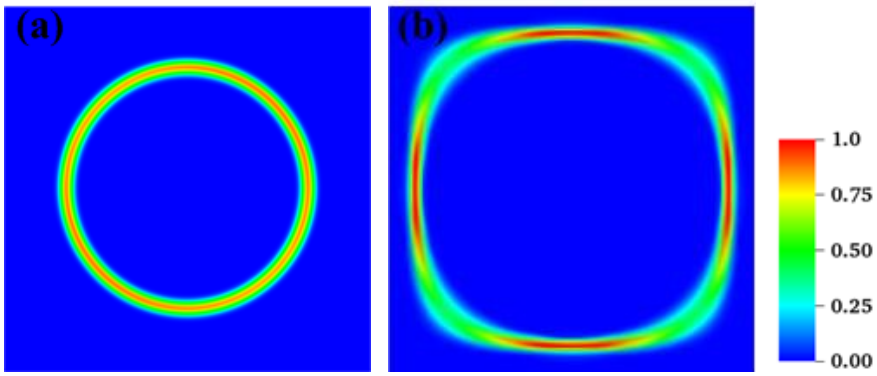

Figure 3.6. An initially circular dislocation loop (a) transforms into square one (b) by expansion and manipulation of the velocity field.

The vector description used here leads to an easier manipulation of dislocation bundles through the desired velocity distribution. Equation (3.24) which accounts for cross slip is implemented in 3D domain where a dislocation loop is located in a prescribed velocity field that directs dislocations to expand and cross slip to a collinear plane, as shown in figure 3.7. In this example, all screw dislocations in the bundle are allowed to cross slip by setting $\delta p^{cs} = 1$. It is to be noted here that in order to preserve the connection of dislocation bundles, the divergence free condition (3.22) applies to the whole set of collinear slip systems.

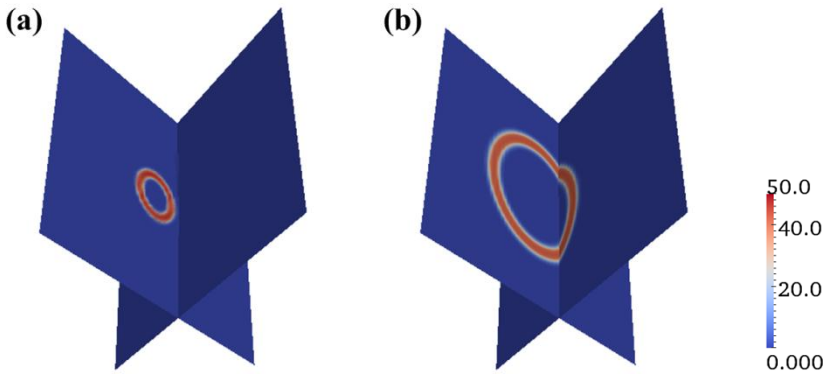

Figure 3.7. Cross-slip simulation: a bundle of dislocation loops glides and cross-slips to a collinear slip plane. In this case, the probability δp^{cs} is set equal to unity.

When δp^{cs} is less than unity, only a fraction of screw bundle of dislocations will cross slip and the remaining fraction continues on the original plane. Such a case is illustrated in figure 3.8, where three snapshots are presented during the process that the screw dislocations cross slip twice between collinear slip systems. The fractions of cross slip are prescribed arbitrarily in this example by setting $\delta p^{cs} = 0.79$ for the first event and $\delta p^{cs} = 0.52$ for the second. The divergence free condition is also applied to the total density $\boldsymbol{\rho}$.

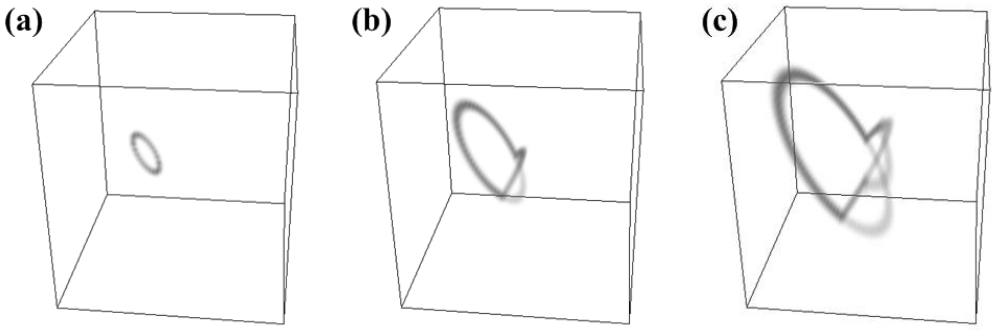

Figure 3.8. A dislocation loop cross-slips twice between a set of collinear slip systems: (a) is the initial prescribed loop, (b) is the configuration after the first cross-slip, and (c) is the final configuration where the original one bundle converts into three bundles on different slip planes belonging to two slip systems.

The above examples demonstrate the accurate capture of dislocation bundle behaviour by the kinetic equations when the velocity field and δp^{cs} are prescribed. As discussed in section 3.2, the stress field within the crystal generates the velocity field and it is also involved in the determination of δp^{cs}. Sample solution of stress field is presented in the following section for prescribed dislocation configuration before the kinetics and equilibrium solutions are coupled to solve the plasticity problem.

3.4.3 The Coupled Numerical Scheme for Simulation

As presented above, the overall numerical implementation of continuum dislocation dynamics consists of two parts, the kinetic equations for the dislocation density evolution (3.24) and the plastic distortion field (3.25), and the stress equilibrium equation (3.17). Once the velocity field in equation (3.24) and equation (3.25) is determined, $\boldsymbol{\rho}$ and γ

fields can be updated with ease; once the plastic (eigenstrain) field is prescribed in equation (3.18) the stress field and subsequently the velocity field is determined. The overall problem is treated with a staggered scheme described as follows. The initial plastic distortion $\boldsymbol{\beta}^{\mathrm{P}}$ is prescribed for each slip system and the associated dislocation density vector is calculated by using equation (3.1) and (3.6). The plastic distortion is the eigenstrain used in equation (3.18) to solve the stress field which yields velocity field for the next time step through equation (3.15). The overall scheme is repeated until a stop criterion $\bar{\boldsymbol{\varepsilon}} = \boldsymbol{\varepsilon}^{*}$ is reached, as shown in figure 3.9.

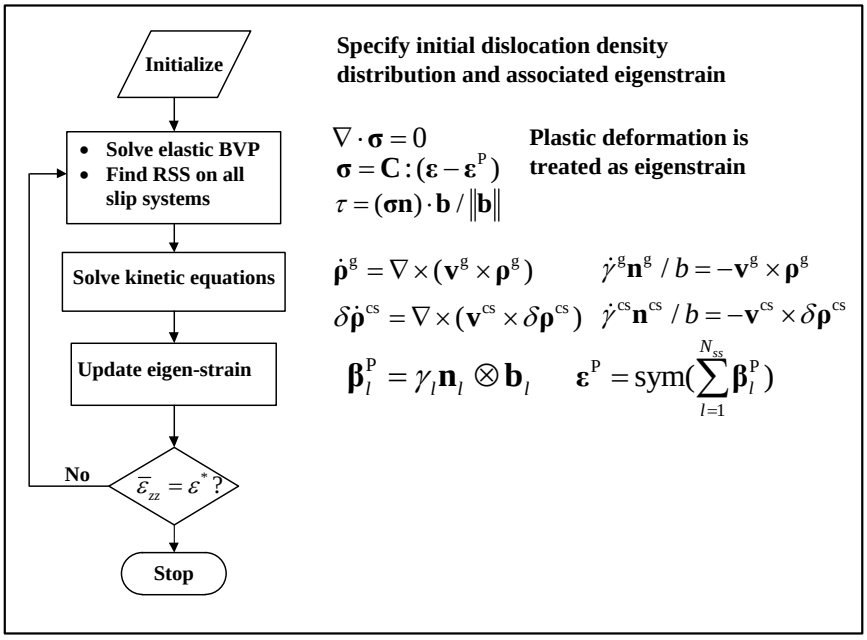

Figure 3.9. A flowchart of the computational algorithm. The stress equilibrium equation is coupled with dislocation kinetics through a staggered scheme.

3.4.4 Discretization in Spatial and Temporal Dimensions

A distinctive feature of dislocation motion is that they always glide on crystallographic planes. In order to capture the planar motion accurately, the mesh should be constructed in such a way that the density field is interpolated using only the nodal values of the field on the same plane. In this manner, the interpolation of the local density field over the elements should decouple density values on different parallel slip planes. This can be made possible by a mesh with nodes and their connections that form a superlattice of the crystallographic structure of the crystal under consideration. Keeping this in mind, the 3D space of the crystal can be filled with octahedral and tetrahedral elements. At this point, octahedral elements are split to two pyramids sharing the base. Thus two types of elements are used, and the detailed process of filling the 3D space with these elements is shown in figure 3.10.

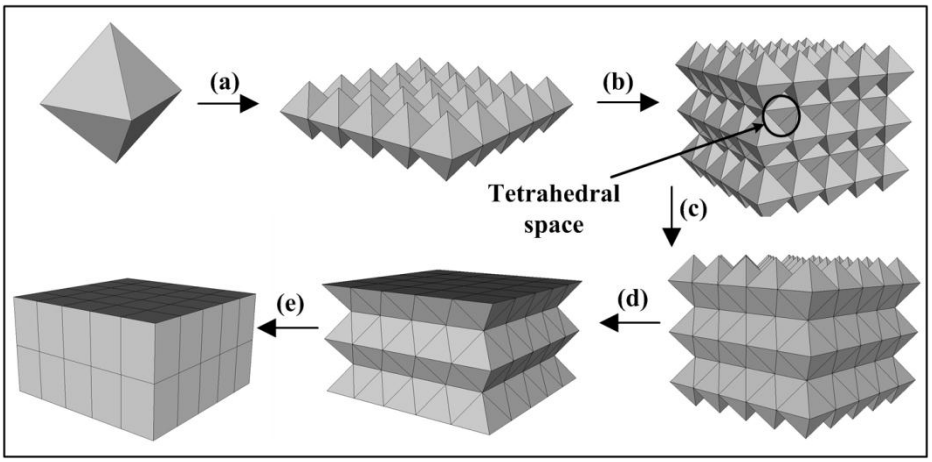

Figure 3.10. Construction of a superlattice mesh in FCC crystals: (a) arranging octahedrons on (001) planes, (b) stacking layers of octahedrons to fill 3D space, (c) filling up the voids with tetrahedral elements, (d) crop the extra pyramid elements at top and bottom layers, and (e) filling the boundaries to make them flat. It has been found more convenient to select the *x*, *y* and *z* coordinates along the [110], $[\bar{1}10]$ and [001] directions, respectively.

In figure 3.10 and also in the following simulations, the *x*, *y*, and *z* axis are aligned with [110], $[\bar{1}10]$, and [001] directions, respectively, for convenience. Viewing from the outside, the surface of the bulk seems to be meshed regularly with hexahedral elements but the crystal structure is represented inside as can be seen from figure 3.11 which shows the triangular mesh on slip planes.

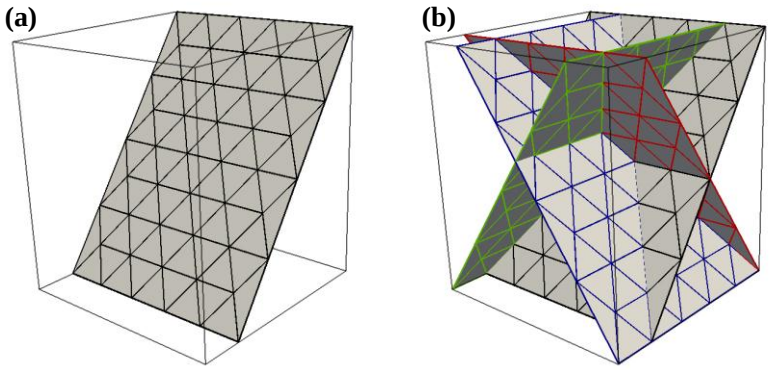

Figure 3.11. Triangular mesh on {111} slip planes of an FCC lattice. All primary slip occurs on the {111} type planes in FCC crystals. The *x*, *y* and *z* coordinates are along the [110], $[\bar{1}10]$ and [001] directions, respectively.

What is shown in figure 3.11 is merely the structure of the mesh. As of the spatial resolution, the size of one element should also be adjusted according to the physics of dislocations. The vector field **ρ** used in the model represents a bundle of dislocations of the same Burgers vector, slip plane and orientation, meaning that there is only one value at a spatial node. Suppose that the mesh is fine enough to the extent that the size of element is on the order of Burgers vector, all of the detailed knowledge of dislocations within the crystal can be represented accurately. However, such a fine mesh is neither computationally practical nor necessary because dislocations with opposite Burgers vector and close to each other will naturally annihilate themselves. Out of this consideration, the element size is chosen on the order of the annihilation distance of dislocations of opposite signs so that the vector representation of the density is consistent with physical situations in which the annihilation has readily occurred. The dependence of annihilation distance on the property of dislocations is reported in references [106,188] , in which the distance is measured at 1.6 nm for edge dislocations and 50 nm ~

500 nm for screw dislocations. Based on this knowledge, the distance between parallel {111} planes in the model is set to be around 20 nm, which is tiny in comparison with the domain dimension, ~ 5 μm.

The temporal discretization is realized on the basis of a balance between stability, accuracy and efficiency. In our case, stability is not a concern because the implicit Euler method is adopted here, which is unconditionally stable. For efficiency and accuracy, the time step is chosen adaptively so that in each time step the fastest moving dislocation lines cannot move over the size of an element. Here, the adaptive time step varies around 6 ns which is about 10 times or more that used in discrete simulation [107].

CHAPTER 4. TIME COARSE GRAINING OF CROSS SLIP RATE

In discrete dislocation simulation, the probability of cross-slip event is calculated by using the information of a segment and crystal parameters [122,189–191]. It is given in the following form:

$$P(L,\Delta t) = A\frac{L}{L_0}\frac{\Delta t}{\Delta t_0}\exp\left(\frac{-W}{k_{\mathrm{B}}T}\right), \tag{4.1}$$

where L_0 and Δt_0 are reference length and time, L and Δt the length of the segment and time step, W the activation energy, k_{B} and T are Boltzmann constant and absolute temperature respectively, and A is a scaling factor. The activation energy is written as

$$W = V\left(\left|\tau_{\mathrm{int}}^{(\mathrm{g})}\right| - \tau_{III}\right), \text{ and}$$

$$W = V\left(\left|\tau_{\mathrm{eff}}^{(\mathrm{cs})}\right| - \tau_{III}\right),$$

for immobilized and mobilized dislocations respectively. The resolved shear stress τ_{III} is the thermally activated critical stress for the onset of stage III in the stress-strain curves of fcc crystals [104], which is 30 MPa for copper. V is activation volume which is around $500\mathrm{b}^3$ for copper singe crystal, depending on the resolved shear stress [192]. But such a method is not available for continuum model where the information of the length of segment is in lack. An alternative way to avoid this problem is to implement a

corresponding discrete dislocation simulation first and incorporate the data into the continuum model.

This chapter presents the method to incorporate discrete dislocation data of cross slip rate into the continuum dislocation dynamics model, which is achieved by applying time series analysis and a coarse-graining process to the cross slip data from discrete dislocation dynamics simulations. The desired form of continuum cross-slip rate is presented first, followed by a definition of cross-slip rate in discrete simulation. Next, the time series analysis is presented followed by the results.

4.1 Cross-slip Rate in Continuum Dislocation Dynamics

The cross slip probability rate $\dot{p}_l^{\mathrm{cs}}$ used in chapter 3 is required in order to solve the dislocation transport equations. A previous work [155] makes an attempt to define the cross-slip rate as a coarse grained parameter of the corresponding discrete dislocation dynamics rate. The procedure will be followed here with some modifications. Without loss of generality, the cross-slip probability rate $\dot{p}_l^{\mathrm{cs}}$ in the continuum model is regarded as a function of time and space:

$$\dot{p}_l^{\mathrm{cs}}(\mathbf{x},t) = \bar{\dot{p}}_l^{\mathrm{cs}}(t) + \dot{\xi}_l^{\mathrm{cs}}(\mathbf{x},t)\,, \tag{4.2}$$

where $\bar{\dot{p}}_l^{\mathrm{cs}}(t)$ is the smooth function of time, $\dot{\xi}_l^{\mathrm{cs}}(\mathbf{x},t)$ is a fluctuation term which depends both on time and space. Equation (4.2) is valid under the assumption that the temporally oscillated cross-slip rate in discrete dislocation simulation can be represented by a coarse-grained ensemble average and a spatial fluctuation term in the continuum model. This

assumption is justified in the following sections by applying coarse-graining process on the discrete data.

So the goal set by continuum model for the corresponding discrete simulation is to find the function $\dot{\bar{p}}_l^{\mathrm{cs}}(t)$ from discrete data and also the probability density function from which the fluctuation term $\dot{\xi}_l^{\mathrm{cs}}(\mathbf{x},t)$ is sampled.

4.2 Cross-slip in Discrete Dislocation Dynamics

The cross-slip rate in discrete dislocation simulation is given by [155]:

$$\dot{R}_{\mathrm{cs}}^{l,n} = \frac{\left\langle \Delta\rho_{l,n}^{\mathrm{cs}} \right\rangle}{\left\langle \rho_{l,n}^{\mathrm{cs}}(\zeta_l^{\mathrm{cs}}) \right\rangle \Delta t}, \tag{4.3}$$

where l is the slip system number, Δt time step in discrete simulation, n the time step number, $\langle\cdot\rangle$ denotes the ensemble average, $\left\langle \Delta\rho_{l,n}^{\mathrm{cs}} \right\rangle$ represents the density of dislocations that cross-slipped from system l to its cross-slip system during Δt time, $\left\langle \rho_{l,n}^{\mathrm{cs}}(\zeta_l^{\mathrm{cs}}) \right\rangle$ represents the total screw density on slip system l.

Because the discrete dislocation model treats cross-slip as random events in time and space, the discrete cross-slip rate computed from equation (4.3) cannot be directly employed in the continuum model which is based on the mesoscale modelling at a larger time scale. It is also incorrect to smooth the cross-slip rate in a casual way because the averaging process should take into account the physics of dislocations rather than just data. The earlier works [72,153] lay foundations for bridging such a gap by applying the statistics to the system of dislocations, acquiring the dislocation kinetic equations in

continuum form. This series of works essentially solves the scaling issue in space. The following works [107,154,155] implement 3D dislocation simulation to find the parameters used in dislocation kinetic equations. Under the assumption of statistical homogeneity of bulk plasticity, the work reported in [155] performs volumetric average over discrete dislocation dynamics data and argues that the temporal gap can be solved by a coarse-graining process which is based on the theory of time series analysis [193,194].

4.3 Time Series Analysis

In statistics, an array of the observations towards a random variable can be arranged chronologically to form a time series: $\{x_t, t \in T\}$, where the observed value x_t is drawn from a random variable X_t at time t. The purpose of time series analysis is to reveal the characteristic of random series $\{X_t, t \in T\}$ through the historically observed values x_t and even forecast the values in the future [194]. Time series can be generally divided into two types: stationary and non-stationary. The stationary series are relatively simple and also sufficiently studied during the past years, which is characterized by a constant mean value, an invariant variance, and the immunity of any seasonal change [193]. That is, the random variable X_t is independent of time t for a stationary time series and thus the observed series x_t can be viewed as a sample of a random variable X.

Non-stationary time series differ from the stationary ones in the way that the features of random variables X_t such as mean average, standard variance, etc. change over the time. One way to study a non-stationary time series is to transform it into a stationary one. For example, the difference operator is demonstrated to be effective in

removing the change in the mean value—or in another word, the trend—of X_t. The first order difference operator $\nabla(\cdot)$ is defined by [193]:

$$\nabla X_t = X_t - X_{t-1}, \tag{4.4}$$

which gives a new series $\{\nabla X_t, t \in T\}$. The *k*-th order difference of X_t is obtained by applying the operator to $\nabla^{k-1} X_t$ and is denoted by $\nabla^k X_t$. It has been illustrated that $k = 2$ is enough to remove the trend [155] in cross-slip rate. In some cases, the change in variance of X_t can be removed by taking the logarithmic value of the original observations.

In the case that a time series fails to be stationarized by any transformation, it may still be segmented into piecewise stationary series [195]:

$$\begin{matrix} \left\{\{X_{t_1}, t_1 \in T_1\}, \{X_{t_2}, t_2 \in T_2\}, ..., \{X_{t_n}, t_n \in T_n\}\right\} \\ T_1 \cup T_2 \cup ... \cup T_n = T \end{matrix}, \tag{4.5}$$

where each subset $\{X_{t_i}, t_i \in T_i\}$, $i = 1, 2, ..., n$ is stationary and all analytical methods for stationary series can thus be applied for it. It is important to keep in mind that each segment has individual stochastic quantities such as mean value, variance, etc., which might differ from segment to segment.

It is of interest to define the correlation time for a stationary series in order to perform the coarse-graining process as seen later. Suppose that the random variable is found to be stationary from t_1 to t_2 of a time series, the correlation time within this segment is defined by:

$$T_c = \int_0^{\infty} c(\tau)d\tau \approx \int_0^{t_2-t_1} c(\tau)d\tau \,, \tag{4.6}$$

where $c(\tau)$ is the correlation function given by:

$$c(\tau) = \frac{E((X_t - \mu)(X_{t+\tau} - \mu))}{\sigma} \,, \tag{4.7}$$

where μ and σ are mean value and variance of the stationary segment, respectively, and the numerator is the covariance and $E(\cdot)$ denotes the expected value.

The coarse-graining process is presented in the next section based on the data obtained according to equation (4.3) and the equations from (4.4) to (4.7).

4.4 Coarse-graining of the Discrete Cross-slip Rate

In order to bridge the scaling gap in space and time between discrete and continuum simulations, coarse graining is required. Here, the spatial scaling issue has been taken care of by the ensemble average in equation (4.3); the time scale issue is handled with coarse-graining process based on time series analysis shown in 4.3.

The first step to perform coarse-graining is to collect the data from discrete dislocation simulation. To this end, a copper single crystal of a cubic shape with a 5 μm edge is subjected to a monotonic loading controlled by an applied rate of strain of 30/s along the [001] crystallographic direction. The crystal is filled with dislocation network of density of 1×10^{12} m^{-2} after relaxation. The dislocation dynamics code microMegas [104] is used.

Equation (4.3) is used for obtaining cross-slip rates on all of 12 slip systems, $l = 1, 2, 3, \ldots, 12$. The slip systems are indexed in table 4.1 for convenience. The original time series $\dot{R}_{\mathrm{cs}}^{l,n}$ are plotted in figure 4.1, where all slip systems exhibit oscillatory behaviour in $\dot{R}_{\mathrm{cs}}^{l,n}$. But for active slip systems, on which Schmid factors are non-trivial according to table 4.1, larger oscillation generally takes place during early stage of the loading process. For inactive slip systems, $l = 5, 6, 7, 8$ in the simulation, the oscillation keeps being serious and the overall trend seems to remain at a trivial level. The difference arises from the difference of externally resolved shear stress on active and inactive slip systems. For active slip systems, the external shear stress is smaller in comparison with the internal stress field at earlier stage of the simulation but becomes larger until to be dominant at larger strain. Thus the main driving force for cross-slip events on active slip systems are transiting from the internal stress field, which is more of randomness, to external loading, which is uniformly distributed and stably increased within the cube. The external loading, on the other hand, fails to influence the inactive slip system due to a trivial Schmid factor, which causes the more oscillatory and almost none trending cross-slip events on them. It is also noted that the time series for a pair of collinear slip systems seem to be correlated but not exactly the same in spite of their symmetry regarding the tensile axis. The difference in initial dislocation configurations between a pair of collinear slip systems must have an influence on the subsequent occurrence of cross-slip events.

Table 4.1. Slip system in FCC crystals

Slip system index	Slip plane	Slip direction	Schmidt factor for [001] loading
1	(111)	$[\bar{1}01]$	0.41
2	$(1\bar{1}1)$	$[\bar{1}01]$	0.41
3	$(1\bar{1}1)$	$[011]$	0.41
4	$(11\bar{1})$	$[011]$	-0.41
5	$(11\bar{1})$	$[\bar{1}10]$	0.0
6	(111)	$[\bar{1}10]$	0.0
7	$(\bar{1}11)$	$[110]$	0.0
8	$(1\bar{1}1)$	$[110]$	0.0
9	(111)	$[01\bar{1}]$	-0.41
10	$(\bar{1}11)$	$[01\bar{1}]$	-0.41
11	$(11\bar{1})$	$[101]$	-0.41
12	$(\bar{1}11)$	$[101]$	0.41

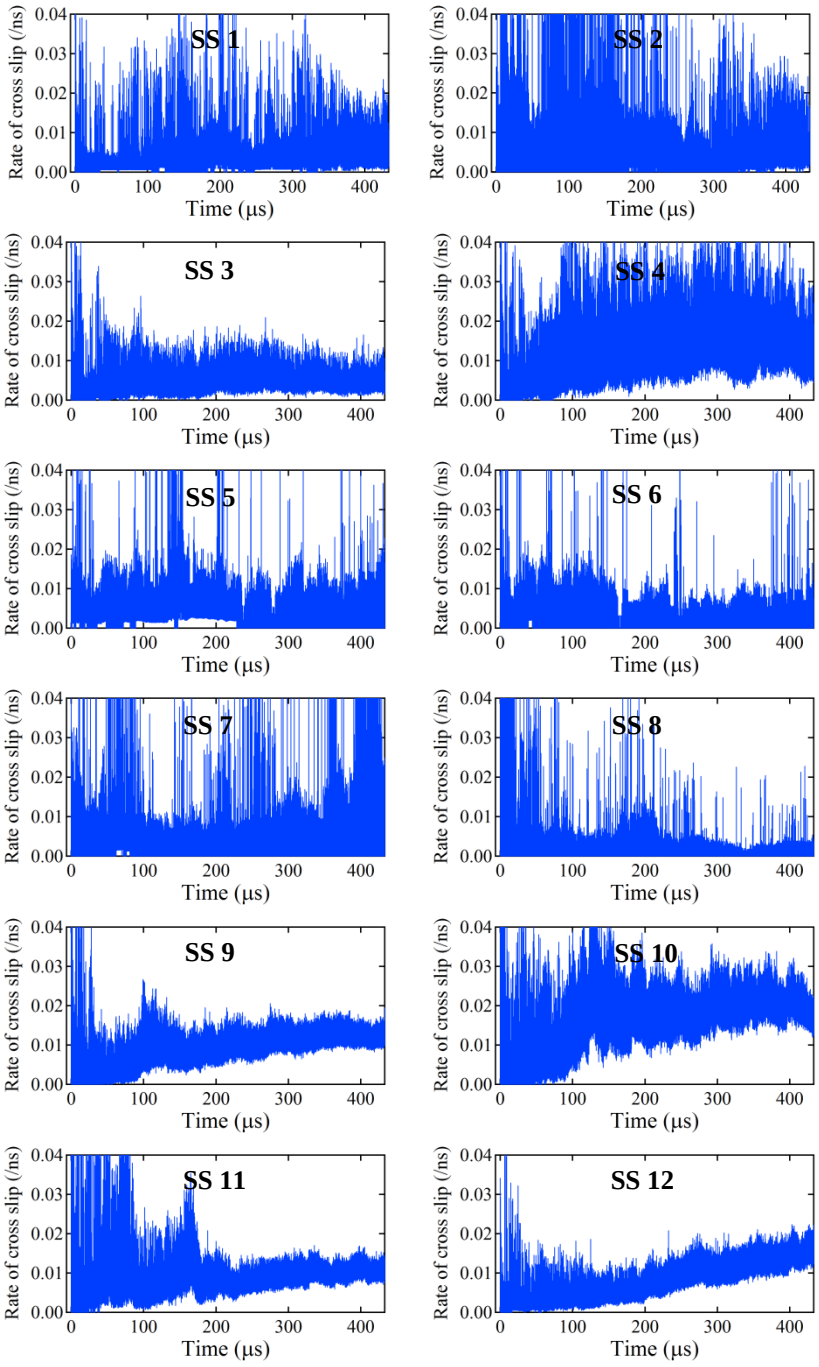

Figure 4.1. The original time series of cross-slip rates of all 12 slip systems (SS stands for slip system). Slip systems 1, 2, 3, 4, 9, 10, 11, and 12 are active slip systems which exhibit increasing trend and decreasing oscillation. The inactive ones show no obvious trend and the oscillations remain to be serious.

The application of equation (4.4) to the cross-slip time series $\dot{R}_{cs}^{l,n}$ creates a new time series by removing the trend from the original one. New series are referred to as difference series and denoted by $\nabla\dot{R}_{cs}^{l}$ for slip system l . Figure 4.2 shows all twelve difference series.

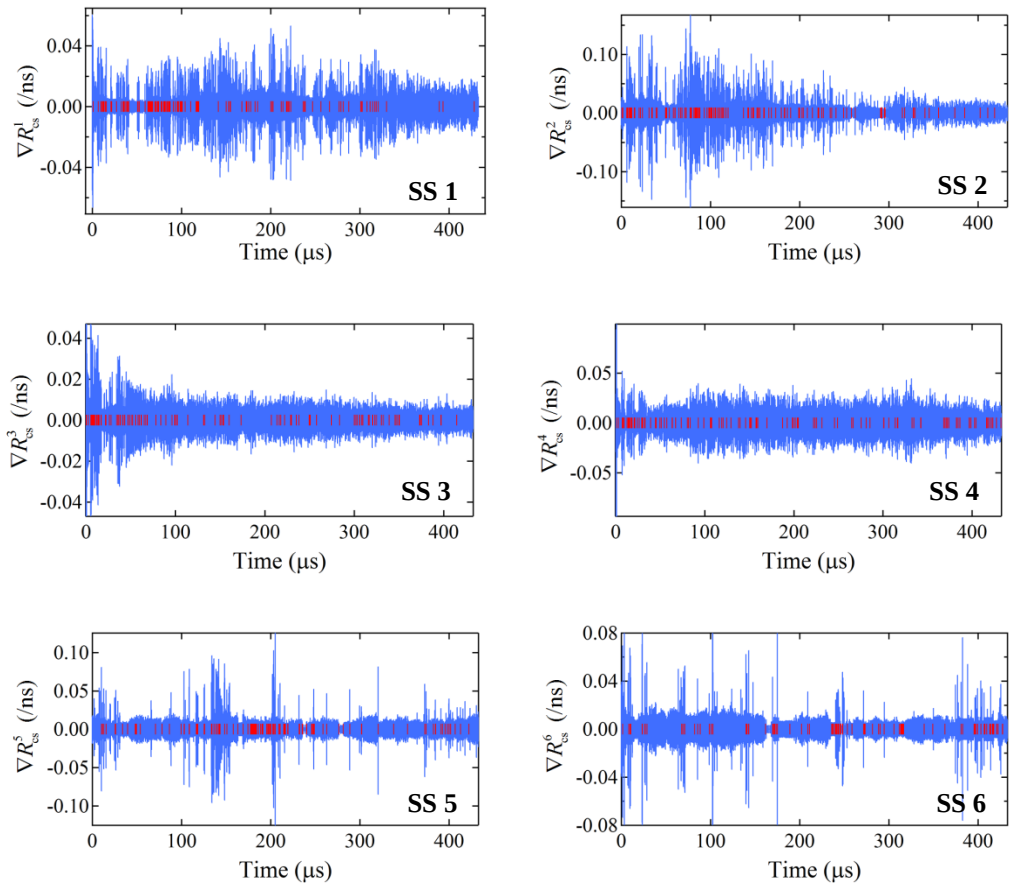

Figure 4.2. The difference series of cross-slip rates for all slip systems and the boundaries of stationary segments (red vertical lines). It can be seen from these figures that the variances of the series tend to decline with time, but the overall trend is removed by the difference operation.

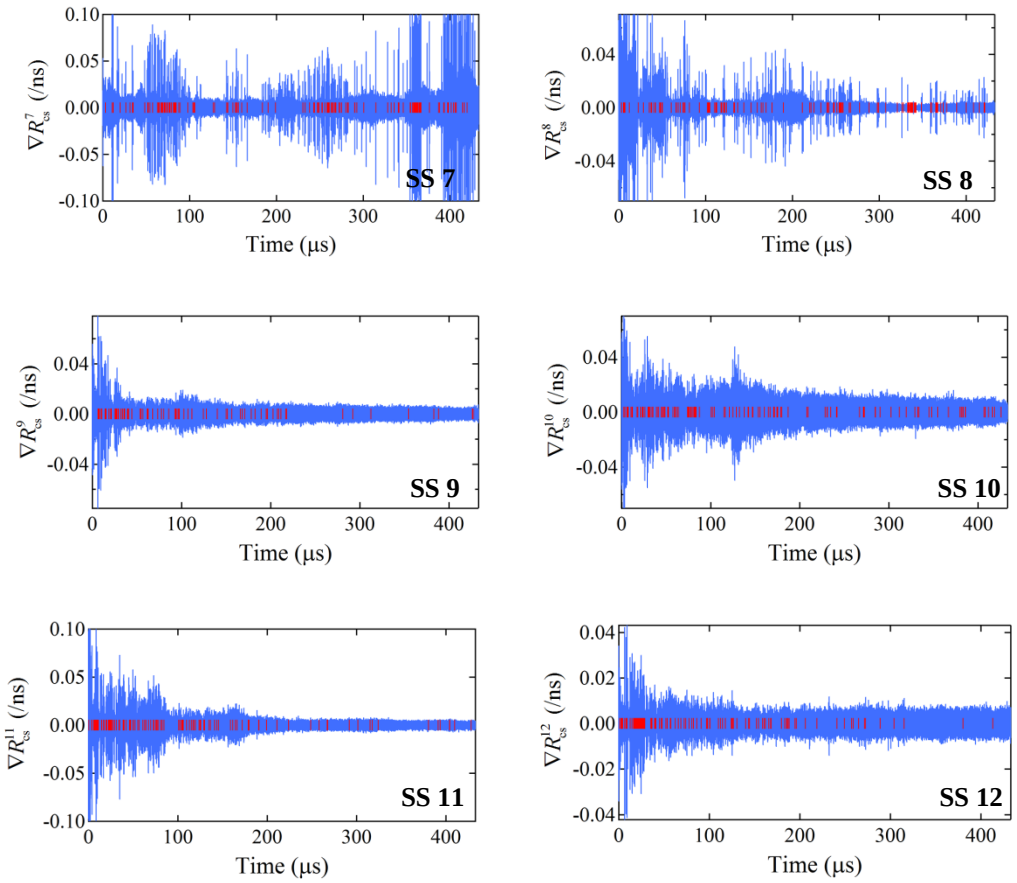

Figure 4.2. (continued) The difference series of cross-slip rates for all slip systems and the boundaries of stationary segments (red vertical lines). It can be seen from these figures that the variances of the series tend to decline with time, but the overall trend is removed by the difference operation.

The trends associated with all original cross-slip rates are removed by the first order differencing scheme and the series seem to be symmetric about the time axis. The symmetry of $\nabla\dot{R}_{cs}^{l}$ arises from the wavy behaviour of $\dot{R}_{cs}^{l}$ during consecutive time steps, $\dot{R}_{cs}^{l}$ upsurges to a higher value and then drops to the value close to the one before the rise. It is also seen that the variances of difference series are changing through the simulation, which makes the overall series non-stationary and such volatility cannot be simply

removed by taking differences, neither by taking logarithm. Further inspection shows that the series $\nabla\dot{R}^{l}_{\mathrm{cs}}$ can be segmented into piecewise stationary sub-series. This task is fulfilled with Brandt's Generalized Likelihood Ratio method (GLR) [196], which detects the series segment boundaries by measuring the dissimilarity between two sliding windows within which the series are modelled auto-regressively [195]. Figure 4.2 marks boundaries of stationary series in vertical red lines such that $\nabla\dot{R}^{l}_{\mathrm{cs}}$ is approximately stationary between two neighbouring red lines. In general, the number of segments is bigger on inactive slip systems than on active slip systems and bigger during earlier stages than during later stages within active slip systems. This is due to the above-discussed reason that cross-slip events are mainly dominated by the internal stress field for inactive slip systems and for active slip systems but at earlier stages. As simulation goes on, the stably increasing applied resolved shear stress are becoming dominant on active slip systems and thus makes the series there more stable in their oscillations and thus less number of segments is needed. On the contrary, for inactive slip systems, however, the cross-slip rates are generally much less predictable and change vividly in oscillation (see SS 7 for example).

One of the quantitative ways to represent the tendency of $\nabla\dot{R}^{l}_{\mathrm{cs}}$ series towards stationarity is to calculate the correlation time within each segment. Two cross-slip events that fall within the correlation time are considered to be correlated and those separating longer than this time scale are thought as independent. The longer the correlation time, the more connection exists between events. Due to this reason, the correlation time can also be treated as the coarse-graining time which serves as a

temporal window span within which an average process is applied to discrete cross-slip rates $\dot{R}_{\mathrm{cs}}^{l}$ to yield the data for later usage in the continuum model [155].

Equation (4.6) is applied to $\nabla\dot{R}_{\mathrm{cs}}^{l}$ piecewise for all slip systems and the correlation times are shown in figure 4.3. Despite oscillation, the correlation time does increase with simulation time on active slip systems but remains to be trivial on inactive slip systems. The final correlation time on active slip systems is around or close to 0.05 μs, which is on the same order of magnitude with previous results [155].

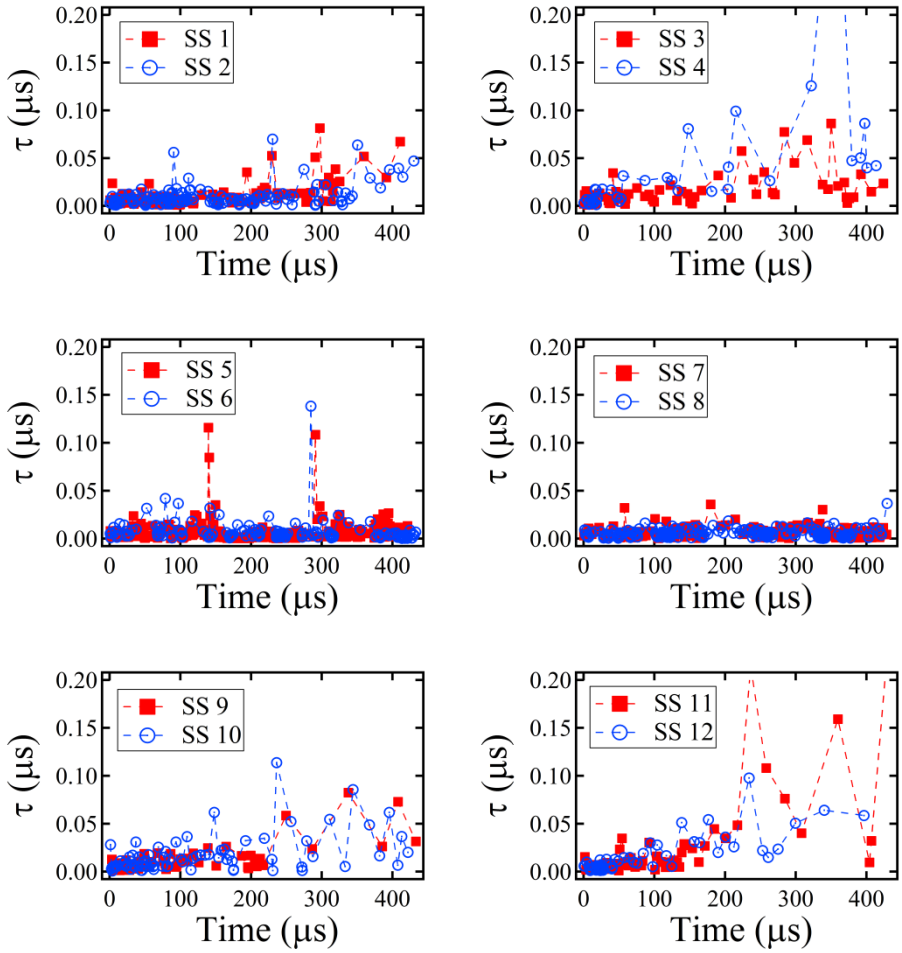

Figure 4.3. Correlation time of time series of cross-slip rates for all slip systems. The recorded points correspond to the middle times of sub-series which is stationary.

The correlation time for a stationary sub-series is used as the coarse-graining time over which the average value of $\nabla \dot{R}_{cs}^{l}$ is taken as:

$$\dot{R}_{cg}^{l}(t) = \int_{t_1}^{t_2} \dot{R}_{cs}^{l}(t')w(t-t')dt', \tag{4.8}$$

where $\dot{R}^l_{\mathrm{cg}}(t)$ is the coarse-grained cross-slip rate at time t and for slip system l, t_1 and t_2 the starting and end point of the stationary series, respectively, $w(t-t')$ the weighting function with the non-trivial value over the averaging window which is equal to the correlation time. Several kinds of weighting functions were tried, which gave similar results to the simple average method, which is used here for simplicity. Figure 4.4 shows the coarse-grained time series for all slip systems. It is apparent that the oscillation in coarse-grained series $\dot{R}^l_{\mathrm{cg}}(t)$ is much smaller than original ones $\dot{R}^l_{\mathrm{cs}}$ especially for active slip systems, inferred from the comparison between figure 4.4 and 4.1. The final cross-slip rates range from 0.005/ns to 0.015/ns, depending on individual slip systems, contrary to what is thought before in [155] which implies a constant universal cross-slip rate for all active slip systems. Slip systems l = 5,6,7, and 8 in general remain to be trivial and oscillatory due to their inactivity.

The coarse-grained data $\dot{R}^l_{\mathrm{cg}}(t)$ is only the volumetric average cross-slip rate at time t. This can now be split into the ensemble average $\bar{\dot{p}}^{\mathrm{cs}}_l(t)$ and spatial fluctuation $\dot{\xi}^{\mathrm{cs}}_l(\mathbf{x},t)$ for the cross slip probability, for use in continuum simulations. A smoothing process is used here to recast the coarse-grained cross-slip rates in this form, namely equation (4.2).

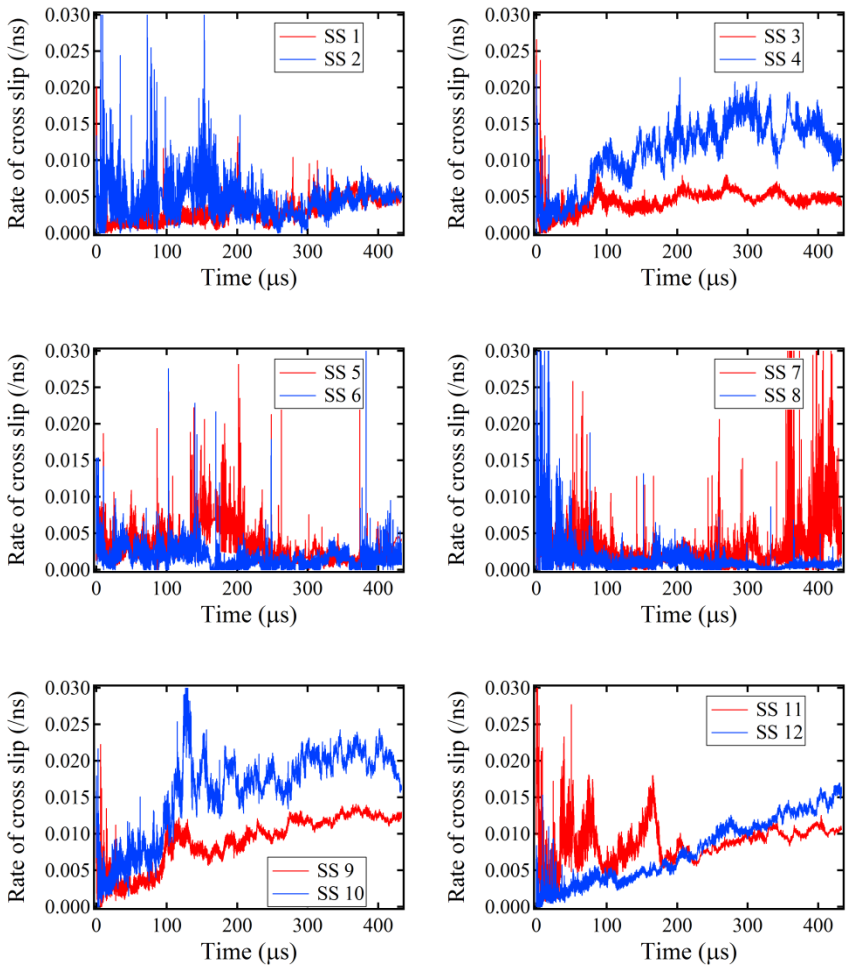

Figure 4.4. The coarse-grained time series of cross-slip rates on all slip systems. The coarse-grained time series is much less oscillatory than the original ones shown in figure 4.1. It is noted that the final cross-slip rates are not the same even within active slip systems.

A segmentation of the coarse-grained series was performed again before the smoothing process, given that the coarse-grained series is also piecewise stationary and that a probability density function only holds for a stationary segment. It is within the expectation that $\bar{\dot{p}}_l^{\mathrm{cs}}(t)$ should be smoother than the coarse-grained series because its fluctuation term $\dot{\xi}_l^{\mathrm{cs}}(\mathbf{x},t)$ has been separated out. The method of GLR is used but for

coarse-grained series plotted in figure 4.4. Locally Weighted Scatterplot Smoothing (LOWESS) method [197,198] is used for the smoothing process. Figure 4.5 illustrates the idea: one zoomed-in sub-series is replaced with a smooth trend $\bar{\dot{R}}^{l}_{\mathrm{cg}}$ plus a fluctuation term $\delta\dot{R}^{l}_{\mathrm{cg}}$, from the latter of which the probability density function is generated and plotted on the right inset. The example is chosen from slip system 3. The above procedure is repeated for each stationary segments and the final smoothed cross-slip rates are plotted in figure 4.6, where the fluctuation is not shown for clearness reason. The terms in equation (4.2) now have their concrete data input as:

$$\bar{\dot{p}}^{\mathrm{cs}}_{l}(t)=\bar{\dot{R}}^{l}_{\mathrm{cg}}(t),\quad \dot{\xi}^{\mathrm{cs}}_{l}(t)=\delta\dot{R}^{l}_{\mathrm{cg}}(t),\quad \text{and}\quad \dot{p}^{\mathrm{cs}}_{l}(\mathbf{x},t)=\bar{\dot{p}}^{\mathrm{cs}}_{l}(t)+\dot{\xi}^{\mathrm{cs}}_{l}(\mathbf{x},t)\,. \tag{4.9}$$

In the implementation of equation (4.9) in the continuum model, the fluctuation term $\dot{\xi}^{\mathrm{cs}}_{l}(\mathbf{x},t)$ is sampled from the cumulative density function for $\dot{\xi}^{\mathrm{cs}}_{l}(t)$ within respective segments.

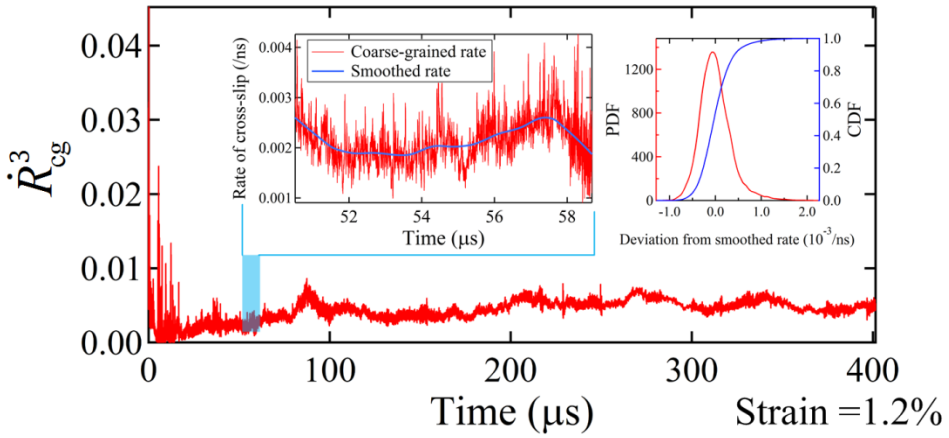

Figure 4.5. The smoothing process for extracting a trend plus a fluctuation. The $\dot{R}_{cg}^3(t)$ series, which is chosen as an example, is first divided into stationary segments (one of them is zoomed in in the left inset) and then the smoothing process is done within each segment. A probability density function and a cumulative density function for the fluctuation term is plotted on the right inset, which is used for sampling.

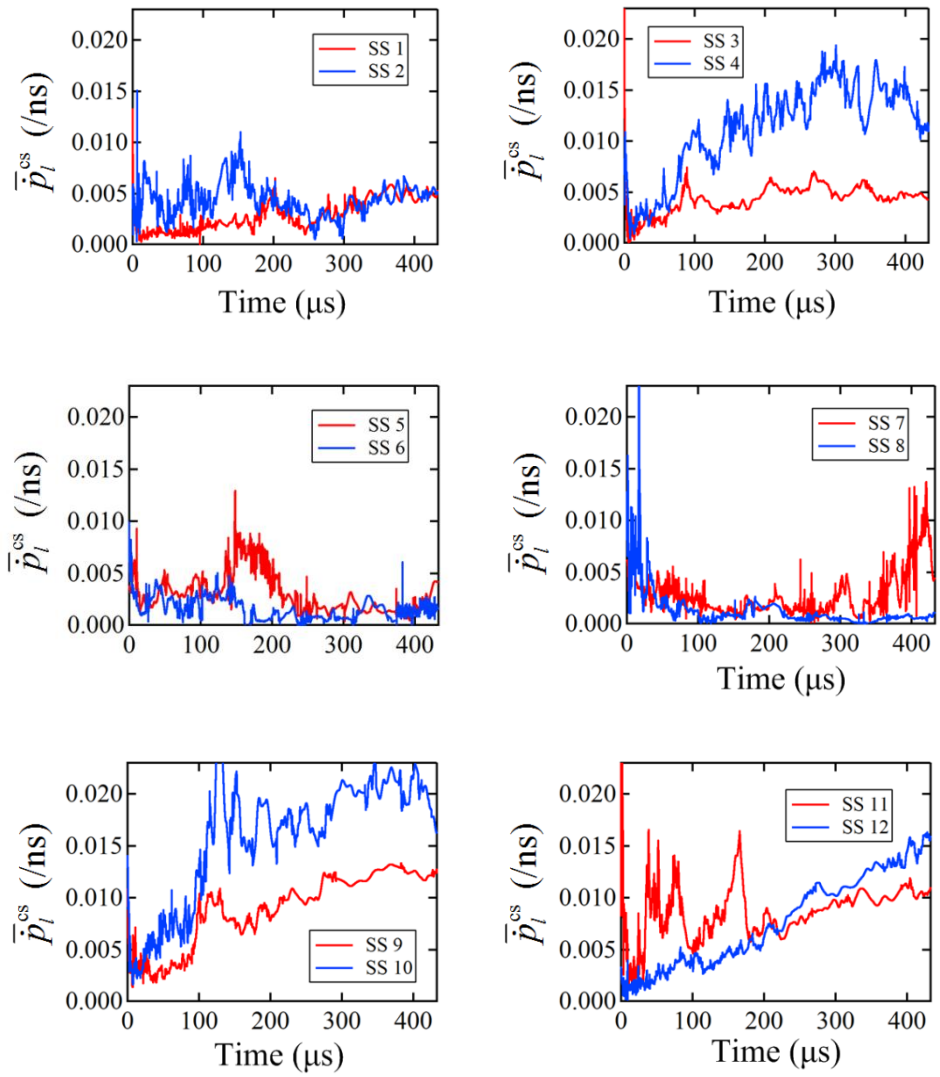

Figure 4.6. The smoothed cross-slip rates for all slip systems. The ensemble average term $\dot{\bar{p}}_l^{cs}(t)$ in equation (4.2) is set to be equal to the value plotted above for corresponding slip systems. The spatial fluctuation term $\dot{\xi}_l^{cs}(\mathbf{x},t)$ is not plotted here but is implemented in the continuum model by sampling process.

CHAPTER 5. MODEL RESULTS: MONOTONIC LOADING

In this chapter, the results from the implementation of the continuum model outlined in chapter 3 are presented. A copper single crystal of the same size with the one used in discrete simulation in chapter 4 is subjected to monotonic loading which is controlled by the strain rate of 30/s. The initial dislocation density is also set approximately equal to the discrete simulation, which is about $1.0\times10^{12}/\mathrm{m}^2$. The simulations are carried out with the numerical scheme given in 3.4 and the program is parallelized with Message Passing Interface (MPI) protocol. It takes about several hundred cores on Purdue University's Hansen and Rice clusters for the continuum model to reach about 1.5% strain level in one month. Admittedly, it is a heavy computational task partly due to the reason that the stiffness matrix for kinetic equations must be recalculated during each time step. But it is still a decent one considering that the 3D feature associated with the mesoscale simulation. The corresponding discrete simulation would be initially faster, as it takes only about 2 weeks for it to reach the same strain level but the computational performance in discrete simulations drops so fast that it almost suspends after 1.5% or so. In the case of continuum simulation, the initial computational performance is not as fast as the discrete one due to the solution of equation on a fine mesh, but that computational speed never drops and keeps almost constant regardless of dislocation population.

The results obtained by the continuum model are compared with both discrete simulations and experiments. The emphasis of the results is given to dislocation patterns under different simulation conditions. This chapter investigates two factors that may influence the simulation results: the cross-slip and loading orientation. Four cross-slip conditions are used for investigation of cross-slip influence, they are: no cross-slip, constant large cross-slip rate, constant smaller cross-slip rate and cross-slip rates obtained from discrete simulation. In general, when the cross-slip rates from discrete simulation are employed by the coarse-graining process discussed in chapter 4, the simulation yields realistic results. On the other hand, the similitude relationship [99] seems to be unchanged by the variation of cross-slip rates, neither by the number of slip systems implemented in the simulation.

The monotonic loadings are also arranged in three directions: [001], [110], [111] respectively to investigate the orientation dependence. For this purpose, the cross-slip data are provided from the corresponding discrete dislocation simulations in these three directions. The results are compared qualitatively with experiments which are often aimed at dislocation patterns at finite strain levels (>10%, e.g.). For convenience, the simulation examples in this chapter are numbered and their differing conditions are listed in table 5.1. Aside from these differences, all other parameters used in all simulations are set the same, see table 5.2.

Table 5.1. Simulation conditions

Simulation index	Number of SS[a]	Cross-slip scheme	Tensile orientation
I	8	No cross-slip	[001]
II	8	$\delta p_l^{cs} = 0.48$	[001]
III	12	$\delta p_l^{cs} = 0.1$	[001]
IV	12	Equation (4.2)	[001]
V	12	Equation (4.2)	[110]
VI	12	Equation (4.2)	[111]

Note: [a]SS stands for slip system(s).

Table 5.2. Simulation parameters

Parameter	Value
Strain rate	30/s
Young's modulus	117GPa (copper)
Poisson ratio	0.34 (copper)
Initial dislocation density	$1.07 \times 10^{12}/m^2$
Magnitude of Burgers vector	0.256 nm (copper)
Dislocation mobility	10^{-4} $Pa^{-1}s^{-1}$

5.1 Strain Hardening in [001] Axis

This section discusses results of simulations I and II, in which the loading axis is in [001] direction. These two sets of simulations both have eight slip systems but differ in the activation of cross-slip. Subsection 5.1.1 presents the results regarding the statistical quantities while subsection 5.1.2 discusses dislocation density patterns with and without cross-slip activation.

5.1.1 Statistical Quantities Given by Continuum Model

Simulation I and II differ in their activation of cross-slip. In order to manifest the effect of cross-slip, the probability δp_l^{cs} is set to be much larger than the actual ones obtained from discrete simulation. The curves of stress and average dislocation density against applied strain for simulation I and II are plotted in figure 5.1. The average dislocation density is calculated from the following expression:

$$\begin{aligned} \bar{\rho}_{\Omega} &= \frac{1}{\Omega}\int_{\Omega} \rho_{\mathrm{Total}} \mathrm{d}\Omega \\ \rho_{\mathrm{Total}} &= \sum_{l=1}^{N} \rho^{l} = \sum_{l=1}^{N} \sqrt{(\rho_1^l)^2 + (\rho_2^l)^2 + (\rho_3^l)^2} \end{aligned}, \tag{5.1}$$

where ρ^l is dislocation density scalar on slip system l , N the number of slip system and in simulations I and II, $N = 8$; Ω the whole simulation domain, ρ_{Total} the total density at one spatial point.

The yielding points are much higher in continuum simulations than in discrete simulations and experiments. Several reasons are responsible for the unrealistically high

stress level. First of all, there are only eight active slip systems simulated in simulations I and II. The inactive slip systems, although they do not contribute many dislocations to the slip systems [155], they still have influence over the simulation results through interaction with dislocations on active ones. The absence of elastic anisotropy in the implementation of the elastic part of the model might also contribute to the high yielding point and flow stress according to discrete dislocation simulation [182]. The results also show a certain degree of the mesh dependence [199] since the distance between two slip plane of the mesh is much larger than the annihilation distance of edge dislocations. It is also seen that the crystal exhibits strain hardening almost immediately after the yielding point. This arises from the symmetry of all active slip systems regarding the axis of tensile loading.

The cross-slip activation is found to have considerable effect on the simulation results. On the mechanical part, the activation of it brings down the yielding point but increases the hardening rate. At first, the motion of dislocations is enhanced by cross-slip, which induces the ‘softening’ of the material. At larger strain values, however, cross-slip leads to density multiplication and rapid hardening. Therefore, an unrealistically high cross-slip level brings about an unrealistically high hardening rate to simulation II. On the dislocation part, the activation of cross-slip gives rise to the continual increase of average dislocation density due to the same reason of mutual interaction.

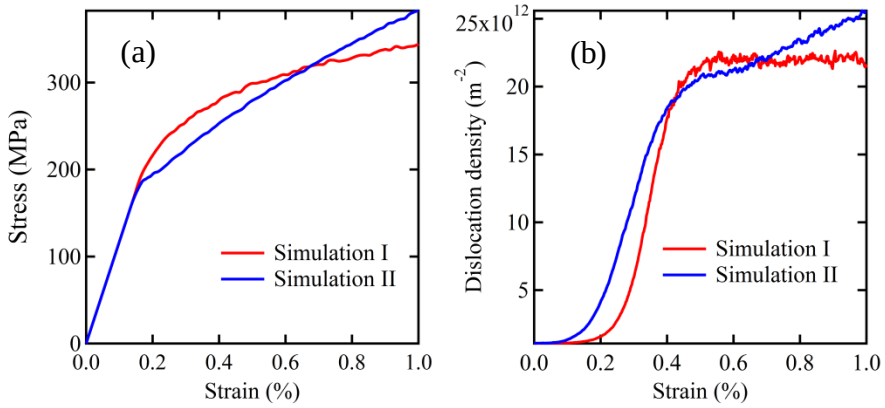

Figure 5.1. Stress-strain (a) and dislocation density evolution (b) curves for simulation I and simulation II. In simulation I, cross-slip is disenabled whereas in simulation II cross-slip is deliberately set at an unrealistically much higher level in order to check its influence.

5.1.2 Dislocation Density Pattern

The patterns of total dislocation density ρ_{Total} in equation (5.1) for simulations I and II is captured at strain level of 0.5% and plotted in figure 5.2 where the patterns without and with cross-slip activation are distinguished clearly by the cell structure formed in the latter case. From the surface view in figure 5.2(b), the cell structure is composed of two parts: the wall-like dislocation-dense areas and dislocation-free regions. Figure 5.2(c) shows that the network of total dislocation density exists in 3D space and when projected onto on (001) section, cell structure is observed there. The comparison between dislocation pattern without and with cross-slip demonstrates the positive influence of cross-slip on the formation of dislocation patterns, which coincides with previous discrete dislocation simulations [172].

The emergence of cell pattern, which was found in experiments but at finite strain level [200], is related to the subdivision and recrystallization of a single crystal. The much earlier appearance of the cell structure in the simulation II is of course due to the unrealistically high cross-slip rate, since the cross-slip of screw dislocations favours the formation of dislocation patterns. It is also to be noted that the TEM micrographs of dislocations are obtained on thin foils of thickness up to hundred nanometers and their preparation requires polishing and other kinds of treatments [53]. So TEM micrographs actually do not capture total dislocations due to relaxation. Recent results of TEM image also report the organization of dislocations into cell-like structure in 2% deformed pure copper [201].

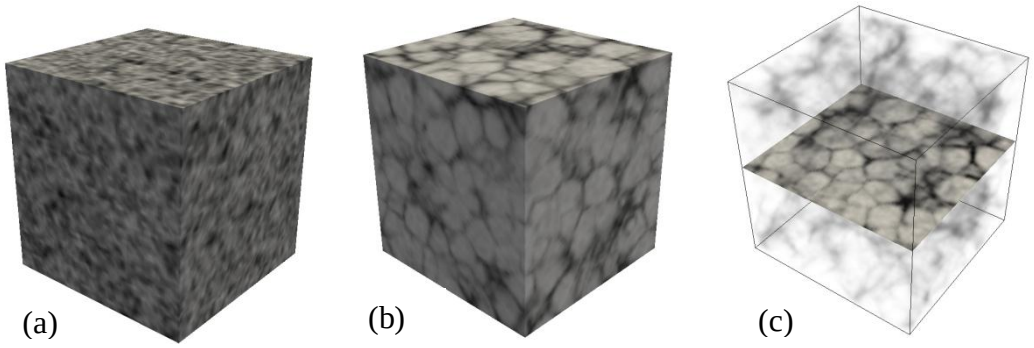

Figure 5.2. Dislocation density patterns for simulation I (a) without cross-slip and simulation II (b and c with cross-slip) at strain level of 0.5%. Cell structure is obvious when the cross-slip is activated with a large probability (~0.48). (c) shows the transparent view of dislocation density in 3D space and cell structure on (001) plane.

The distorted shape of the crystal is plotted in figure 5.3(a) and (b) for the correspondent states in figure 5.2(a) and (b) by adding the perturbed displacement $\tilde{\mathbf{u}}$ in

equation (3.21) to the original nodal positions. The displacement associated with the average strain $\bar{\boldsymbol{\varepsilon}}$ is removed to amplify the distortion of the crystal by plotting $\tilde{\mathbf{u}}$ only. When the cross-slip is disabled, the slip pattern on the surface of the cube is mainly in parallel with <110> type slip directions, represented by solid line in figure 5.3(a), and the traces of slip planes on the surfaces, represented by dashed line in figure 5.3(a). They are formed by dislocations leaving the surface. However, when cross-slip is activated, the distorted shape shows granular feature and the straight slip bands associated with single slip behaviour do not dominate any longer.

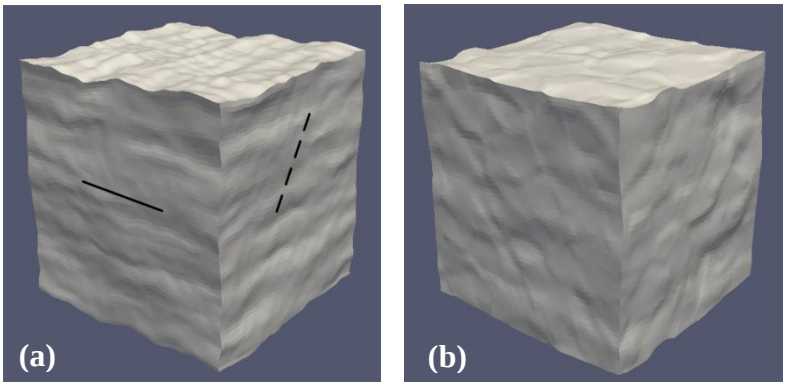

Figure 5.3. Crystal distortion in simulation I (a) and II (b) at 0.5% strain. The linear displacement associated with average strain is suppressed and only the perturbation displacement $\tilde{\mathbf{u}}$ is displayed with a magnification of 200 times.

The above results of stress-strain and dislocation density curves have demonstrated the ability of the continuum model to predict the mechanical and microstructural phenomena in single crystal in qualitative agreement with experiments. Cross-slip is demonstrated to have influence on both the macroscopic behaviour of the single crystal

and the microstructural formation of dislocations. In the following sections, simulations III and VI are presented by changing the schemes of cross-slip implementation as well as the number of slip systems. The purposes are to adjust the simulation conditions to realistic situations in experiments as well as to investigate the influence of cross-slip and number of slip systems in monotonic strain hardening.

5.2 Influence of Cross-slip Rate on Results

The number of simulated slip systems in simulations III and IV is set to be 12 and they are controlled by two different schemes of cross-slip: a constant cross-slip probability $\delta p_l^{\mathrm{cs}} = 0.1$ and the cross-slip rates given by equation (4.2) where the data are specified by equation (4.9) through the coarse-graining process applied to discrete data. The stress-strain and dislocation density curves for simulations III and VI are plotted in figure 5.4.

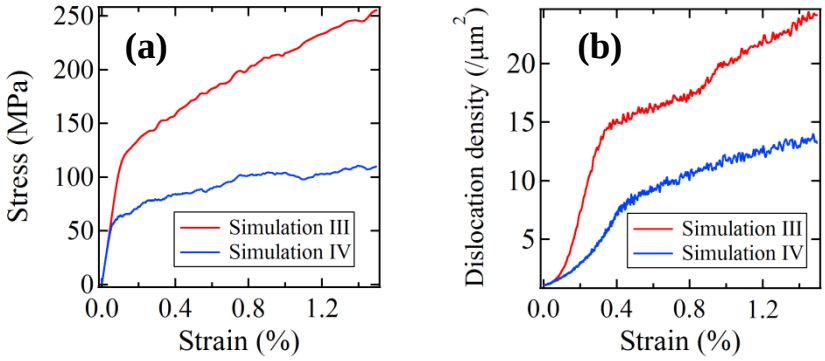

Figure 5.4. The stress-strain (a) and dislocation density evolution (b) curves under simulation conditions III and IV where all twelve slip systems are activated.

By incorporating cross-slip rate from discrete simulation, the yielding point in simulation IV reduces about one half from simulation III to about the same magnitude given by the discrete simulations and experiments, and the hardening rate also decreases. The cross-slip probability in simulation IV is about 0.03 in each time step, which is only one third of the probability implemented in simulation III (~ 0.1). Thus, the significantly high cross-slip rate in simulations II and III makes the material 'harder.' Ignoring the cross slip difference between active and inactive slip systems in simulation III exaggerates the effect of cross-slip.

The calibrated cross-slip rates for inactive slip systems are actually close to trivial. Although the stress level after the incorporation of discrete data in simulation IV is still larger than the experiments [45], which is because of the lack of short range reactions and the mesh size dependency, it is already shown here that the incorporation of parameters from discrete dislocation simulation improves the performance of the continuum model to a great extent.

The total dislocation patterns are plotted in figure 5.5 for simulations III and IV at three strain levels. The cell structure in simulation III emerges immeidately after yielding and develops quickly to a a very clear version as seen in figure 5.5(c). During their evolution, cells seem to increase in number and decrease in their average sizes. A finer cell structure contributes to strain hardening process by reducing the mean free path [132] of dislocations which are impeded or trapped by the network of cell structure.

In simulation IV, where the cross-slip rates are obtained by coarse graining, the dislocations organize into cell structure at a slower pace. At the strain level of 1.28%, the clarity in the dislocation density pattern is close to the one of simulation III at the strain level of 0.5%. Besides, the cell size in figure 5.5(f) appears to be larger than the one in figure 5.5(c), resulting in a smaller value in flow stress. That is, the implementation of parameter from discrete dislocation simulation defers the formation of cell structure and its subsequent fragrmentation process. According to the observation in section 5.1, cross-slip has positive influence on the formation of cell structure, so a smaller cross-slip rate implemented in simulation IV than in simulation III delays the emergence of cell structure. The late emergence of the cell structure at the level around or above 1.5 % is more in accordance with experiments [201].

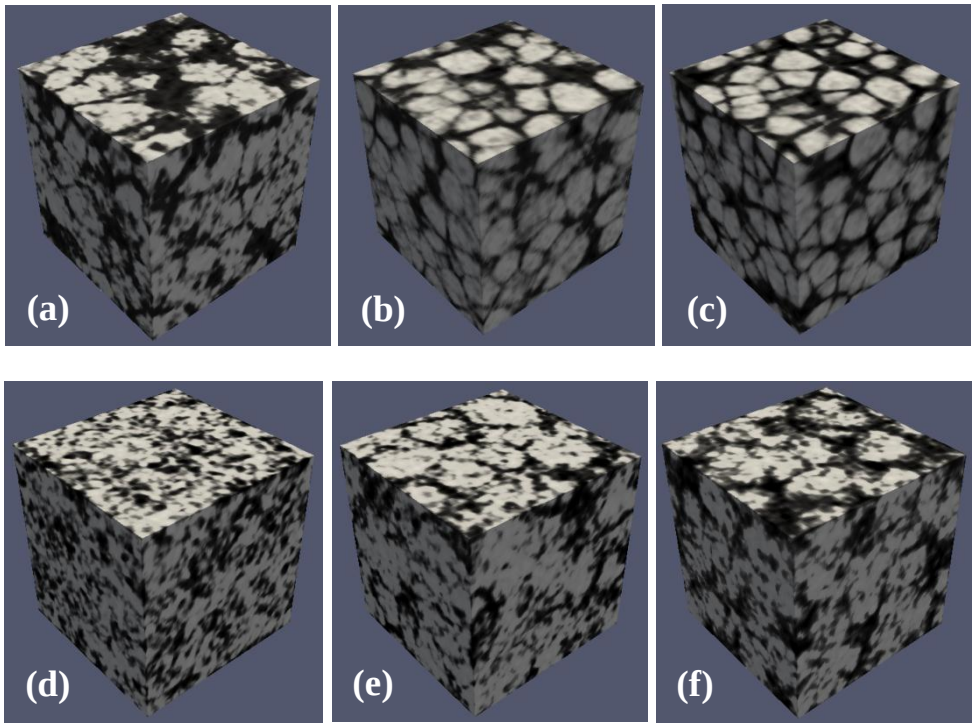

Figure 5.5. Dislocation density patterns from simulations III ((a), (b), (c)) and IV ((d), (e), (f)). The first, second and third columns correspond to strains of 0.5%, 1.0%, and 1.28% respectively. It is seen that the cell patterns in simulation III is clearer than in IV because of the difference in the setting of cross-slip rates.

One can see that the simulation examples from I to IV differ in cross-slip rate and the number of slip systems. The results from these simulations vary from no cell pattern to a clear cell structure. It is thus of interest to examine from these cases the common law that governs the feature of dislocation patterns. One of the relationships that is widely accepted and observed is the similitude law [202,203] which states the relationship between resolved shear stress and pattern wavelength of dislocation structures. In the following section, the attempt is made to extract the similitude law by measuring the average cell sizes.

5.3 Similitude Law

The similitude law for dislocation microstructures states that the wavelength for dislocation density pattern is inversely proportional to the resolved shear stress, which can be expressed in the following formula [202]:

$$\frac{\lambda}{b} = K\frac{G}{\tau}, \tag{5.2}$$

where λ is the average wavelength of the pattern, b the magnitude of Burgers vector, G Shear modulus, τ the resolved shear stress, K similitude coefficient. The average wavelength λ can be calculated from the 2D dislocation structure which is sliced from the 3D structure as shown in figure 5.2(c). The following procedures are implemented to obtain the representative λ for [001] type loading.

First of all, 20 sections parallel to (001) plane are made to display dislocation density patterns on them. For each section, the Gaussian blur and sharpening algorithms are applied successively to make the cells more salient. Watershed method [204], which is one of the methods widely employed in the segmentation of grey-scale images [205], is used to detect cells, yielding the result illustrated in figure 5.6(b). The area of each cell, A_i, is calculated by pixel counting and an equivalent diameter d_i is obtained by:

$$d_i = \sqrt{\frac{4A_i}{\pi}}. \tag{5.3}$$

The same process is repeated for all cells on the 20 sections and the wavelength is defined as the average value of d_i:

$$\lambda = \sum_{i=1}^{N_{cell}} d_i \,, \tag{5.4}$$

where N_{cell} is the total number of cells detected on all sections.

The above mentioned process is repeated at different strain levels for simulations II, III and IV, and for I no effort is made for measuring cells because there is no cell formation. The resolved shear stress τ is calculated by multiplying the hardening stress with the Schmid factor of active slip systems. It is investigated through experiments [58,82,83,85] and previous simulations [99] that the similitude coefficient K ranges from 5.0 to 10.0 under different circumstances.

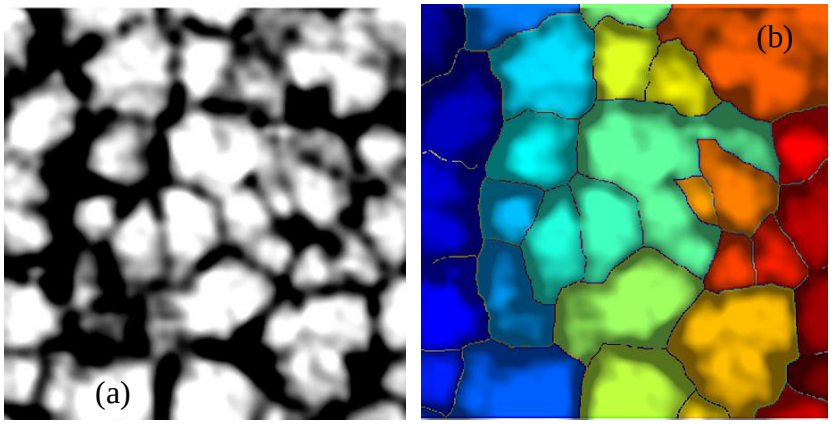

Figure 5.6. Watershed method for the detection of cell structure on (001) sections. (a) displays the dislocation density pattern processed by highlighting the contrast. (b) shows the cells detected from pattern (a) by using watershed method. The sample used here is from simulation III, at the strain level of 1.5%.

Based upon the data obtained from continuum dislocation model and the average wavelength calculated from equation (5.4), the relationship between λ/b and G/τ is

plotted in figure 5.7 for simulation samples II, III, and IV. For each simulation condition, an attempted line is fit for discrete sampled points which are computed from the above mentioned procedures. It is to be noted that the error bar associated with each point stands for one standard deviation from the mean value of cell sizes. The attempted coefficients in all three simulations are 7.48, 7.53, and 7.06 respectively, all of which are in accordance with experimental results [202] which are in favour of similitude coefficient around 7.0. Another important phenomenon seen from figure 5.7 is that all sampled points seem to be located around a common line indicated by a dashed line, despite the differences in simulation conditions in terms of the numbers of slip systems and cross-slip schemes, and also the difference in the value of resolved shear stress between simulation IV and the other two.

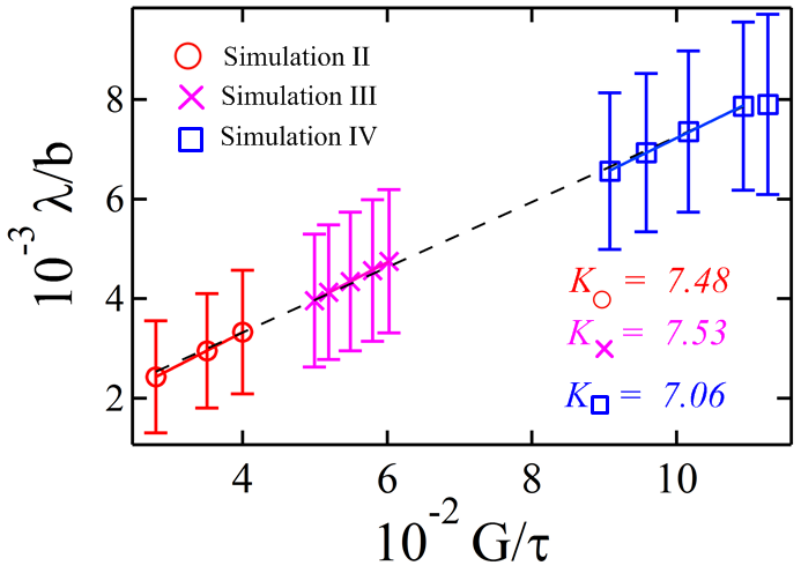

Figure 5.7. The simulation law attempted from three simulation conditions with various schemes in cross-slip rates and the numbers of simulated slip systems. A line is fit to the sampled points in each condition, which yields coefficient K around 7.0. In spite of different conditions applied, all sampled points appear to be around the same line (dashed) whose tangent is estimated to be $K \approx 6.56$.

The conformity to the same similitude law of all data indicates that the main reason for hardening stress is the wavelength of dislocation patterns. A pattern featured by a smaller average cell size shrinks the space for dislocations to move freely and enhances the probability of the immobilization. Thus, the material is hardened by the loss of freely moving dislocations, or saying the loss of capability for the accommodation of plastic strain. Furthermore, the relationship between the flow stress and wavelength is demonstrated to be fixed by a linear relationship characterized by a constant similitude coefficient K. The coefficient is relatively smaller in simulation IV, which might be attributed to the clarity of the cell patterns. If the dislocation pattern is as blurred as seen

in figure 5.5(e), it becomes hard to clarify a cell region and the detected cell patterns suffer from over-segmentation by watershed method [204], resulting in underestimated radii of cells.

On the other hand, the observation of a similitude law in figure 5.7 demonstrates that λ given by equation (5.4) suffices to represent the characteristic wavelength that should ideally be calculated from a 3D analysis, at least when the cell structure is full-fledged.

5.4 Orientation Dependence of Crystal Response

The dislocation patterns under different loading orientations did not show dissimilarity with each other in the early experiments [79]. But more experiments [45,200,206–209] have demonstrated that the structures of dislocation walls are influenced considerably by the orientation of tensile axes, which is supported by further examinations on both polycrystalline [74] and single crystalline [75]. Reference [75] renders a compilation of experimental results and divides dislocation structures into three types, each of which is associated with a domain in the stereographic triangle of an FCC material. From all the results reviewed, in general, a monotonic tensile loading around <001>-type direction favours the formation of near isotropic cell structures as has been shown in figure 2.1(b); tensile loading around <111>-type orientation direction facilitates the concentration of dislocations onto {111}-type slip planes, but with a deviation angle of about 30 degrees, forming dislocation walls as seen in figure 2.1(c); tensile axes in the most part of stereographic triangle which are in favour of single slip activation result in dislocation walls orientated very closely to slip planes with a mere deviation of 2-3 degrees.

Reference [76] provides with the compilation of types of patterns associated with tensile orientations in a stereographic triangle.

These results from experiments motive the interest of investigating the dependence of dislocation patterns in the simulation. Simulations V and VI are thus initiated to subject the cube to [110] and [111] monotonic loadings to examine the orientation dependence. The loading orientation is applied by varying the applied strain tensor $\bar{\boldsymbol{\varepsilon}}$ in equation (3.21). The magnitude of strain is kept in the simulation to be within the domain of small deformation (around 1.0% or so), in contrast to experiments where the specimens are often loaded up to finite strain level (above 10% or even close or above 100%). It is done so for theoretical reason that the continuum model is built upon small deformation assumption and for practical reason that quite amount of computational resources are required for the simulation even up to 2.0%.

It is important to note that the cross-slip rates should also be obtained from the corresponding discrete simulations of different loading axes, since orientations have direct effect on the activated slip systems through Schmid factors. To this end, discrete dislocation simulations are performed with [110] and [111] orientations for the collection of data of cross-slip rates. The method used for coarse-graining is the same as stated in chapter 4.

This section first presents the orientation dependence of cross-slip rates and the stress-strain curve. The results are compared between discrete and continuum simulations. Then the attempts are made to compare patterns in continuum numerical simulations with experimental data in all three tensile axes. Subsection 5.4.2 presents a qualitative comparison in 3D cube and on 2D slices; subsection 5.4.3 gives an analytical way to

draw the angle feature from the simulations and compare the deviation angles with those conventionally measured in experiments.

5.4.1 Orientation Dependence of Cross Slip

The coarse-graining process for cross-slip rates detailed in chapter 4 is done to the data collected from discrete dislocation simulations in [110] and [111] orientations. The final smoothed trends for [110] and [111] loadings are respectively plotted in figure 5.8 and 5.9 for all slip systems. It is important to keep in mind that fluctuation term $\delta\dot{R}^{l}_{\mathrm{cg}}(t)$ in equation (4.9) is not plotted in these two figures for clarity but is implemented by sampling the cumulative density functions that are obtained piecewise as discussed in chapter 4.

For [110] loading, the indices of active slip systems are 1, 4, 9 and 11, whose Schmid factor in magnitude is 0.408, the same as in [001] loading. Being different from [001] loading, the cross-slip rates turn out to be more complicated in terms of active and inactive slip systems. It was concluded that the cross-slip rates increase with applied strain on active slip systems but remain trivial on inactive slip systems in [001] loading, such is not the case in [110] loading. The similarity in cross-slip rates between collinear active slip systems does not exist either, e.g. slip system 1 and slip system 2. The reason for the complexity in cross-slip rates lies in the fact that the no pair of collinear slip systems is activated simultaneously in [110] loading situation. The slip systems 1, 4, 9, 11 are active slip systems, but their collinear slip systems are not. Thus the asymmetry of a pair of collinear slip systems regarding [110] loading axis brings about the less correlation in cross-slip rates between them and adds more complexity. During the

implementation of discrete dislocation simulations, the comparison is made between the resolved shear stresses on gliding plane and cross-slip plane such that the later must be larger than the former one for an actual occurrence of cross-slip [104]. In the case of [110] loading, the resolved shear stress on only one of a pair of collinear slip systems is stably influenced by the external loading and another one is entirely dominated by the internal stress which is more sporadic in time and space.

The active slip systems under [111] loading are 3, 4, 7, 8, 11 and 12 with a Schmid factor of about 0.272. Slip systems 3 and 4, 7 and 8, and 11 and 12 are pairs of collinear slip systems respectively. It is seen in figure 5.9 that each pair of them shares a similarity in the trends of cross-slip rates, due to the symmetry reason. It is noted that cross-slip rate on collinear slip systems 3 and 4 increases very slowly comparing with the other two pairs. The initial configurations of dislocations might play a role in the evolution of cross-slip rates for individual slip systems. Figures 4.6 , 5.8, and 5.9 together show dependence of cross-slip rates on different loading orientations. It is thus reasonable to incorporate cross-slip rate into the continuum model to represent a real situation before any possible laws are found.

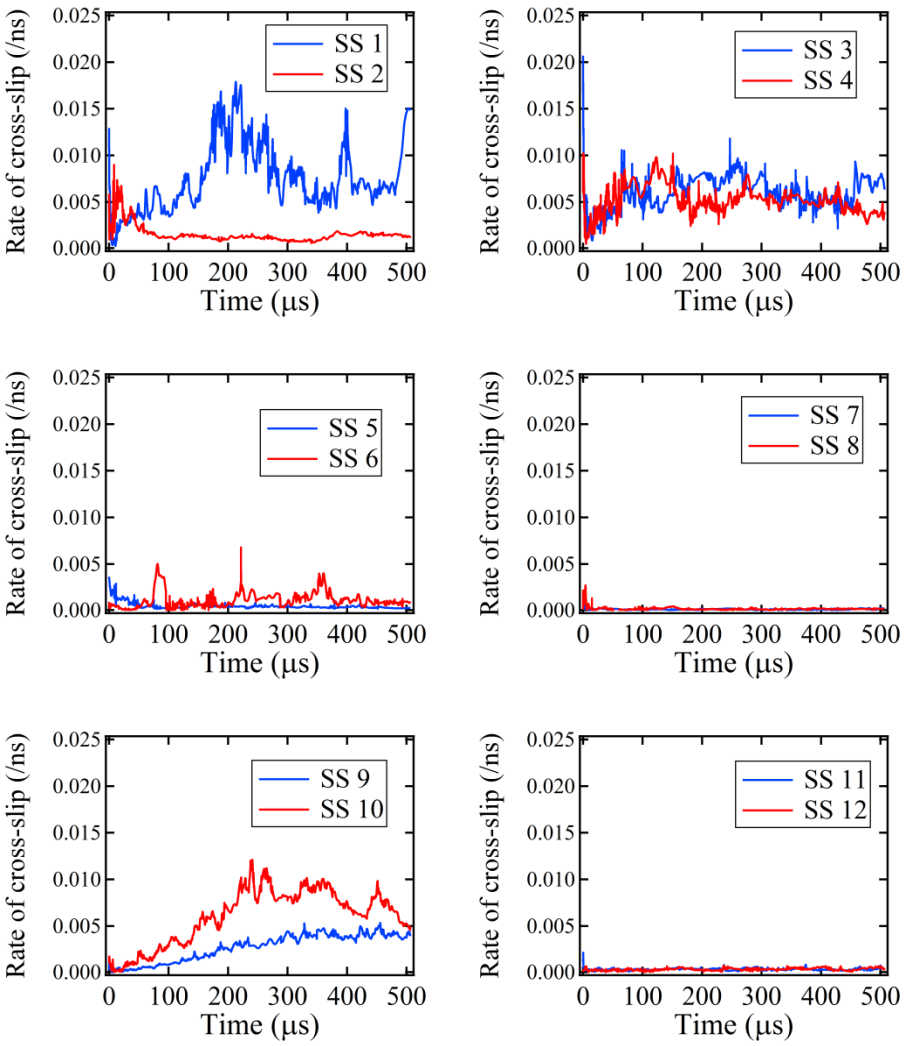

Figure 5.8. Cross-slip rates obtained from discrete dislocation simulation. The loading axis is along [110] direction. The behaviour of cross-slip rates exhibits complexity. Slip system 11 is active but cross-slip rates of it keep being trivial through the simulation. Slip system 1 and 2 are collinear slip systems but exhibit different evolution trends.

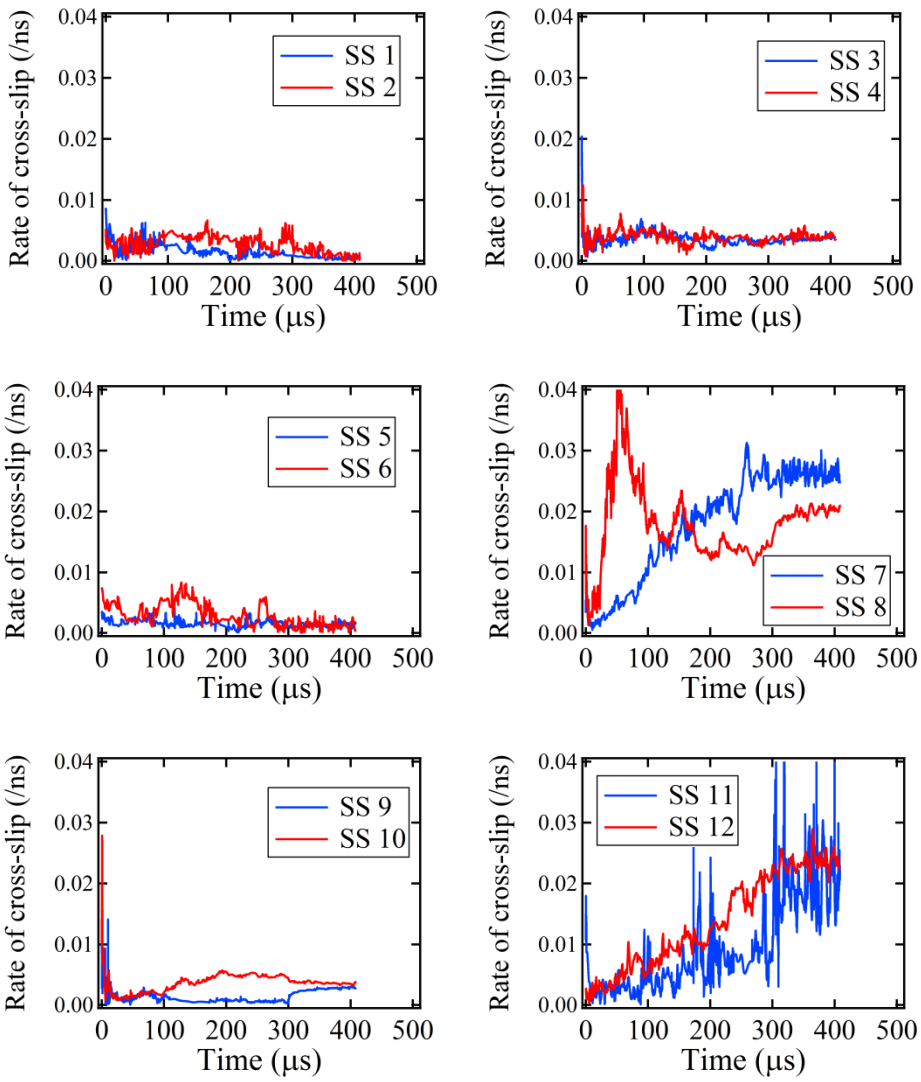

Figure 5.9. Cross-slip rates obtained from discrete dislocation simulation. The loading axis is along [111] direction. Each pair of collinear slip systems exhibits similar evolution path in cross-slip rates due to their symmetry regarding the loading axis.

Figure 5.10 shows the results of stress-train and dislocation density curves by discrete dislocation simulation and continuum simulations which take the cross-slip rates shown in figure 4.6, 5.8 and 5.9 as trends. In figure 5.10(a) and (c), the stress is calculated as the average stress along the tensile axis. The total dislocation density is calculated from equation (5.1) for continuum simulation and calculated by the following equation:

$$\rho_{\text{Total}}^{\text{dis}} = \frac{1}{V}\sum_{i=1}^{N_{\text{seg}}} l_i \,, \tag{5.5}$$

for discrete simulation, where l_i is length of segment i, N_{seg} the total number of segments on all slip systems, V the volume of the body.

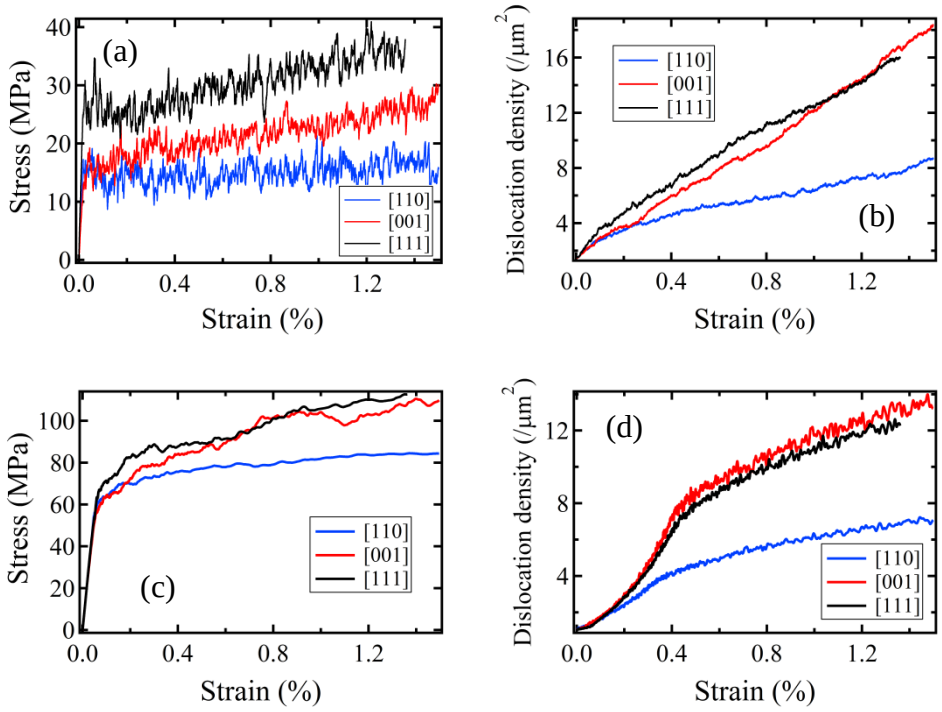

Figure 5.10. Stress-strain and dislocation density curves by discrete dislocation simulations, (a) and (b), and continuum simulations, (c) and (d). The orientation dependence shown from discrete and continuum simulations is in qualitative agreement with each other.

In both discrete and continuum simulations, the hardening rate for [111] direction loading tends to be highest, followed by [001] and [110] loadings. The Schmid factor in [111] loading (~0.272) is smaller than in the other two orientations (both of ~0.408). When the crystal is oriented in a direction with smaller Schmid factor, most of the applied strain is accommodated elastically, which results in larger stress. In simulating the [110] loading case, the Schmid factor is as large as in [001] loading (~0.408) but the number of active slip systems (4 in [110] loading) is only as half of those in [001] loading. This leads to less interaction between dislocations on different slip systems in the case of [110] loading and a lower hardening rate and slow variation of the flow stress with

applied strain. For the same reason, the dislocation multiplication in the case of [110] loading is also limited compared with [001] and [111] loading.

5.4.2 Orientation Dependence of Dislocation Microstructures

In addition to the above mentioned orientation dependence of cross slip rates, Schmid factor and the number of active slip systems, differences in dislocation patterns were also observed. To this end, figure 5.11, figure 5.12, and figure 5.13 plot dislocation patterns in continuum simulation and in the experiments for <001>, <110>, and <111> types of orientations or in close directions. In those figures, the cube surfaces in simulations are chosen as close as possible to the ones chosen in TEM images for qualitative comparison. In figure 5.11, where <001>-type loading is applied, both simulation and experiment produce images with cell structures on {001} and {110} type planes. When <110>-type loading is applied as shown in figure 5.12, the dislocation structure exhibits orientation preference in the direction of the trace lines of {111}-type slip planes both in the simulation and in experiments. This orientation dependence is also observed in <111>-type loading as plotted in figure 5.13 but to lesser extent.

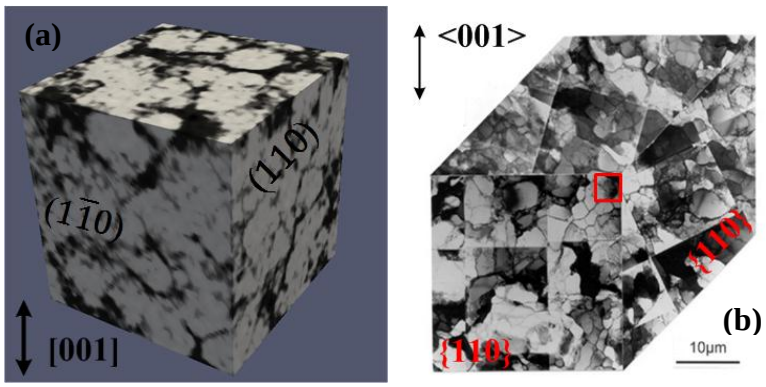

Figure 5.11. Dislocation patterns from (a) continuum simulation at strain level = 1.36% and (b) from experiment at strain level ~34%. The tensile axes for both are of <001> type. The TEM image (b) is taken from [76].

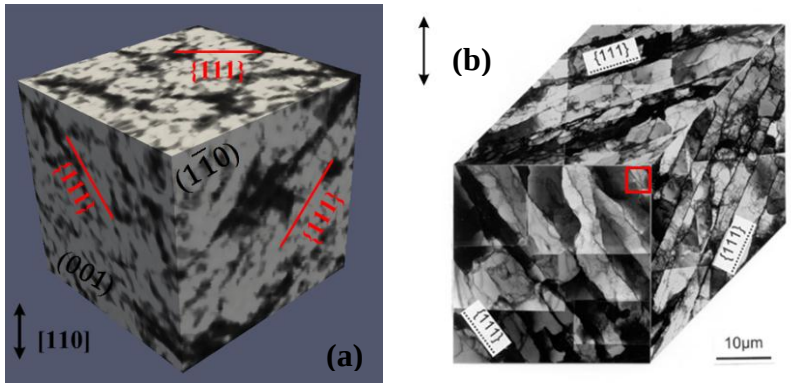

Figure 5.12. Dislocation patterns from (a) continuum simulation at strain level = 1.5% and (b) from experiment at strain level ~34%. The tensile axes for both are of <110> type. The TEM image (b) is taken from [76]. The {111} lines in red in part (a) are traces of {111}-type slip planes. The traces of the same type are shown in (b).

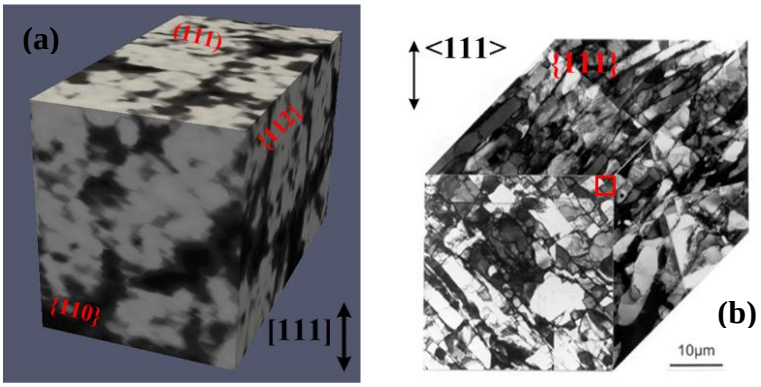

Figure 5.13. Dislocation patterns from (a) continuum simulation at strain level = 1.5% and (b) from experiment at strain level ~34%. The tensile axes for both are of <111> type. the TEM image (b) is taken from [76].

The above comparison between the density patterns on the surface of the 3D cube demonstrates the similarity between continuum dislocation dynamics predictions and experiments. Further comparisons are shown in figures 5.14 and 5.15, where the dislocation density patterns are shown on various crystallographic planes and compared with corresponding experimental data available. The types of the planes as well as the directions of images are kept the same in these figures.

The microstructure on $(\bar{1}01)$ plane in both simulations and experiments for [111] orientation shows similar orientation preference. The image size in figure 5.14(a) is about a quarter of area in figure 5.14(b), coinciding with the difference in dimensions between the two. For loading along [001] direction and on (001) plane (see figure 5.15(a) and (b)), the simulation result agrees well with experimental data in forming the cell structure. The preference in the orientation of dislocation walls is less pronounced in comparison with figure 5.14, where the loading is applied along [111] direction. There exists a difference between numerical simulation and TEM images in figure 5.15(c) and (d), both of which

show (100) sections perpendicular to [001]. The (100) section from simulation data shows isotropic cell structure while the slice of (100) crystallographic planes obtained from TEM shows obvious elongation of dislocation walls along [001] tensile direction. This is because the deformation in the experiment is much larger than in the simulation by orders of magnitude. Consequently, the movement of dislocations in experiments are not only driven by the stress field but also by the motion of material points that they are associated with. The material points have the tendency to move along the tensile direction in the experiment. As a result of this, the dislocation microstructures are also elongated in [001] direction. Such a feature due to finite deformation is neither modelled nor attained in the simulation, which is beyond the scope of current work.

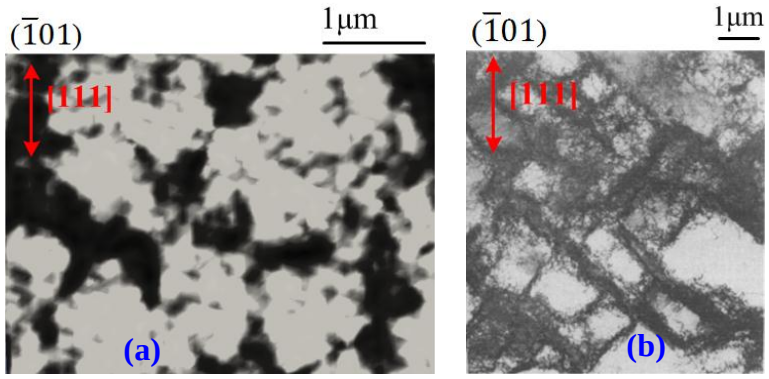

Figure 5.14. Dislocation microstructures on $(\bar{1}01)$ plane for [111] tensile in (a) simulations and (b) experimental data taken from [45]. The domain in simulation is about 4μm and in the experiment is about 7μm. The resolved shear strain is about 0.37% in simulation and 40% in the experiment.

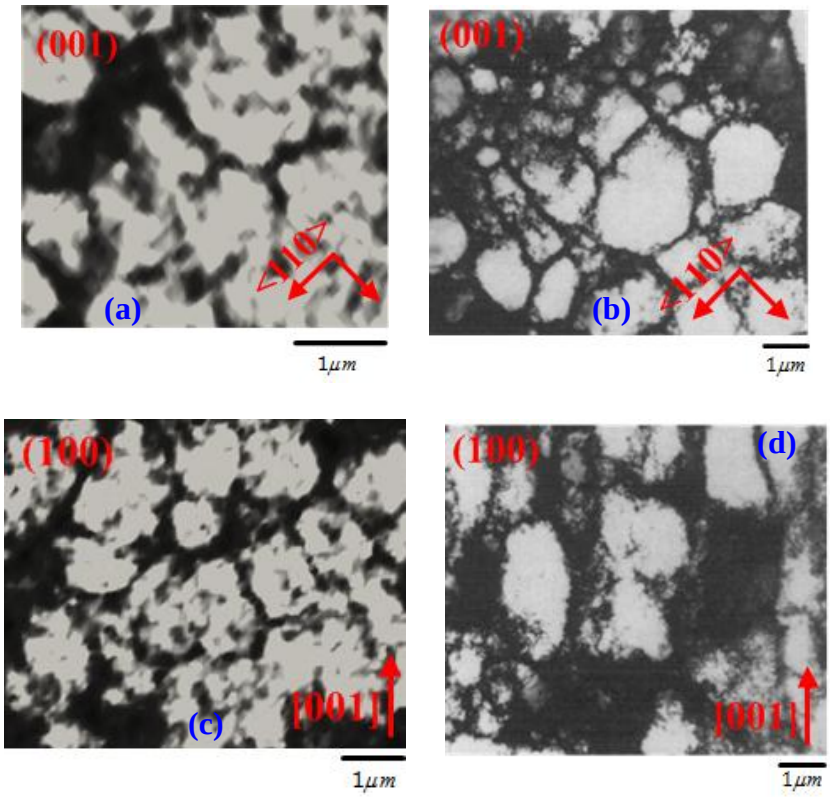

Figure 5.15. Dislocation microstructures on {001}-type planes for [001] tensile in simulations((a) and (c)) and TEM images ((b) and (d)) taken from [45]. The (001) plane shown in (a) and (b) is perpendicular to the tensile axis whereas the (100) plane shown in (c) and (d) is parallel with tensile axis. The resolved shear strain is 0.61% in the simulation and 19% in the experiment.

It is important to point out here that the simulations differ significantly from experiments in both the magnitude of strain and sample size. For the reasons that have been stated, the data provided by simulation fall within the small deformation regime, in contrast to over 10% of strain in the experiments. The dimension of the domain of the simulation domain is also smaller than in experiments for the reason of computational limitation. Despite all these differences, the qualitative agreement between the simulations (at small strain) and the experiments (at large strain level) implicates that

even during the very early stage of strain hardening the dislocations organize into the structure indicative of the microstructure in the succeeding larger strain and such an organization is affected by the orientation of the loading axis in the same way as in the larger strain level.

Quantitative analysis has been accomplished in experiments by measuring the deviation angle of dislocation walls from the slip plane, which is referred to as trace analysis [75,76]. Such a direct measurement is not applicable in case of numerical simulation because, although the dislocation walls have started to show orientation preference, the arrangement of walls is still too vague for their angles to be identified clearly, which is again attributed to the insufficient strain level. However, this issue can be addressed by numerically detecting the orientation of those unclearly oriented images.

5.4.3 Analysis of Dislocation Patterns for Different Tensile Orientations

The 2D autocorrelation function (referred to as ACF) of an image can be used as a tool to recover some hidden facts of an image—including the preferred orientation [210]. For an isotropic pattern, the central part of the ACF is circular with a peak at the origin. Depending on the wavelength of the pattern, other weaker peaks might appear far from the center. For anisotropic patterns, which might not seem clear in real space or are hard to identify by the naked eyes, ACF remains high along the preferred directions of the image and decays faster in the short-ranged correlation directions. In another words, the central part is elongated in certain directions of the image. In the case of the analysis of dislocation density patterns such as in figure 5.14(a), the orientation inclination is obvious but the determination of the exact angle of this inclination may suffer from

subjective judgement. With the hope to detect the angle as objective as possible, the ACF analysis procedures are employed and applied to the images of dislocation density patterns on sections.

By definition, the autocorrelation of an image is the convolution of the image with itself and it is defined in the following formula [210]:

$$\begin{aligned} C_f(\Delta x, \Delta y) &= f(x,y) \otimes f(x,y) \\ &= \int_{-\infty}^{\infty}\int_{-\infty}^{\infty} f(x,y) f(x+\Delta x, y+\Delta y) dxdy, \end{aligned} \tag{5.6}$$

for an infinite domain, where $C_f(\Delta x, \Delta y)$ stands for the autocorrelation function for the original function $f(x,y)$. In the case of dislocations and considering a finite domain, the ensemble average can be taken over the domain [143]:

$$C_\rho(\Delta x, \Delta y) = \left\langle \rho(x,y)\rho(x+\Delta x, y+\Delta y) \right\rangle, \tag{5.7}$$

where $\langle \cdot \rangle$ denotes the ensemble average, $\rho(x,y)$ represents the dislocation density distribution on the plane. It is to be noted that the autocorrelation calculation does not subtract the mean value from $\rho(x,y)$ in order to avoid the negative value in C_ρ. Although this is possible, it does not aid the detection of anisotropy of the original image.

Keeping in mind that the TEM images are obtained from a slice of the thickness up to 100 nm, the analysis of dislocation microstructures from numerical simulations should also be done on similar slices. Ideally speaking, a slice within the simulated cube should be first cut and relaxed first to take into consideration the free surface effects but this

effect is assumed to be minor. On the other hand, the current simulations suit better a comparison with dislocation pattern observation by x-ray diffraction technology [211].

The following procedures are conducted at the post-processing stage in the simulation to mimic the acquisition of TEM images in experiments. First of all, a slice of the thickness about 120 nm, which spans the distance of four grid points, are cut from the cube. Four sections, each of which is located on one mesh point in the direction of thickness, are taken to plot total dislocation density pattern on each of them. The ACF analysis is completed for the four respective images, yielding four correlation fields which are finally averaged to yield an average autocorrelation field, from which direction of dislocation walls within the slice is expected to be detected and quantified. The above process can be summarized mathematically by:

$$\bar{C}_{\rho}(\Delta x, \Delta y) = \sum_{i=1}^{4} C_{\rho_i(x,y)}(\Delta x, \Delta y), \tag{5.8}$$

where ρ_i is the scalar density function of total dislocations on the *i*-th section within a slice. The trace analysis can be processed based on the correlation information embodied in $\bar{C}_{\rho}(\Delta x, \Delta y)$.

The results of correlation analysis are shown in figures 5.16 , 5.17 and 5.18 for [001], [110], and [111] loading directions, respectively. The slices chosen from the simulations are all of {110}-type because the section of this type is parallel to the direction of cubic edges. The sections parallel to the cube edges are the same in shape and size, so it makes sense to average the values on these parallel sections. The images of ACFs all have twofold symmetry about the origin. The pair of perpendicular green lines in ACFs

denotes $\Delta x = 0$ and $\Delta y = 0$. Relevant crystallographic directions and planes are also tagged in these figures.

The dominant feature of $\bar{C}_\rho(\Delta x, \Delta y)$ in the case of [001] loading is the nearly circular central part with peak at the origin, see figure 5.16(b). The surrounding dark areas outside the circular central part and near the rim in figure 5.16(b) arise due to finite wavelength of the pattern and the periodic boundary condition used in the simulation [107] (edge effects), so they are not of concern. The circular shape of the central part of the ACF indicates that no obvious orientation preference is detected by the autocorrelation fields. The cell structure is thus near isotropic when the specimen is subjected to [001] loading, coinciding with the experimental results [76].

When the loading is applied along the [110] direction, the dislocation pattern on $(1\bar{1}0)$ slices shows orientation preference but, at small strains, such a preference cannot be quantitatively characterized until the ACF analysis is applied. More distinguishable images and measurable anisotropy are plotted in figure 5.17(b). The high-value area is elongated in two dominant directions which are tagged with solid blue lines. It can be argued, based on the explanation on the meaning of ACF that these two directions are approximately corresponding to the preferred directions of dislocation walls in simulations. In figure 5.17(b), the traces of {111} slip planes are also included and they are actually oriented in <121>-type directions. Then the task of trace analysis for dislocation patterns obtained in the simulation can be fulfilled by measuring the angles between {111} traces (represented by dashed red lines) and directions of dislocation

walls (regarded in the directions of solid blue lines). According to this method, it is found that the deviation angles are 2.8 and 4.9 degrees for the chosen slice.

Figure 5.18 shows the same representative images in the process of trace analysis but in [111] loading. Unlike in figure 5.17(b) where the averaged ACF shows two directions of dislocation walls, it is found that only one orientation seems to be the dominant direction of dislocation walls. The reason is that the two {111}-type slip planes, which are represented by dashed red lines in figure 5.18 (b), are not symmetric regarding the loading axis in terms of Schmid factors. The $(\bar{1}\bar{1}1)$ slip plane, being closer to the wall direction in figure 5.18(b), contains two slip directions, while the (111) slip plane accommodates no slip directions at all. Hence, the dislocation walls are mainly constituted by dislocations coming from slip planes containing active slip directions so that the walls are more inclined to active slip planes. The deviation angle between the wall and the trace is measured to be about 28 degrees from the ACF figure.

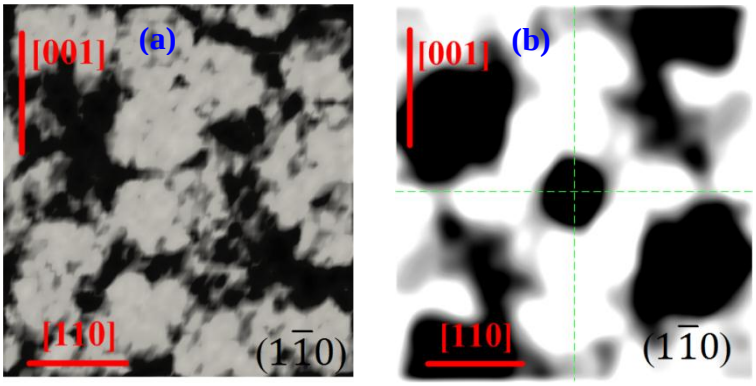

Figure 5.16. Dislocation density on one of the four sections within a $(1\bar{1}0)$ slice (a) and $\bar{C}_{\rho}(\Delta x, \Delta y)$ averaged over all four sections (b). The four sections are similar to each other in terms of dislocation density distribution, and so only one of them is displayed in part (a). The domain size is about 5μm and the analysis is done at a strain level of 1.5% for [001] loading axis.

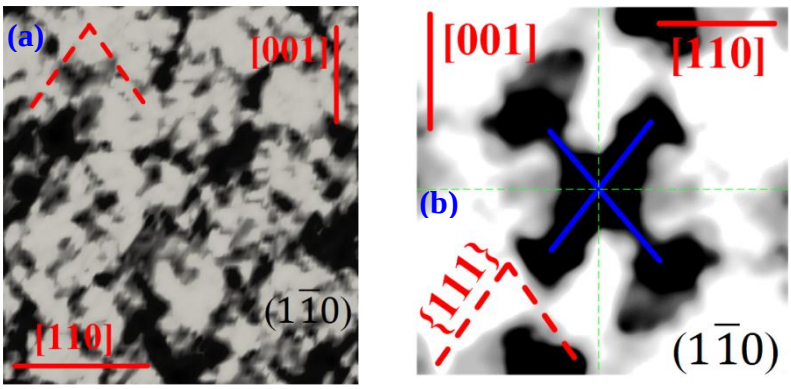

Figure 5.17. Dislocation density on one of the four sections within a $(1\bar{1}0)$ slice (a) and $\bar{C}_{\rho}(\Delta x, \Delta y)$ averaged over all four sections (b). Only one of images of four sections within a thin slice is displayed in part (a). The domain size is about 5μm and the analysis is done at a strain level of 1.5% for [110] loading axis.

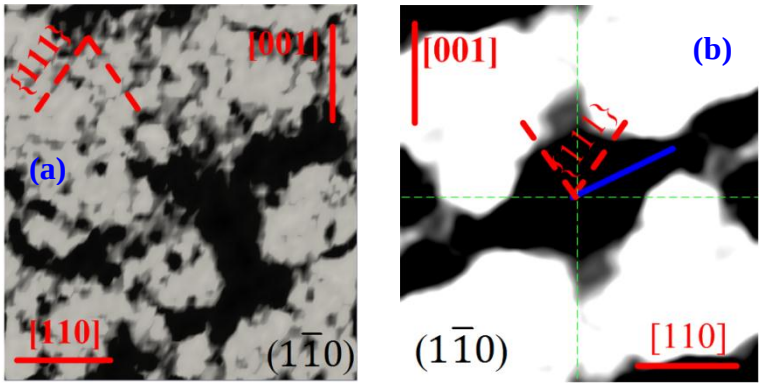

Figure 5.18. Dislocation density on one of the four sections within a $(1\bar{1}0)$ slice (a) and $\bar{C}_{\rho}(\Delta x, \Delta y)$ averaged over all four sections (b). (a) is representative of the four images averaged out and the others are similar in pattern. Two traces of {111} slip planes are represented by red dashed line. The domain size is about 5μm and the analysis is done at a strain level of 1.5% for [111] loading axis.

On the aspect of experiments, the deviation of dislocation boundaries from the slip plane was measured to be 3 degrees for the crystal is oriented for [541] [209] which is in vicinity to the simulated [110] loading. The ACF analysis applied to patterns in the simulation gives deviation angles between 2 to 5 degrees in [110] loading (simulation V). The simulated [111] loading was conducted by Kawasaki and co-workers [45] in laboratories. In their experiment, the deviation angle between dislocation boundaries and slip planes is measured to be 29 degrees, only 3.5% different from the simulation here. Reference [76] measured the deviation angle to be 2 °for type I structure and 25 °for type III structure, which correspond to [110] and [111] loading directions in the simulations, respectively.

In short, the above measurement of the deviation angle between dislocation wall and the trace of slip planes based on the detected direction on ACF images coincides with the

experiments to a large extent. The dislocation-dense areas can be either recognized by different types: geometrical necessary boundaries (GNBs), incidental dislocation boundaries (IDBs), microbands (MBs), dense dislocation walls (DDWs), etc., [49,212,213], or without distinction between such structures [214]. In the previous study by discrete dislocation dynamics [215], the latter approach is adopted. The analysis by ACF in the current process essentially belongs to the later also since the dislocation patterns shown on sections are total dislocation density. The reason for this lies in the different strain levels existing in numerical simulations and experiments. The strain level in current simulations is too small for the emergence of dislocation boundaries of different types.

CHAPTER 6. MODEL RESULTS: CYCLIC LOADING

The failure of metals by fatigue has important safety and economic consequences. When a material is subjected to the loads of cyclic nature, it fails at much lower stresses than would be required for failure in a tensile test [53]. A fatigue fracture always starts with a small crack which grows in length under repeated stresses. It is the movement of dislocations during cyclic loading that gives rise to the extrusion and intrusion that lead to the initiation of cracks [216]. Thus the prevention of fatigue failures cannot be accomplished quite well without a good understanding of dislocations kinetics under cyclic loading.

In this chapter, continuum dislocation dynamics is applied to fatigue simulations, with the objective of checking the model's ability to predict the characteristic patterns observed under fatigue loading in experiments. As a test problem, cyclic loading along [001] is imposed on the cube with the strain rate of 30/s and a prescribed plastic limitation of 0.15%. For the same reason as in the previous simulations, the cross-slip rate is first obtained from a discrete dislocation simulation. The results from continuum model are compared with those from discrete dislocation simulation as well as with those in experiments, with a focus on the dislocation density patterns from the continuum simulation.

6.1 Cross-slip Rates from Discrete Dislocation Dynamics

Discrete dislocation dynamics simulations were conducted for a specimen of the same size and subjected to the same loading condition as used in the continuum model. The microMegas code was used for this purpose. Time series analysis presented in chapter 4 is implemented so as to obtain $\bar{\dot{R}}^{l}_{\mathrm{cg}}(t)$ and $\delta\bar{\dot{R}}^{l}_{\mathrm{cg}}(t)$ in equation (4.9) when the cube is cyclically loaded. Once the smoothed time series, for example $\bar{\dot{R}}^{l}_{\mathrm{cg}}(t)$ is obtained, it is plotted against cumulative plastic strain $\varepsilon^{\mathrm{pl},n}_{\mathrm{cum}}$ which is obtained from the following equation:

$$\varepsilon^{\mathrm{pl},n}_{\mathrm{cum}} = \sum_{i=1}^{n} \left| \Delta\varepsilon^{\mathrm{pl},i} \right|, \tag{6.1}$$

where $\Delta\varepsilon^{\mathrm{pl},i}$ is the increment of plastic strain from time step $i-1$ to i, n denotes the n-th time step, $\varepsilon^{\mathrm{pl},n}_{\mathrm{cum}}$ the cumulative plastic strain. Due to the absolute value taken for $\Delta\varepsilon^{\mathrm{pl},i}$, which itself can be positive or negative depending on loading direction, $\varepsilon^{\mathrm{pl},n}_{\mathrm{cum}}$ always increases with time.

Cumulative plastic strain is chosen instead of time as a scale for cross-slip rate due to the need to synchronize the loading and unloading control in discrete and continuum simulations. It was found in the previous monotonic simulations that plastic strain is not synchronized in time for discrete and continuum simulations (see figure 5.10). It takes more time for the crystal to yield in continuum dynamics than in discrete dynamics given that the yielding stress is higher (about 2 times but on the same magnitude of the order) under the same strain rate. As a result, when it is time for the reverse loading to be

applied on the crystal in the discrete simulation, the plastic strain has not yet reached to the prescribed limit of plasticity. So if the cross-slip rate were implemented in terms of time rather than plasticity scale, the simulation by continuum dynamics would at some time during loading period take unloading cross-slip rates generated from discrete dynamics, which may lead to a less accurate result. However, the common employment of plastic strain amplitude in both discrete and continuum simulations enables the simulation in both cases to be synchronized by cumulative plastic strain. Furthermore, The cumulative plastic strain is also frequently used as a scale in fatigue and damage in experiments [217–219]. The task to replace time t in function $\bar{\dot{R}}^{l}_{\mathrm{cg}}(t)$ with $\varepsilon^{\mathrm{pl},n}_{\mathrm{cum}}$ is straightforward since $\varepsilon^{\mathrm{pl},n}_{\mathrm{cum}}$ according to equation (6.1) is a function of t.

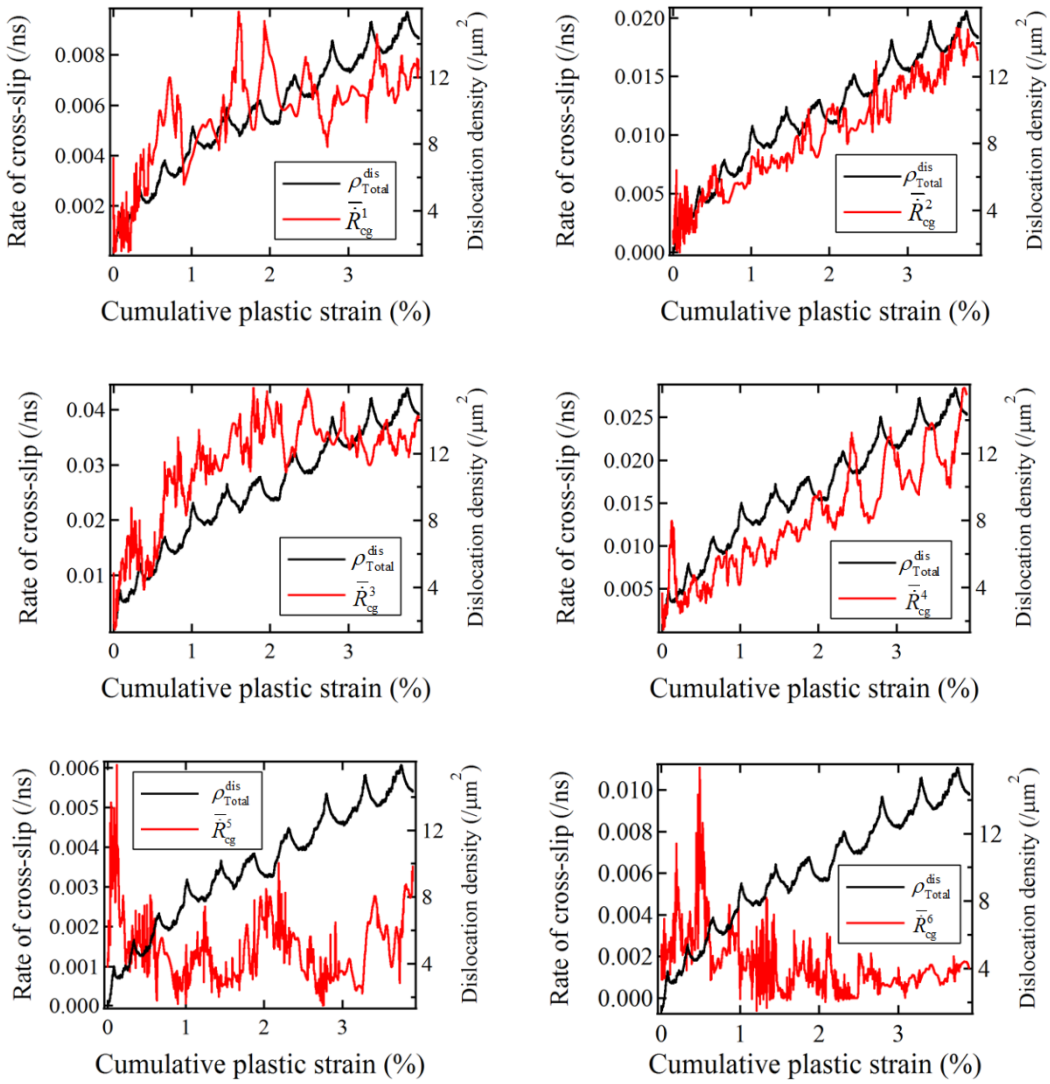

Figure 6.1. $\dot{\bar{R}}_{\text{cg}}^{l}(t)$, $(l=1,2,...,6)$ in fatigue test from discrete dislocation simulation. The total dislocation density is plotted together with each $\dot{\bar{R}}_{\text{cg}}^{l}(t)$ so as to identify cycles.

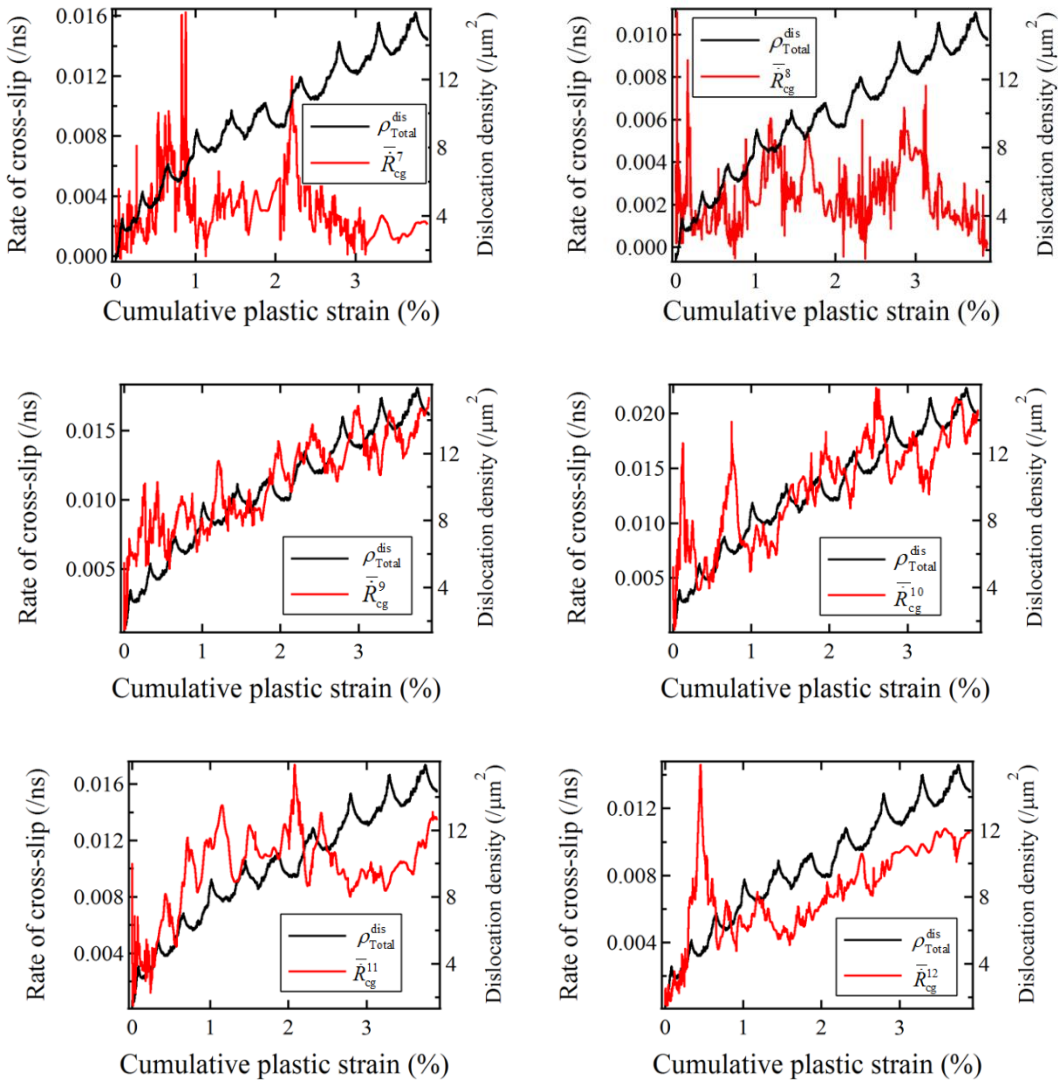

Figure 6.1. (continued) $\bar{\dot{R}}_{\text{cg}}^{l}(t)$, $(l = 7,8,...,12)$ in fatigue test from discrete dislocation simulation. The total dislocation density is plotted together with each $\bar{\dot{R}}_{\text{cg}}^{l}(t)$ so as to identify cycles.

The term $\bar{\dot{R}}_{\text{cg}}^{l}(t)$ after coarse-graining and smoothing, which represents the trend, is plotted in figure 6.1 for all 12 slip systems. Up to 5 cycles are finished by the simulation and the total dislocation density (the black curve in figure 6.1) increases in general but

with rises and declines in accordance with loading and unloading. The trend of cross-slip rates for active slip systems, which are 1, 2, 3, 4, 9, 10, 11 and 12, show increasing feature while only trivial wavy feature in $\bar{\dot{R}}^{l}_{\mathrm{cg}}(\varepsilon^{\mathrm{pl,n}}_{\mathrm{cum}})$ is associated with inactive slip systems, coinciding with previous observations for monotonic loading plotted in figure 4.6.

The cross-slip rates in some slip systems as 1, 3, and 11 show the saturation behaviour towards the end of simulation, while some seem to be still in increase at the end of 5 cycles. Slip system 2 even shows a cyclic behaviour in cross-slip rates with cumulative plastic strain, such is however not observed on the other slip systems. All these features demonstrate that the cross-slip is a complex behaviour even when viewed stochastically at a coarse-grained level. There might or might not be some universal laws that can relate cross-slip rate with time or plasticity, which is beyond the scope of current progress. In short, it is at least reasonable to incorporate the data (as plotted in figure 6.1) directly before any further summarization is made.

6.2 Fatigue Results by Continuum Dislocation Dynamics

The dislocation density and stress-plastic strain curves from continuum dislocation dynamics for fatigue are plotted in figure 6.2. Due to the limitation of data obtained from discrete dislocation simulation and the computing time, only about 5 cycles are finished by the continuum model. The typical shape of hysteresis loops is observed in the stress-strain curve shown in figure 6.2(a), where the material exhibits cyclic hardening, coinciding with experiments [43,44,47,94,96] and other simulations [128,129,220]. The flow stress level is higher than in experiment for the same reasons discussed in chapter 5.

The Bauschinger effect, which is commonly observed in experiments and in simulations [101,138,221], reveals itself in figure 6.2(a). For example, the first unloading takes place at about 70MPa while the yielding in the opposite direction happens around -50MPa, delivering a difference about 20% between both directions.

The cyclic hardening is most pronounced during first and second cycles but the continual increase in stress is moderate in later cycles (towards 5 cycles), indicating a saturation feature. The profile of the hysteresis loop is also changing, developing from a round shape to a sharp cornered shape and again into a round shape, coinciding qualitatively with the experiment [96].

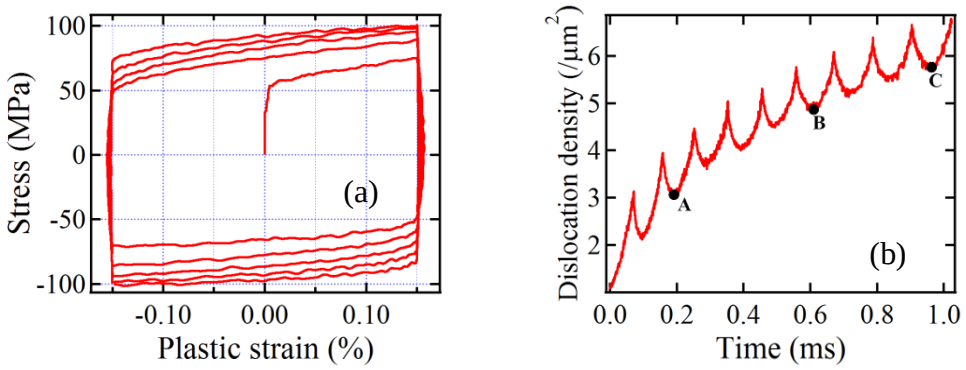

Figure 6.2. (a) dislocation density and (b) stress-strain curves obtained from continuum dislocation dynamics for fatigue simulation up to 5 cycles. The stress strain curve shows typical hysteresis loops with Bauschinger effect reflected. The dislocation density increases during the entire simulation in an oscillatory manner with the applied loads.

The dislocation density curve in figure 6.2(b) shows cyclically increasing feature: the density increases while the material is strained by tension or compression; it decreases while the material is relaxed by unloading. This feature coincides with the total

density curves plotted in figure 6.1 from discrete dislocation simulation, justifying the synchronization by using cumulative plastic strain for the incorporation of cross-slip rates. The average dislocation density increases pretty fast at first two cycles but slows down in the later cycles, also indicating the tendency towards a final saturation status, in correspondence with the stress-plastic strain behaviour.

It is often observed in experiments that fatigue gives rise to the patterning of dislocations within crystals, depending on many factors [219]. Since saturation status is seen to be close in the continuum simulation, dislocations might already form certain structures in this particular test. The next section is dedicated to the discussion of dislocation patterns during the cyclic loading simulated by the continuum model. For convenience, three sample points are tagged in figure 6.2(b) to denote the snapshot time.

6.3 Dislocation Density Pattern during Fatigue

Plenty of results have been obtained regarding dislocation patterns in FCC single crystals under cyclic loading during past years [46,48,51,88,92,94,96,222–224]. The saturated patterns in cyclic loading are dependent on plastic amplitude [89], orientation [88], and temperature [92]. The amplitude and orientation dependencies are of interest among all the factors, especially in context of the simulation presented here.

The orientation of crystal has its influence on the cyclic stress-strain curve which is first plotted by Mughrabi [96]. For single-slip-oriented copper single crystals, plateau period is observed during which the saturated hardening stress is not changed by increase in plastic amplitude. This period ranges approximately from 10^{-4} to 10^{-2} of plastic strain amplitude [96]. Before this period, veins are observed at low values of plastic strain

amplitude whereas the persistent slip bands are observed within the plateau stage because of their ability in accommodating more plastic deformation. The persistent slip bands are identified by their ladder-like arrangement of dislocations, see figure 1.2(a). Towards and after the end of plateau stage, other structures like labyrinth and cells are observed, depending on crystal orientation, which can be ascribed to the secondary slip [90].

The cyclic stress-strain curve changes its shape in plateau behaviour if the crystal is otherwise oriented such that multiple slip systems are activated from the beginning [225]. The dislocation patterns show its diversity with respect to different orientations also. The labyrinth structure is universally found in <001> crystals as shown in figure 2.9, where the walls are constituted of persistent slip bands [51]. Cell structure is often associated with <111> crystals and abundant persistent slip bands are prominent with <011> crystals [89].

The discrete dislocation models also achieve some of the results that are seen in those experiments [124,128,130,220,226]. However, a continuum model is seldom used for the fatigue simulation to produce dislocation patterns especially when it comes to 3-dimensional modelling. This section presents the dislocation patterns obtained from the continuum simulation of cyclic loading. At first, the pattern is displayed with scalar dislocation density on surfaces and sections of the cube. Further investigation into the dislocation structure is enabled by vector representation of dislocation density on individual slip systems, which is presented in section 6.3.2.

6.3.1 Scalar Dislocation Density Pattern

Viewed from the surface, the cube is exhibiting patterning during the fatigue process, as plotted in figure 6.3. Dislocations, which are represented by total dislocation density, are not forming cell structure even after about 5 cycles, unlike monotonic loading case, where the total dislocations form cell structure at pretty earlier stage of the simulation. Nevertheless, the inhomogeneity feature of dislocation structure is also preserved in the fatigue test.

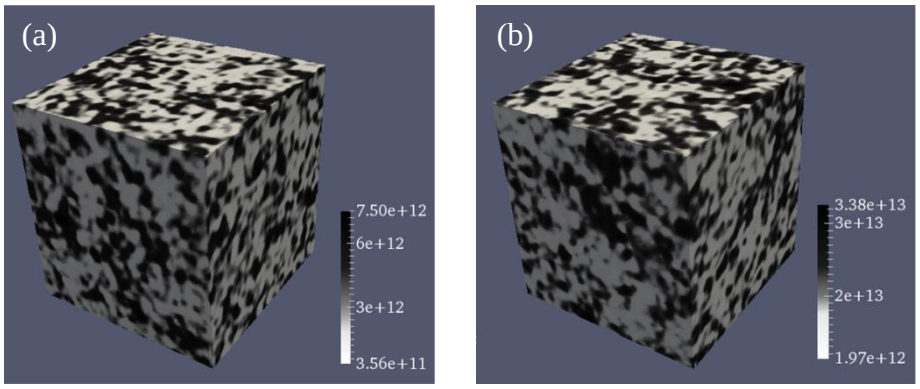

Figure 6.3. Dislocation density on the surface of the cube at (a) point A (the end of the first cycle) and (b) point C (within the 5-th cycle). No prominent cell features are observed through the cyclic loading simulation.

Although the total dislocation density does not show well-formed structure on the surface, the model can be employed further to display partial dislocation density, which is the dislocation density on one slip system, on a slip plane. The scalar dislocation density on an individual slip system at a point reads:

$$\|\rho_l\| = \sqrt{(\rho_{l,1})^2 + (\rho_{l,2})^2 + (\rho_{l,3})^2}\,, \tag{6.2}$$

where $\|\rho_l\|$ is the scalar of the vector $\boldsymbol{\rho}_l$. The quantity $\|\rho_l\|$ is plotted on one section from (111) slip plane in figure 6.4 at different strain levels, where l is chosen to be $(111)[01\bar{1}]$ slip system, one of the active slip direction on that plane. It is clearly seen that the partial density $\|\rho_l\|$ on a slip plane gradually organizes into the clear vein structure which is constituted of dislocation walls along the direction perpendicular to the Burgers vector direction (namely, $[\bar{2}11]$). Furthermore, the vein structure is seen refining itself by decreasing the distance between the walls in the same sense as in the refinement of cell structure in the monotonic loading case. The decrease in the distance between dislocation walls provides less free space for dislocations to glide on the slip plane and thus causes cyclic hardening [227].

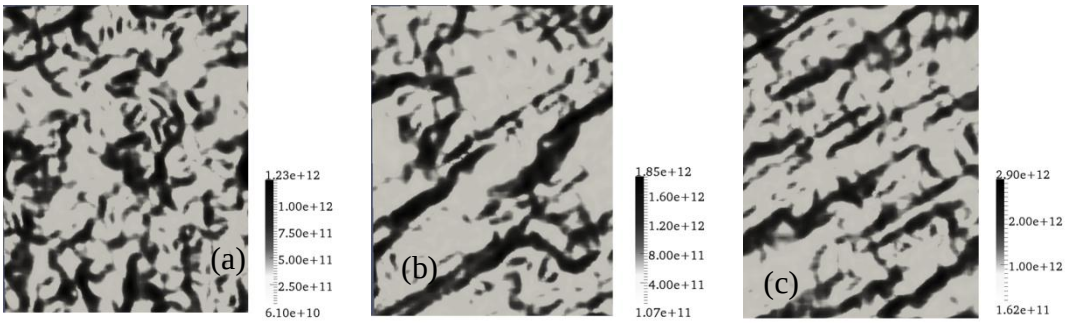

Figure 6.4. Partial dislocation density on a slip plane at (a) point A (the end of the first cycle) (b) point B (the end of the third cycle), and (c) point C (within the 5-th cycle).

The vein structure shown in the above simulation results on (111) slice has been typically observed in experiments [47,88,222] for years. Figure 6.5 shows a clear vein

structure on (111) slip plane in the $[\bar{1}17]$ copper single crystal (a) and single-slip oriented copper single crystal (b), the tensile direction of the former of which is close to [001] direction used in the current simulation. The qualitative similarity can be immediately seen when one compares figure 6.5 with figure 6.4(b) and (c).

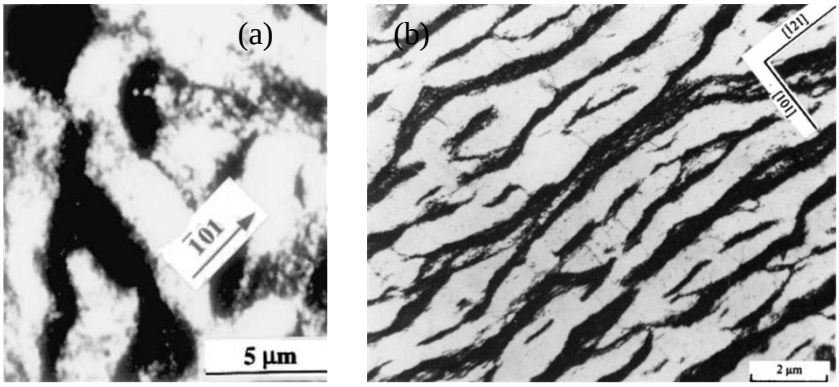

Figure 6.5. (a) Experimental dislocation structure on (111) foil after saturation of the cyclic loading along $[\bar{1}17]$ axis, adopted from [88]. (b) Vein structure on $(\bar{1}\bar{1}1)$ plane in a copper single crystal oriented for single slip, adopted from [91].

6.3.2 Composition of Vein Structure

It is commonly regarded by experimentalists [216] and modellers [171] that the vein structure is mainly composed of edge dipolar walls with screw dislocations gliding between them. The reason for this is that the dipolar walls are stable under stress of opposite signs in cyclic loading [14]. Figure 6.6 schematically illustrates the arrangements of dislocations in different organizations of vein structures. Two typical structures are observed in TEM micrograph for fatigued crystals: the matrix structure and

persistent slip bands [91]. The matrix structure is characterized by an irregular arrangement of veins, which is plotted in figure 6.6(a). The persistent slip bands, on the other hand, appear in a form of regular ladder-like structure oriented along the primary Burgers vector, which is plotted in figure 6.6(b). In experiments, the persistent slip bands are often seen being embedded in the surrounding vein structure [47,223]. What figure 6.6(c) shows is a schematic illustration of idealized slab-matrix structure in which the matrix experiences homogeneous deformation while the slabs do not deform [228]. Such a structure accommodates long range rotation between successive matrix areas which can be attributed to plastic strain incompatibility. The common feature existing in the veins, walls and slabs is the edge dipoles which may evolve into different structure depending on situations (loading directions, magnitude of plastic deformation, slip planes, etc.)

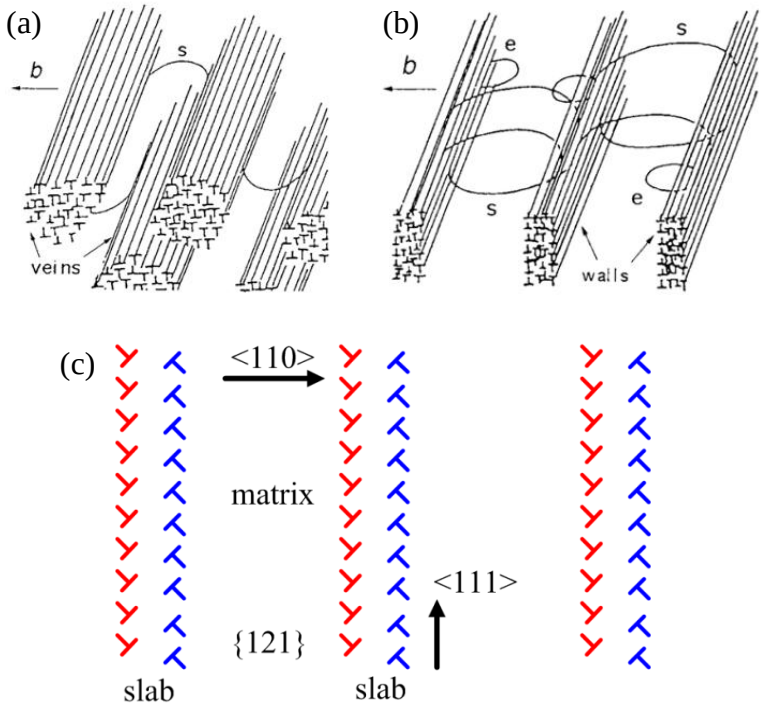

Figure 6.6. Theoretical models of vein structure appearing in fatigued fcc single crystals: (a) and (b) shows dislocation arrangements in matrix and persistent slip band structure respectively, adopted from [14]. (c) shows the slab-matrix model, reproduced from [228].

The scenario in the continuum simulation can be examined by checking the component of dislocations in the vein-like structure plotted in figure 6.4. The edge component of dislocations is extracted by applying a dot product to dislocation density vector with edge dislocation line sense:

$$\rho_{\text{edge}} = \rho_l \cdot \xi_{\text{edge}}, \tag{6.3}$$

where $\boldsymbol{\rho}_l$ stands for dislocation density vector of slip system l, ξ_{edge} the line sense of pure edge dislocation of Burgers vector $[01\bar{1}]$ on slip plane (111). The edge component

can be positive or negative, indicating edges of different signs. In a sense, the dislocation density vector is filtered out to produce an edge component.

In figure 6.7(a), a (111) slice of the thickness of 130 nm is chosen from the cube at sample point C with partial dislocation density plotted on the surface of it. The dislocations on (111) plane are aligned in the direction of $[\bar{2}11]$, being parallel with pure edge direction on that plane. On two vertical planes to (111), namely $(\bar{2}11)$ and $(1\bar{1}0)$, dislocations are concentrated in dense areas in dark dots. Figure 6.7(b) plots the edge component by the application of equation (6.3) on the same slice as in figure 6.7(a). Several features of veins can be revealed by the plotting of edge components. First of all, the dislocation dense area on (111) plane is mainly composed of edge dislocations. The whole dislocation density tends to be smaller in magnitude at the place where the edge density is lower. The edges are alternating in their signs violently from positive to negative signs within one straight vein, which is more prominent on $(\bar{2}11)$ plane where the cross sections of veins are seen. This means that the dislocation veins are composed of edge dislocation dipoles which include opposite edges in sign.

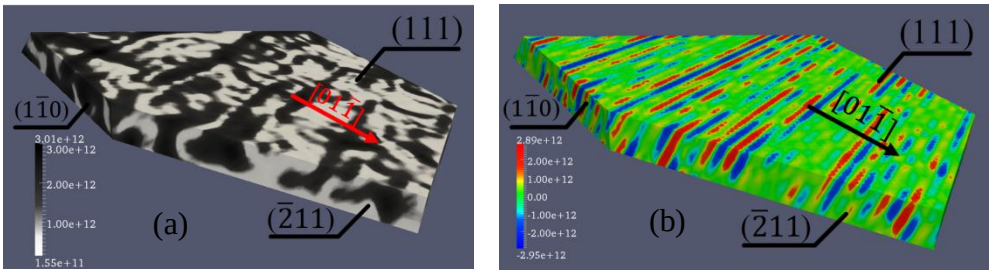

Figure 6.7. (a) The vein structure viewed from a (111) slice with the thickness of 130 nm at sample point C. (b) the edge component of veins on the surface of the same slice.

Partly due to the resolution limitation, the continuum model implemented here cannot exactly present the detailed dipoles in which edges are in shorter distance to each other than the resolution of the mesh (~30 nm). Ideally speaking, the resolution should be on the magnitude of Burgers vector since the annihilation distance between edges is quite small (~1.6 nm) [188], which is not practical. However, future extension of the model will allow the presence of multiple orientations at a given point in space. The continuum model with oversized resolution must induce some numerical smearing effect regarding edge dislocations. Nevertheless, the present model characterizes the constituents of veins correctly in a qualitative sense.

It must be kept in mind that from the experimental literatures discussed at the beginning of this chapter, the <001> crystal demonstrates labyrinth structure in dislocations. However, vein structure shown in the continuum simulation mimics more the single slip situation in experiments. The main reason for the failure of dislocations to reach a labyrinth structure in simulation can be again attributed to the insufficient number of cycles (in experiments, observations are often made up to tens of thousands of cycles). It is proposed that the labyrinth structure arises from a critical type of short-range reactions occurring among edges from different slip systems [95]:

$$\begin{matrix} \frac{1}{2}[\bar{1}01]+\frac{1}{2}[101]=[001] \\ \frac{1}{2}[10\bar{1}]+\frac{1}{2}[101]=[100] \end{matrix}, \qquad (6.4)$$

which leads to formation of new slip systems of the type {100}<001>. The intersection between dislocations on the new born slip systems with {010} type plane forms the

eventual labyrinth structure. In the current model, however, short-range reactions other than annihilation are not yet considered. This renders the dislocations described in the continuum model at the current status more influenced by the long range stress effects. Indeed, previous explanations, e.g., in figure 6.6(c), emphasize more the long range effects in fatigue pattern formation.

CHAPTER 7. SUMMARY AND OUTLOOK

Dislocations are critical in studying the deformation mechanism of metals [229]. However, their collective behaviour still poses a great theoretical challenge. The complexity of dislocation systems arises from their one-dimensional nature, long range effects, and the multitude of crystallographic processes they undergo, e.g., cross slip and short range reactions. The fact that they are one-dimensional objects, although straight forward to handle, posed for a long time a mathematical challenge to modellers trying to study their collective behaviour – in classical literature, only particle systems are well modelled. The long range feature of stress field also contributes to the difficulty especially for discrete simulation where the cut off radius should ideally be the entire domain. This nature of the dislocation systems made it hard to tackle practical deformation problems in bulk plasticity using discrete dislocation dynamics. This aspect is exacerbated by various short range reactions. Finally, the multiplication of dislocation density during hardening adds difficulty to discrete simulation because of the $O(N^2)$ increase in computational burden.

Various continuum dislocation dynamics models were developed as a way to avoid these difficulties. The current model is one that gave results closer to experiments for the first time. By representing dislocations as vector fields, the continuum model captures the position and orientation information of dislocations. Although the model does not yet

permit the presence of multiple line directions at a continuum point in space [72,159], a practical solution to circumvent the consequences by controlling the mesh size to be on the magnitude of annihilation distance proved to be a satisfactory initial step. In any case, the merit of describing dislocations as physical fields is that it enabled the continuum model to predict the deformation behaviour of crystals, including all mechanical field and dislocation patterns solutions, in a reasonable time and to higher strain values than achieved in discrete simulations. The future extension to finite deformation is straightforward, which is inconceivable for discrete dislocation dynamics.

Unlike in the discrete model, where the short range reactions are implemented by referring to Frank's energy criterion, dislocations repulsion and attraction as dictated by the stress field can take care of all short range reactions. Indeed, annihilation is taken care of in the current model and future extension will take into consideration the formation of glissile junctions. Cross-slip of screw dislocations, a thermally activated process, is handled by incorporating the data from a corresponding discrete dislocation simulation using a time series procedure for temporal coarse graining. This connection with discrete dislocation dynamics models should be viewed as a different method from the hybrid model proposed by Zbib and co-workers [175] because the former only takes parameters from discrete simulation while Zbib's multiscale model utilizes discrete simulation to evolve the dislocation systems within a crystal plasticity framework.

The implementation of continuum model is supported by a robust staggered numerical scheme that couples the kinetics of dislocations and stress field solution. The stress field is solved by Galerkin's finite element method which is well known for its accuracy in elliptical equations, the case with equilibrium equations [230]. The kinetic

equations are solved by Least Square Finite Element Method which is shown to be reliable for hyperbolic equations [186]. The superlattice meshing proposed here to reproduce all slip planes of an FCC crystal and accurately capture the 2D motion of dislocations proved to be a critical part of the solution scheme. The integration scheme of the hyperbolic transport equations, although suffers slight diffusion, was found to be robust against dispersion. The reason is that, unlike the case of scalar functions, the density vector and the velocity vector are coupled which leads to smoothing any fluctuations in the wake of propagating density profiles.

The continuum model shows promising results in an array of 3D simulations. The stress-strain and dislocation density evolution curves are in qualitative agreement with experiments and other discrete dislocation dynamics simulations. It is observed for the first time in any simulation, at least using continuum dislocation dynamics models, that dislocations are organizing into clear cell patterns under monotonic loading of [001] type. Prediction of this kind of self-organization of dislocations has been the number 1 reason dislocation dynamics simulations was pursued for the first time in the mid-1980s. It took almost 30 years of research to achieve that goal, thanks to the progress made on continuum modelling side dislocations.

It is also found that cross-slip serves as a mechanism for triggering the formation of cell structure: the larger the cross-slip rate is in the simulations, the earlier and sharper the cell structure. It is also discovered that the utilization of realistic data from discrete simulation improves the model to make it closer to discrete simulation results, the only available results for benchmarking at small strains. The similitude law is checked with various conditions regarding cross-slip rates and the number of simulated slip systems,

yielding a nearly universal curve for all cases [001] cases simulated. This finding not reveals the mechanism underlying strain hardening of fcc single crystal but also shows that these mechanisms are well represented in the model. The simulations also exposed the orientation dependence of both the hardening rate and dislocation patterns. No anisotropy is found in [001] crystal due to its symmetry with respect of slip systems whereas pronounced orientation preference of dislocation dense areas is observed in [111] and [110] crystals. The results are all compared with experiments which show similarity but, again, at much larger strain level. It is thus not unreasonable to make the argument here that the patterning of dislocations at small strain level paves the way for forming the lamellar structures observed at large strains for loading orientations different from [001].

The fatigue test has also been run to test the continuum model by simulating plastic strain controlled cycles of load reversals. Although the number of cycles is limited due to computational issues to only several, dislocations were found to arrange into vein structure on respective slip systems and the veins are examined constituted of edge dipoles, in agreement with experiments and theoretical models.

All the test examples not only affirm the validity of the continuum model presented here but also provide original discoveries of mechanisms and detailed structures which are not observable in experiments. This, however, should not be seen as a final point in the exploration of continuum dislocation dynamics modelling, but rather as an initial development of this approach. Actually, as this dissertation is being developed, new continuum models are seen to be proposed [231].

The current continuum model still has resolution issue in mesh size especially towards edge dislocations which possess a smaller annihilation distance. This

disadvantage is perhaps one of the reasons a labyrinth structure for [001] fatigued crystal was not observed, where reactions between edge components are important. Other reactions (e.g. glissile reactions) are also lacking which affects the accuracy of predictions to some extent. Further development of the model should be based on either the decrease in mesh size at the cost of computation or the capture of short range reaction by change in equations somehow.

The model improvement with regard to cross slip by incorporating data from discrete dislocation dynamics is an advantage, because it seems as redundancy also: the simulation should be conducted twice for one example, one by discrete and another one by continuum. This is not true, however, since the purpose of running discrete simulations is to learn the statistical representation of cross slip at the continuum scales. This learning process will continue in the future until we are able to develop models in that respect.

As a final remark, future extension of the model to accommodate finite deformation is a must in order to simulate levels of deformation encountered in experiments and in metal processing.

REFERENCES

REFERENCES

[1] H. C. H. Carpenter, C.F. Elam, Proc. R. Soc. A 100 (1921) 329.

[2] G.I. Taylor, C.F. Elam, Proc. R. Soc. A 102 (1923) 643.

[3] C.F. Elam, Proc. R. Soc. A 112 (1926) 289.

[4] G.I. Taylor, W.S. Farren, Proc. R. Soc. A 111 (1926) 529.

[5] G.I. Taylor, Proc. R. Soc. A 116 (1927) 16.

[6] G.I. Taylor, Proc. R. Soc. London 145 (1934) 362–387.

[7] M. Polanyi, Zeitschrift Für Phys. 89 (1934) 660–664.

[8] E. Orowan, Zeitschrift Für Phys. 89 (1934) 605–613.

[9] E. Orowan, Zeitschrift Für Phys. 89 (1934) 614–633.

[10] E. Orowan, Zeitschrift Für Phys. 89 (1934) 634–659.

[11] V. Gerold, in:, F.R.N. Nabarro (Ed.), Dislocations in Solids, North-Holland Publishing Company, 1979, p. 219.

[12] P. Haasen, in:, F.R.N. Nabarro (Ed.), Dislocations in Solids, North-Holland Publishing Company, 1979, p. 155.

[13] H. Suzuki, in:, F.R.N. Nabarro (Ed.), Dislocations in Solids, North-Holland Publishing Company, 1979, p. 191.

[14] L.P. Kubin, C. Fressengeas, G. Ananthakrishna, in:, F.N.R. Nabarro, M.S. Duesbery (Eds.), Dislocations in Solids, Elsevier Science, 2002, p. 101.

[15] J.P. Hirth, J. Lothe, Theory of Dislocations, Second, John Wiley & Sons, Inc., New York, 1982.

[16] Kosevich, in:, F.R.N. Nabarro (Ed.), Dislocations in Solids, North-Holland Publishing, 1979, p. 350.

[17] S. Amelinckx, in:, F.R.N. Nabarro (Ed.), Dislocations in Solids, North-Holland Publishing, 1979, p. 66.

[18] W.D. Callister, Materials Science and Engineering, Seventh, John Wiley & Sons, Inc., New York, 2007.

[19] E. Orowan, Nature 147 (1941) 452–453.

[20] J. Dejace, D. Nobili, J. Mater. Sci. 4 (1969) 61–64.

[21] B.F. Boyce, J. T. Vreeland, Mater. Sci. Eng. 9 (1972) 56–57.

[22] P. Zielinski, D. Ast, Philos. Mag. A 48 (1983) 811–824.

[23] M. Peach, J.S. Koehler, Phsical Rev. 80 (1950) 436–439.

[24] V. Volterra, Ann. Sci. l'École Norm. Supérieure, Sér 3 (1907) 401–517.

[25] Rudolf Peierls, Proc. R. Soc. London 52 (1940) 34–37.

[26] F.R.N. Nabarro, Proc. Phys. Soc. 59 (1947) 256–S72.

[27] L.P. Kubin, Dislocations, Mesoscale Simulations and Plastic Flow, Oxford University Press, Oxford, 2013.

[28] D. Hull, D.J. Bacon, Introduction to Dislocations, 5th ed., Butterworth-Heinemann, 2011.

[29] W.M. Lomer, Philos. Mag. 42 (1951) 1327–1331.

[30] A.H. Cottrell, Philos. Mag. 43 (1952) 645–647.

[31] T. Jøssang, J.P. Hirth, C.S. Hartley, J. Appl. Phys. 36 (1965) 2400.

[32] J.P. Hirth, J. Appl. Phys. 32 (1961) 700.

[33] R. Madec, B. Devincre, L. Kubin, T. Hoc, D. Rodney, Science (80-.). 301 (2003) 1879–1882.

[34] D. Weygand, P. Gumbsch, Mater. Sci. Eng. A 400-401 (2005) 158–161.

[35] B. Devincre, L. Kubin, T. Hoc, Scr. Mater. 54 (2006) 741–746.

[36] L. Kubin, B. Devincre, T. Hoc, Acta Mater. 56 (2008) 6040–6049.

[37] D. Weygand, Mater. Res. Soc. Symp. Proc. 1651 (2014).

[38] G. Saada, Acta Mater. 8 (1960) 841–847.

[39] Z.S. Basinski, Scr. Metall. 8 (1974) 1301–1308.

[40] R. Madec, B. Devincre, L. Kubin, Phys. Rev. Lett. 89 (2002) 255508.

[41] P.B. Hirsch, R.W. Horne, M.J. Whelan, Philos. Mag. 86 (1956) 4553–4572.

[42] E. Laufer, Czechoslov. J. Phys. 19 (1969) 333–334.

[43] T.H. Youssef, Phys. Status Solidi 3 (1970) 801–810.

[44] N.Y. Jin, A.T. Winter, Philos. Mag. Lett. 32 (1984) 1173–1176.

[45] Y. Kawasaki, T. Takeuchi, Scr. Metall. 14 (1980) 183–188.

[46] H. Mughrabi, Acta Metall. 31 (1983) 1367–1379.

[47] C. Laird, Z. Wang, B.-T. Ma, H.-F. Chai, Mater. Sci. Eng. A 113 (1986) 245–257.

[48] N. Hansen, D. Kuhlmann-Wilsdorf, Mater. Sci. Eng. 81 (1986) 141–161.

[49] N. Hansen, D.A. Hughes, Phys. Status Solidi 149 (1995) 155–172.

[50] T. Tabata, H. Fujita, M.-A. Hiraoka, K. Onishi, Philos. Mag. A 47 (1983) 841–857.

[51] A.T. Winter, O.B. Pedersen, K. V. Rasmussen, Acta Metall. 29 (1981) 735–748.

[52] A. Luft, Prog. Mater. Sci. 35 (1991) 97–204.

[53] R. Abbaschian, L. Abbaschian, R.E. Reed-Hill, Physical Metallurgy Principles, Cengage Learning, Independence, KY, 2008.

[54] R.D. Doherty, D.A. Hughes, F.J. Humphreys, J.J. Jonas, D. Juul Jensen, M.E. Kassner, W.E. King, T.R. McNelley, H.J. McQueen, A.D. Rollett, Mater. Sci. Eng. A 238 (1997) 219–274.

[55] F.J. Humphreys, M. Hatherly, Recrystallization and Related Annealing Phenomena, 2nd ed., Pergamon, Oxford, 2004.

[56] P.J. Jackson, Prog. Mater. Sci. 29 (1985) 139–175.

[57] B. Bay, N. Hansen, D.A. Hughes, D. Kuhlmann-Wilsdorf, Acta Metall. Mater. 40 (1992) 205–219.

[58] U.F. Kocks, H. Mecking, Prog. Mater. Sci. 48 (2003) 171–273.

[59] B. Jakobsen, In-Situ Studies of Bulk Deformation Structures : Static Properties under Load and Dynamics during Deformation, Roskilde University, 2006.

[60] J. Chakarabarty, Theory of Plasticity, Butterworth-Heinemann, Burlington,MA, 2006.

[61] R. Hill, J. Mech. Phys. Solids 14 (1966) 95–102.

[62] R.J. Asaro, J.R. Rice, J. Mech. Phys. Solids 25 (1977) 309–338.

[63] R.J. Asaro, J. Appl. Mech. 50 (1983) 921–934.

[64] B. Devincre, L.P. Kubin, Mater. Sci. Eng. A234-236 (1997) 8–14.

[65] H.D. Espinosa, M. Panico, S. Berbenni, K.W. Schwarz, Int. J. Plast. 22 (2006) 2091–2117.

[66] A.A. Benzerga, J. Mech. Phys. Solids 57 (2009) 1459–1469.

[67] C. Zhou, S.B. Biner, R. LeSar, Acta Mater. 58 (2010) 1565–1577.

[68] D. Walgraef, E.C. Aifantis, Int. J. Eng. Sci. 23 (1985) 1351–1358.

[69] A. Acharya, J. Mech. Phys. Solids 49 (2001) 761–784.

[70] S. Limkumnerd, J. Sethna, J. Mech. Phys. Solids 56 (2008) 1450–1459.

[71] M. Zaiser, T. Hochrainer, Scr. Mater. 54 (2006) 717–721.

[72] A. El-Azab, Phys. Rev. B 61 (2000) 11956–11966.

[73] M. Koslowski, M. Ortiz, Model. Simul. Mater. Sci. Eng. 12 (2004) 1087–1097.

[74] X. Huang, N. Hansen, Scr. Mater. 37 (1997) 1–7.

[75] X. Huang, Scr. Mater. 38 (1998) 1697–1703.

[76] X. Huang, G. Winther, Philos. Mag. 87 (2007) 5189–5214.

[77] P. Hähner, K. Bay, M. Zaiser, Phys. Rev. Lett. (1998) 1–4.

[78] P. Hahner, M. Zaiser, Mater. Sci. Eng. 272 (1999) 443–454.

[79] C.S. P. Ambrosi, E. Göttler, Scr. Metall. 8 (1974) 1093–1098.

[80] C. Schwink, Scr. Metall. 27 (1992) 963–968.

[81] M.R. Staker, D.L. Holt, Acta Metall. 20 (1972) 569–579.

[82] S. V. Raj, G.M. Pharr, Mater. Sci. Eng. 81 (1986) 217–237.

[83] R. Neuhaus, P. Buchhagen, C. Schwink, Scr. Metall. 23 (1989) 779–784.

[84] R. Neuhaust, C. Schwink, Philos. Mag. A 65 (1992) 1463–1484.

[85] A.S. Argon, Strengthening Mechanisms in Crystal Plasticity, Oxford University Press, Oxford, 2008.

[86] M. Zaiser, A. Seeger, in:, F.R.N. Nabarro, M.S. Duesbery (Eds.), Dislocations in Solids, North-Holland, Amsterdam, 2002, pp. 1–100.

[87] M. Zaiser, Adv. Phys. 55 (2006) 185–245.

[88]X.W. Li, Y. Umakoshi, B. Gong, S.X. Li, Z.G. Wang, Mater. Sci. Eng. A 333 (2002) 51–59.

[89] P. Li, S.X. Li, Z.G. Wang, Z.F. Zhang, Prog. Mater. Sci. 56 (2011) 328–377.

[90] F. Ackermann, L.P. Kubin, J. Lepinoux, H. Mughrabi, Acta Metall. 32 (1984) 715–725.

[91] S. Suresh, Fatigue of Materials, 2nd ed., Cambridge University Press, Cambridge, 1998.

[92] Z.S. Basinski, A.S. Korbel, S.J. Basinski, Acta Metall. 28 (1980) 191–207.

[93] J. Ahmed, A.J. Wilkinson, S.G. Roberts, Philos. Mag. Lett. 76 (1997) 237–246.

[94] B. Gong, Z. Wang, Z. Wang, Acta Mater. 45 (1997) 1365–1377.

[95] P. Li, S.X. Li, Z.G. Wang, Z.F. Zhang, Acta Mater. 58 (2010) 3281–3294.

[96] H. Mughrabi, Mater. Sci. Eng. 33 (1978) 207–223.

[97] R.J. Amodeo, N.M. Ghoniem, Phys. Rev. B 41 (1990) 6958–6967.

[98] E. Van der Giessen, A. Needleman, Model. Simul. Mater. Sci. Eng. 3 (1995) 689–735.

[99] D. Gómez-García, B. Devincre, L. Kubin, Phys. Rev. Lett. 96 (2006) 125503.

[100] A.A. Benzerga, Y. Bréchet, A. Needleman, E. Van Der Giessen, Model. Simul. Mater. Sci. Eng. 12 (2004) 557–559.

[101] C. Hou, Z. Li, M. Huang, C. Ouyang, Acta Mater. 56 (2008) 1435–1446.

[102] D. Tanguy, D. Delafosse, Philos. Mag. 90 (2010) 1415–1434.

[103] L.P. Kubin, Y. Estrin, G. Canova, in:, D. Walgraef, N.M. Ghoniem (Eds.), Patterns, Defects Mater. Instab., NATO ASI series, Kluwer, 1990, p. 277.

[104] B. Devincre, R. Madec, G. Monnet, S. Queyreau, R. Gatti, L. Kubin, in:, O. Thomas, A. Ponchet, S. Forest (Eds.), Mech. Nano-Objects, Presses des Mines, Paris, 2011, pp. 81–100.

[105] L.P. Kubin, G. Canova, M. Condat, B. Devincre, V. Pontikis, Y. Bréchet, Solid State Phenom. 23 (1992) 455–472.

[106] B. Devincre, M. Condat, Acta Metall. Mater. 40 (1992) 2629–2637.

[107] J. Deng, A. El-Azab, Model. Simul. Mater. Sci. Eng. 17 (2009) 075010.

[108] S. Queyreau, G. Monnet, B. Devincre, Acta Mater. 58 (2010) 5586–5595.

[109] B. Devincre, L. Kubin, Comptes Rendus Phys. 11 (2010) 274–284.

[110] C.Z. Zhou, R. Lesar, Comput. Mater. Sci. 54 (2012) 350–355.

[111] A. Vattré, B. Devincre, F. Feyel, R. Gatti, S. Groh, O. Jamond, A. Roos, J. Mech. Phys. Solids 63 (2014) 491–505.

[112] J.P. Hirth, M. Rhee, H.M. Zbib, J. Comput. Mater. Des. 3 (1996) 164–166.

[113] M. Rhee, H.M. Zbib, J.P. Hirth, H. Huang, T. Rubia, Model. Smulation Mater. Sci. Eng. 6 (1998) 467–492.

[114] A. Arsenlis, W. Cai, M. Tang, M. Rhee, T. Oppelstrup, G. Hommes, T.G. Pierce, V. V Bulatov, Model. Simul. Mater. Sci. Eng. 15 (2007) 553–595.

[115] V. V. Bulatov, W. Cai, Computer Simulations of Dislocations, Oxford University Press, New York, 2006.

[116] W. Cai, V. V. Bulatov, Mater. Sci. Eng. A 387-389 (2004) 277–281.

[117] A. El-Azab, J. Deng, M. Tang, Philos. Mag. 87 (2007) 1201–1223.

[118] C.R. Weinberger, W. Cai, J. Mech. Phys. Solids 58 (2010) 1011–1025.

[119] A.M. Hussein, S.I. Rao, M.D. Uchic, D.M. Dimiduk, J. a. El-Awady, Acta Mater. 85 (2015) 180–190.

[120] N. Ghoniem, L. Sun, Phys. Rev. B 60 (1999) 128–140.

[121] Z. Wang, N. Ghoniem, S. Swaminarayan, R. LeSar, J. Comput. Phys. 219 (2006) 608–621.

[122] G. Canova, L. Kubin, in:, G.A. Maugin (Ed.), Contin. Model. Discret. Syst., Longman Scientific and Technical, Harlow, UK, 1991.

[123] C. Ouyang, Z. Li, M. Huang, L. Hu, C. Hou, Mater. Sci. Eng. A 526 (2009) 235–243.

[124] M.C. Fivel, C.F. Robertson, G.R. Canova, L. Boulanger, Acta Mater. 46 (1998) 6183–6194.

[125] C. Motz, D. Weygand, J. Senger, P. Gumbsch, Acta Mater. 56 (2008) 1942–1955.

[126] N. Ahmed, A. Hartmaier, J. Mech. Phys. Solids 58 (2010) 2054–2064.

[127] C.Z. Zhou, R. Lesar, Int. J. Plast. 30-31 (2012) 185–201.

[128] C. Déprés, C.F. Robertson, M.C. Fivel, Philos. Mag. 84 (2004) 2257–2275.

[129] C. Déprés, C.F. Robertson, M. Fivel, S. Degallaix, Mater. Sci. Forum 482 (2005) 163–166.

[130] C. Déprés, C.F. Robertson, M.C. Fivel, Philos. Mag. 86 (2006) 79–97.

[131] F.F. Csikor, C. Motz, D. Weygand, M. Zaiser, Z. Stefano, Science (80-.). 318 (2007) 251–254.

[132] B. Devincre, T. Hoc, L. Kubin, Science (80-.). 320 (2008) 1745–8.

[133] L.P. Kubin, G. Canova, M. Condat, B. Devincre, V. Pontikis, Y. Bréchet, Solid State Phenom. 23-24 (1992) 455–472.

[134] J.F. Nye, Acta Metall. 1 (1953) 153–162.

[135] E. Kröner, Kontinuumscheorie Der Versetzungen Und Eigenspannungen, Springer, Berlin, 1958.

[136] K. Kondo, in:, 2nd Japan Natl. Congr. Appl. Mech., 1952, pp. 41–47.

[137] B.A. Bilby, R. Bullough, E. Smith, Proc. R. Soc. A 231 (1955) 263–273.

[138] A. Roy, A. Acharya, J. Mech. Phys. Solids 54 (2006) 1711–1743.

[139] A. Acharya, A. Roy, J. Mech. Phys. Solids 54 (2006) 1687–1710.

[140] E. Kroner, Arch. Ration. Mech. Anal. 4 (1959) 273.

[141] A. Roy, S. Puri, A. Acharya, Model. Simul. Mater. Sci. Eng. 15 (2007) S167–S180.

[142] S. Limkumnerd, J.P. Sethna, Phys. Rev. Lett. 96 (2006) 095503.

[143] Y.S. Chen, W. Choi, S. Papanikolaou, M. Bierbaum, J.P. Sethna, Int. J. Plast. 46 (2013) 94–129.

[144] D. Walgraef, E.C. Aifantis, Int. J. Eng. Sci. 23 (1985) 1359–1364.

[145] D. Walgraef, E.C. Aifantis, Int. J. Eng. Sci. 23 (1985) 1365–1372.

[146] D. Walgraef, E.C. Aifantis, J. Appl. Phys. 58 (1985) 688–691.

[147] J. Pontes, D. Walgraef, E.C. Aifantis, Int. J. Plast. 22 (2006) 1486–1505.

[148] I. Groma, Phys. Rev. B 56 (1997) 5807–5813.

[149] I. Groma, P. Balogh, Acta Mater. 47 (1999) 3647–3654.

[150] M. Zaiser, M.C. Miguel, I. Groma, Phys. Rev. B 64 (2001) 224102.

[151] I. Groma, F.F. Csikor, M. Zaiser, Acta Mater. 51 (2003) 1271–1281.

[152] S. Yefimov, I. Groma, E. van der Giessen, J. Mech. Phys. Solids 52 (2004) 279–300.

[153] A. El-Azab, Scr. Mater. 54 (2006) 723–727.

[154] J. Deng, A. El-Azab, J. Comput. Mater. Des. 14 (2007) 295–307.

[155] J. Deng, A. El-Azab, Philos. Mag. 90 (2010) 3651–3678.

[156] T. Hochrainer, J. Appl. Math. Mech. 93 (2013) 252–268.

[157] T. Hochrainer, M. Zaiser, P. Gumbsch, Philos. Mag. 87 (2007) 1261–1282.

[158] S. Sandfeld, T. Hochrainer, P. Gumbsch, M. Zaiser, Philos. Mag. 90 (2010) 3697–3728.

[159] T. Hochrainer, S. Sandfeld, M. Zaiser, P. Gumbsch, J. Mech. Phys. Solids 63 (2014) 167–178.

[160] S. Sandfeld, M. Zaiser, Model. Simul. Mater. Sci. Eng. 23 (2015) 065005.

[161] M. Koslowski, A.M. Cuitino, M. Ortiz, J. Mech. Phys. Solids 50 (2002) 2597–2635.

[162] M. Koslowski, Philos. Mag. 87 (2007) 1175–1184.

[163] L. Lei, M. Koslowski, Philos. Mag. 91 (2011) 865–878.

[164] N.A. Stelmashenko, M.G. Walls, L.M. Brown, Y.V. Milman, Acta Metall. Mater. 41 (1993) 2855–2865.

[165] N.A. Fleck, G.M. Muller, M.F. Ashby, J.W. Hutchinson, Acta Metall. Mater. 42 (1994) 475–487.

[166] Q. Ma, D.R. Clarke, J. Mater. Res. 10 (1995) 853–863.

[167] J.S. Stölken, A.G. Evans, Acta Mater. 46 (1998) 5109–5115.

[168] W.D. Nix, H.J. Gao, J. Mech. Phys. Solids 46 (1998) 411–425.

[169] N. Yamaki, Y. Aoyagi, K. Shizawa, Mater. Sci. Forum 503-504 (2006) 989–994.

[170] B. Devincre, V. Pontikis, in:, MRS Proc., 1993, pp. 555–560.

[171] R. Fournet, J. Salazar, Phys. Rev. B. Condens. Matter 53 (1996) 6283–6290.

[172] R. Madec, B. Devincre, L.P. Kubin, Scr. Mater. 47 (2002) 689–695.

[173] H. Yasin, H.M. Zbib, M.A. Khaleel, Mater. Sci. Eng. A 309-310 (2001) 294–299.

[174] H.M. Zbib, T. Diaz de la Rubia, V. Bulatov, J. Eng. Mater. Technol. 124 (2002) 78.

[175] H.M. Zbib, T. Rubia, Int. J. Plast. 18 (2002) 1133–1163.

[176] T. Mura, Micromechanics of Defects in Solids, 2nd ed., Springer, Tokyo, 1987.

[177] S. Xia, A. El-Azab, Model. Simul. Mater. Sci. Eng. 23 (2015) 055009.

[178] G.A. Malygin, Physics-Uspekhi 887 (1999).

[179] R. Sedláček, C. Schwarz, J. Kratochvíl, E. Werner, Philos. Mag. 87 (2007) 1225–1260.

[180] V. V Bulatov, M. Rhee, W. Cai, Mat. Res. Soc. Symp. 653 (2001).

[181] J.D. Hoffman, S. Frankel, Numerical Methods for Engineers and Scientists, CRC Press, New York, 2001.

[182] X. Han, N.M. Ghoniem, Z. Wang, Philos. Mag. 83 (2003) 3705–3721.

[183] Z.Q. Wang, I.J. Beyerlein, R. LeSar, Model. Simul. Mater. Sci. Eng. 15 (2007) 675–690.

[184] W.E. Fitzgibbon, Computational Methods in Geosciences, 1st ed., Society for Industrial and Applied Mathematic, 1992.

[185] P.B. Bochev, M.D. Gunzburger, Least-Squares Finite Element Methods, Springer, New York, 2009.

[186] B. Jiang, The Least-Squares Finite Element Method, Springer, 1998.

[187] S.. N. Varadhan, A.J. Beaudoin, A. Acharya, C. Fressengeas, Model. Simul. Mater. Sci. Eng. 14 (2006) 1245–1270.

[188] U. Essmann, H. Mughrabi, Philos. Mag. A 40 (1979) 731–756.

[189] J. Bonneville, B. Escaig, Acta Metall. 27 (1979) 1477–1486.

[190] J. Bonneville, B. Escaig, J.L. Martin, Acta Met. 36 (1988) 1989–2002.

[191] M. Verdier, M. Fivel, I. Groma, Model. Simul. Mater. Sci. Eng. 6 (1998) 755.

[192] P. Kratochv í l, Phys. Stat. Sol. 40 (1977) K165–K167.

[193] C. Chatfield, The Analysis of Time Series: An Introduction, Chapman and Hall, New York, 1989.

[194] P.J. Brockwell, R.A. Davis, Introduction to Time Series and Forecasting, 2nd ed., Springer US, 2010.

[195] H. Azami, H. Hassanpour, J. Escudero, S. Sanei, J. Adv. Res. 6 (2015) 687–698.

[196] A. V. Brandt, ICASSP '83. IEEE Int. Conf. Acoust. Speech, Signal Process. 8 (1983) 1017–1020.

[197] W.S. Cleveland, J. Am. Stat. Assoc. 74 (1979) 829–836.

[198] W.S. Cleveland, S.J. Devlin, J. Am. Stat. Assoc. 83 (1988) 596–610.

[199] S. Xia, A. El-Azab, IOP Conf. Ser. Mater. Sci. Eng. 89 (2015) 012053.

[200] H. Mughrabi, T. Ungár, W. Kienle, M. Wilkens, Philos. Mag. A 53 (1986) 793–813.

[201] B. Jakobsen, H.F. Poulsen, U. Lienert, J. Almer, S.D. Shastri, H.O. Sørensen, C. Gundlach, W. Pantleon, Science (80-.). 312 (2006) 889–92.

[202] M. Sauzay, L.P. Kubin, Prog. Mater. Sci. 56 (2011) 725–784.

[203] M. Zaiser, S. Sandfeld, Model. Simul. Mater. Sci. Eng. 22 (2014) 065012.

[204] J. Roerdink, A. Meijster, Fundam. Informaticae 41 (2001) 187–228.

[205] X. Zhang, L. Chen, L. Pan, L. Xiong, 2012 Fifth Int. Conf. Intell. Comput. Technol. Autom. (2012) 505–508.

[206] J.W. Steeds, Proc. R. Soc. London A292 (1966) 343.

[207] F.J. Humphreys, J.W. Martin, Philos. Mag. 16 (1967) 927–957.

[208] E. Göttler, Philos. Mag. 28 (1973) 1057–1076.

[209] Y. Kawasaki, Jpn. J. Appl. Phys. 18 (1979) 1429–1438.

[210] R.P. Heilbronner, Tectonophysics 212 (1992) 351–370.

[211] B. Jakobsen, U. Lienert, J. Almer, W. Pantleon, H.F. Poulsen, Mater. Sci. Forum 550 (2007) 613–618.

[212] D.A. Hughes, Q. Liu, D.C. Chrzan, N. Hansen, Acta Mater. 45 (1997) 105–112.

[213] D. Hughes, D. Chrzan, Q. Liu, N. Hansen, Phys. Rev. Lett. 81 (1998) 4664–4667.

[214] N.P. Gurao, S. Suwas, Sci. Rep. 4 (2014) 5641.

[215] M.S. Mohamed, B.C. Larson, J.Z. Tischler, A. El-Azab, J. Mech. Phys. Solids 82 (2015) 32–47.

[216] D. Kuhlmann-Wilsdorf, C. Laird, Mater. Sci. Eng. 27 (1977) 137–156.

[217] P.J. Woods, Philos. Mag. 28 (1973) 155–191.

[218] N.Y. Jin, A.T. Winter, Acta Metall. 32 (1984) 989–995.

[219] X. Li, in:, J.Q. Wang, Y.-W. Chung (Eds.), Encycl. Tribol., Springer, 2013, pp. 2313–2323.

[220] C. Déprés, M. Fivel, L. Tabourot, Scr. Mater. 58 (2008) 1086–1089.

[221] O.B. Pedersen, L.M. Brown, W.M. Stobbs, Acta Metall. 29 (1981) 1843–1850.

[222] J.M. Finney, C. Laird, Philos. Mag. 31 (1975) 339–366.

[223] R. Wang, H. Mughrabi, M. McGovern, S.Rapp, Mater. Sci. Eng. 65 (1984) 219–233.

[224] P. Li, Z.F. Zhang, S.X. Li, Z.G. Wang, Scr. Mater. 59 (2008) 730–733.

[225] X.W. Li, Z.G. Wang, S.X. Li, Philos. Mag. Lett. 79 (1999) 715–719.

[226] C. Robertson, M.C. Fivel, A. Fissolo, Mater. Sci. Eng. A 315 (2001) 47–57.

[227] L. Kubin, M. Sauzay, Acta Mater. 104 (2016) 295–302.

[228] G. Saada, P. Veyssière, in:, Dislocations in Solids, 2002, pp. 413–458.

[229] M.F. Ashby, Acta Metall. 20 (1972) 887–897.

[230] T.J.R. Hughes, The Finite Element Method: Linear Static and Dynamic Finite Element Analysis, Dover Publications, New York, 2000.

[231] X. Xiao, D. Song, J. Xue, H. Chu, H. Duan, Int. J. Plast. 65 (2015) 152–167.

VITA

VITA

Purdue University, West Lafayette, IN, United States

Doctorate in Materials Engineering, 2016

Dissertation: *Continuum Dislocation Dynamics Modeling of the Deformation of FCC Single Crystals*

Florida State University, Tallahassee, FL, United States

Master of Science in Computational Science, 2011

Thesis: *Numerical Implementation of Continuum Dislocation Theory*.

Hohai University, Nanjing, Jiangsu Province, P.R. China

Master of Science in Engineering Mechanics, 2009

Thesis: *The Application of Discrete Element Method to the Simulation of Structure Destruction*.

Hohai University, Nanjing, Jiangsu Province, P. R. China

Bachelor in Engineering Mechanics, 2007

PUBLICATIONS

PUBLICATIONS

Shengxu Xia, James Belak, Anter El-Azab, The discrete-continuum connection in dislocation dynamics. Part I: Time coarse graining of cross slip, *Modelling and Simulation in Materials Science and Engineering, submitted, May 2016*

Shengxu Xia, Anter El-Azab, Computational modelling of mesoscale dislocation patterning and plastic deformation of single crystals, *Modelling and Simultion in Materials Science and Engineering* 23, 55009 (2015)

Shengxu Xia, Anter El-Azab, A preliminary investigation of dislocation cell structure formation in metals using continuum dislocation dynamics, *IOP Conference Series: Materials Science and Engineering* 89, 012053 (2015)

Anter El-Azab, Shengxu Xia and Grethe Winther, Continuum dislocation dynamics modeling of the orientation dependence of FCC single crystals in tensile experiments, *under preparation for JMPS*